



**Politecnico di Torino**

---

COLLEGIO DI INGEGNERIA MECCANICA, AEROSPAZIALE, DELL'AUTOVEICOLO E DELLA  
PRODUZIONE

Corso di Laurea Magistrale in Automotive Engineering

MASTER OF SCIENCE THESIS

**Mechanical Characterization and  
Post-Process Heat Treatment of  
Selectively Laser Melted AlSi10Mg**

Relatore:

**Ch.mo. Prof. Giorgio Chiandussi**

Correlatore:

**Ch.mo. Prof. Paolo Fino**

Candidato:

**Carlo Marinelli**

Matricola s242599

# Abstract

Extensive research has been carried out in the field of additive manufacturing technologies to characterize the mechanical properties of various alloys, but only a limited understanding of the effects of different process parameters and of ex-situ post processes has been gained so far, limiting the robustness of the designs, as the process can be characterized by a significant variability of the results. Data in the literature show how the performance of additively manufactured parts can be improved by ex-situ heat treatments which reduce defects and residual stresses in the part, yielding properties comparable with those of cast or wrought materials. The present study is aimed at providing the characterization of the mechanical properties of the AlSi10Mg alloy manufactured with *Selective Laser Melting* (SLM), comparing the effects of different process parameters and of a post-process stress-relieving heat treatment on the final mechanical properties of the material. The printed specimens were subject to an array of examinations including chemistry, density, hardness and tensile tests. An inspection of the fractured surfaces with a *Scanning Electron Microscope* (SEM) was also carried out to better understand the test results. The experiments showed that SLM-manufactured parts can achieve mechanical properties comparable with those of traditional cast parts, however the parts present a marked anisotropy depending on the build direction, with elongation being up to 43.2% lower in specimens grown along the Z-axis compared to those grown on the XY-plane. A reduction in anisotropy, together with a minimum increase of 80% in elongation was achieved after stress-relieving. Fractographic analysis showed a ductile intergranular fracture surface, but it also highlighted how tensile results are highly influenced by internal defects.

*Keywords:* Additive Manufacturing; AM; Automotive; Metal; AlSi10Mg; SLM; Stress Relieving.

# Sommario

Molti ricercatori hanno portato avanti studi nel campo dell'additive manufacturing con l'obbiettivo di ottenere una caratterizzazione meccanica di varie leghe. Si è tuttavia potuto ottenere solo una limitata comprensione degli effetti dei parametri di processo e di differenti trattamenti post-fabbricazione, con il risultato di limitare il livello di fiducia nei progetti, in quanto il processo può essere caratterizzato da una significativa variabilità dei risultati. I dati ottenuti dalla comunità scientifica evidenziano come le prestazioni meccaniche di componenti prodotte tramite additive manufacturing possano essere migliorate tramite trattamenti termici ex-situ, i quali possono ridurre difetti e stress residui nel pezzo finito, restituendo proprietà comparabili con quelle di parti fuse o lavorate. Il presente lavoro di tesi si pone l'obbiettivo di ottenere una caratterizzazione meccanica della lega d'alluminio AlSi10Mg prodotta con *Selective Laser Melting* (SLM), confrontando gli effetti sulle proprietà meccaniche del materiale di diversi parametri di processo e di un trattamento termico di riduzione degli stress residui. Le parti stampate sono state soggette a una serie di esami, tra cui analisi chimiche, di densità, durezza e prove di trazione. Le superfici di frattura sono anche state oggetto di analisi con il microscopio elettronico a scansione (SEM). I risultati sperimentali hanno evidenziato come i componenti prodotti tramite SLM possono arrivare ad ottenere proprietà meccaniche comparabili con quelle di parti tradizionali prodotte tramite fusione. Tuttavia, le parti stampate presentano una forte anisotropia, dipendente dalla direzione di crescita del pezzo come testimoniato dall'allungamento, il quale risulta fino al 43.2% inferiore nei provini stampati lungo l'asse Z rispetto a quelli stampati nel piano XY. Dopo il trattamento di riduzione degli stress residui è stato possibile ridurre l'anisotropia del materiale ed incrementare l'allungamento di almeno 80 punti percentuali. L'analisi frattografica ha mostrato una frattura duttile ed intergranulare, ma ha anche evidenziato come i risultati dei test a trazione siano altamente influenzati dai difetti interni.

*Parole chiave:* Additive Manufacturing; AM; Automotive; Metalli; AlSi10Mg; SLM.

# Contents

<b>Abstract</b>	<b>iii</b>
<b>Sommario</b>	<b>iv</b>
<b>List of Figures</b>	<b>viii</b>
<b>List of Tables</b>	<b>xi</b>
<b>List of Acronyms</b>	<b>xii</b>
<b>1 Introduction</b>	<b>1</b>
1.1 Historical Background . . . . .	1
1.2 Process Outline . . . . .	2
1.3 Available Technologies . . . . .	4
1.3.1 Powder Bed Fusion . . . . .	5
1.3.2 Direct Energy Deposition . . . . .	11
1.3.3 Ultrasonic Additive Manufacturing . . . . .	13
1.4 Materials . . . . .	13
1.4.1 Titanium Alloys . . . . .	15
1.4.2 Nickel Alloys . . . . .	15
1.4.3 Fe- Alloys . . . . .	17
1.4.4 Aluminum Alloys . . . . .	17
1.5 Part Properties . . . . .	18
1.5.1 Porosity . . . . .	19
1.5.2 Scanning Strategy . . . . .	20
1.5.3 Residual Stresses . . . . .	21
1.5.4 Anisotropy . . . . .	22
1.5.5 Microstructure . . . . .	23
1.5.6 Post-Process Treatments . . . . .	24
1.5.7 Economics of Additive Manufacturing . . . . .	26
<b>2 Literature Review</b>	<b>29</b>
2.1 Testing Procedure . . . . .	29
2.2 Titanium . . . . .	29
2.2.1 Microstructure . . . . .	29
2.2.2 Tensile Properties . . . . .	30

2.2.3	Fatigue Properties . . . . .	30
2.2.4	Crack Growth . . . . .	30
2.3	Aluminum . . . . .	34
2.3.1	Microstructure . . . . .	34
2.3.2	Tensile Properties . . . . .	36
2.3.3	Fatigue Properties . . . . .	37
2.3.4	Crack Growth . . . . .	40
2.4	Discussion . . . . .	41
2.5	Conclusions . . . . .	42
<b>3</b>	<b>Experimental Procedures</b>	<b>43</b>
3.1	Manufacturing Process . . . . .	43
3.2	Specimens . . . . .	45
3.3	Powder Particle Size Distribution . . . . .	49
3.4	Tensile Test . . . . .	50
3.5	Density Test . . . . .	51
3.6	Chemistry Test . . . . .	54
3.7	Hardness Test . . . . .	55
3.8	Optical Microscopy . . . . .	57
3.9	Scanning Electron Microscopy . . . . .	58
<b>4</b>	<b>Experimental Results</b>	<b>60</b>
4.1	Powder Characterization . . . . .	60
4.1.1	North American Experimental Results . . . . .	60
4.1.2	Italian Experimental Results . . . . .	62
4.2	Chemistry . . . . .	63
4.2.1	North American Experimental Results . . . . .	63
4.2.2	Italian Experimental Results . . . . .	64
4.3	Microstructure . . . . .	64
4.3.1	North American Experimental Results . . . . .	64
4.3.2	Italian Experimental Results . . . . .	66
4.4	Density . . . . .	68
4.4.1	North American Experimental Results . . . . .	68
4.4.2	Italian Experimental Results . . . . .	69
4.5	Hardness . . . . .	69
4.5.1	North American Experimental Results . . . . .	70
4.5.2	Italian Experimental Results . . . . .	70
4.6	Tensile Properties . . . . .	71
4.6.1	North American Experimental Results . . . . .	72
4.6.2	Italian Experimental Results . . . . .	76
4.7	Fracture Surface Characterization . . . . .	79
4.7.1	North American Experimental Results . . . . .	80
4.7.2	Italian Experimental Results . . . . .	88

<b>5 Discussion of Results</b>	<b>91</b>
<b>6 Conclusions</b>	<b>96</b>
<b>Bibliography</b>	<b>99</b>
<b>Vita Auctoris</b>	<b>105</b>

# List of Figures

1.1	Generic AM process steps ([15]) . . . . .	3
1.2	STL triangle, defined by three vertices and a normal vector $n$ , and effect of mesh size ([16]) . . . . .	3
1.3	Schematic of a <i>Selective Laser Melting</i> machine ([18]) . . . . .	6
1.4	SLM thermal profile . . . . .	7
1.5	Typical scan strategies . . . . .	8
1.6	Schematic of an <i>Electron Beam Melting</i> machine ([27]) . . . . .	9
1.7	Schematic of a <i>Binder Jetting</i> machine (courtesy of Additively) . . . . .	10
1.8	Schematic of a LENS machine ([31]) . . . . .	11
1.9	Schematic of a wire-fed DED machine ([21]) . . . . .	12
1.10	Illustration of a UAM machine (courtesy of Fabrisonic) . . . . .	13
1.11	Schematic of <i>Water Atomization</i> process (courtesy of FCA) . . . . .	15
1.12	Schematic of <i>Gas Atomization</i> process (courtesy of FCA) . . . . .	16
1.13	Schematic of PA and PREP processes (courtesy of FCA) . . . . .	16
1.14	SEM images of GA/RA/PREP powders . . . . .	17
1.15	Al-Si phase diagram ([39]) . . . . .	18
1.16	AM parameters interaction . . . . .	19
1.17	Typical relation between Laser Scanning Power and Velocity (courtesy of Renishaw) . . . . .	20
1.18	Comparison between process and powder-induced porosity ([35]) . . . . .	20
1.19	Proposed contour remelting ([10]) . . . . .	21
1.20	Example of severe part cracking after SLM processing (courtesy of Renishaw) . . . . .	21
1.21	SLM AlSi10Mg microstructure . . . . .	23
1.22	SLM AlSi10Mg porosity . . . . .	24
1.23	SLM AlSi12 columnar microstructure . . . . .	25
1.24	Ti6Al4V microstructure after heat treatment . . . . .	25
1.25	AM market growth . . . . .	27
1.26	AM part complexity vs. part manufacturing cost ([31]) . . . . .	27
1.27	AM break-even point compared to conventional manufacturing on the base of manufacturing volume ([59]) . . . . .	28
2.1	SLM Ti6Al4V columnar microstructure . . . . .	31
2.2	SLM Ti6Al4V CT scan before/after HIP . . . . .	31
2.3	HCFpProperties of Ti6Al4V specimens . . . . .	32

2.4	SLM Ti6Al4V fractography . . . . .	32
2.5	Ti6Al4V crack growth . . . . .	33
2.6	SLM Ti6Al4V Kitigawa . . . . .	33
2.7	SLM AlSi12 microstructure . . . . .	34
2.8	SLM AlSi12 CT scan without/with base plate heating . . . . .	35
2.9	SLM AlSi12 CT scan before/after HIP . . . . .	35
2.10	SLM AlSi12 microstructure with precipitates after HIP . . . . .	35
2.11	SLM AlSi12 stress-strain curve . . . . .	36
2.12	SLM AlSi10Mg stress-strain curve . . . . .	37
2.13	SLM AlSi10Mg brittle fracture surface . . . . .	37
2.14	SLM AlSi12 VHCF Wohler diagram . . . . .	38
2.15	SLM AlSi12 fatigue life . . . . .	38
2.16	SLM AlSi10Mg Wohler diagram . . . . .	39
2.17	SLM AlSi10Mg fractography . . . . .	39
2.18	SLM AlSi12 crack growth curves . . . . .	40
3.1	EOS M 290 machine (Courtesy of EOS) . . . . .	44
3.2	North American specimen arrangement in the build chamber . . . . .	45
3.3	ASTM specimens dimensions ([64]) . . . . .	46
3.4	North American as-built rods showing build support marks . . . . .	47
3.5	ISO specimens dimensions ([65]) . . . . .	48
3.6	Italian cubic and cylindrical specimens (before and after machining) . . . . .	49
3.7	Example of powder size distribution chart (courtesy of TLS Technik) . . . . .	50
3.8	Fritsch ANALYSETTE 22 NanoTec laser particle sizer (courtesy of Fritsch) . . . . .	50
3.9	Tinius Olsen universal testing machine . . . . .	51
3.10	MTS Criterion Model 43 tensile testing machine (courtesy of MTS) . . . . .	52
3.11	X-Ray CT general setup ([10]) . . . . .	53
3.12	Example of gravimetric density scale based on Archimedes' Principle (courtesy of Mettler Toledo) . . . . .	53
3.13	Baird Spectrovac DV-3 setup . . . . .	54
3.14	Rockwell hardness test method (schematic diagram)([68]) . . . . .	55
3.15	Hardness testing machines at the North American supplier (a) and in Italy (b) . . . . .	56
3.16	Brinell hardness test measurement principle ([69]) . . . . .	57
3.17	Schematics of a SEM (courtesy of [71]) . . . . .	58
3.18	Setup of the SEM used at the University of Windsor . . . . .	59
4.1	Particle size distribution for TLS AlSi10Mg powder . . . . .	61
4.2	EOS-supplied powder morphology at 1000x magnification . . . . .	62
4.3	Particle size distribution for EOS AlSi10Mg powder . . . . .	63
4.4	Microstructure of as-built specimens from Batch 2 at 100x magnification . . . . .	65
4.5	Microstructure of stress-relieved specimens from Batch 1 at 100x magnification . . . . .	66

4.6	Microstructure of specimens from Batch A at 50x magnification . . . . .	67
4.7	Microstructure of specimens from Batch A at 100x magnification . . . . .	68
4.8	Microstructure of a specimen from Batch A at 500x magnification, parallel section . . . . .	68
4.9	North American Batch 1 Z-Axis tensile curves . . . . .	73
4.10	Box-plot analysis of mechanical properties variance for North American batches (1 and 2) . . . . .	75
4.11	Engineering stress-strain curves for specimens tested in Italy . . . . .	77
4.12	Schematics of the interaction between build and stress orientation for (a) XY-plane and (b) Z-axis built specimens . . . . .	80
4.13	SEM image of the fracture surface of XY-plane as-built specimens . . . . .	81
4.14	SEM image of the fracture surface of Z-axis as-built specimens . . . . .	82
4.15	SEM image of the fracture surface of 45°-axis as-built specimens . . . . .	83
4.16	SEM image of the fracture surface of XY-plane stress-relieved specimens . . . . .	84
4.17	Comparison of as-built and heat treated grain structures for XY specimens . . . . .	85
4.18	SEM images of the fracture surface of Z-axis stress-relieved specimens . . . . .	86
4.19	SEM images of the fracture surface of 45°-axis stress-relieved specimens . . . . .	87
4.20	Low-magnification image of the fracture surface of as-built specimens . . . . .	89
4.21	100x image of the fracture surface of as-built specimens . . . . .	89
4.22	1500x image of the fracture surface of as-built specimens . . . . .	89
4.23	Image of the fracture surface of stress-relieved specimens . . . . .	90
4.24	1000x image of the fracture surface of stress-relieved specimens . . . . .	90
4.25	2000x image - Comparison of the fracture surface of as-built and stress-relieved Z-axis specimens . . . . .	90

# List of Tables

1.1	SLM typical process parameter . . . . .	8
1.2	EBM typical process parameter . . . . .	10
1.3	BJ typical process parameters . . . . .	11
1.4	LENS typical process parameters . . . . .	12
1.5	Typical heat treatment parameters . . . . .	26
3.1	Nominal AlSi10Mg powder chemical composition in weight % . . . . .	43
3.2	Technical data EOS M 290 . . . . .	44
3.3	Printing parameters EOS M 290 . . . . .	45
3.4	ASTM specimens specifications . . . . .	46
3.5	ISO specimens regulated dimensions . . . . .	48
4.1	Nominal vs. actual TLS-supplied AlSi10Mg powder chemical composition in weight % . . . . .	60
4.2	TLS powder particle cumulative size distribution percentiles . . . . .	61
4.3	EOS powder particle cumulative size distribution percentiles . . . . .	62
4.4	Average weight % chemical composition of Batch 1 (stress-relieved spec- imens) . . . . .	63
4.5	Average weight % chemical composition of Batch 2 (as-built specimens)	64
4.6	Nominal AlSi10Mg EOS powder chemical composition in weight % . . . .	64
4.7	Bulk density and porosity measurements of parallelepiped specimens . .	69
4.8	Rockwell and Brinell hardness results for Batch 1 & 2 . . . . .	70
4.9	Brinell hardness results for batches A, B & C . . . . .	71
4.10	Tensile test results for Batch 1 (stress-relieved) . . . . .	72
4.11	Tensile test results for Batch 2 (as-built) . . . . .	72
4.12	Percent variation in mechanical properties between as-built and stress- relieved AlSi10Mg specimens . . . . .	74
4.13	Common mechanical properties for sand-cast and permanent mold-cast AlSi10Mg ([75][76]) . . . . .	74
4.14	Average tensile test results for specimens tested in Italy . . . . .	78
5.1	Comparison of chemical composition between as-built and stress-relieved specimens . . . . .	91

# List of Acronyms

- AM** *Additive Manufacturing*. ix, 1, 2, 4, 5, 14, 15, 18, 19, 46
- ASTM** *American Society of Testing and Materials*. 2, 4, 31
- BJ** *Binder Jetting*. ix, xii, 1, 4, 5, 10, 11, 13
- CAGR** *Compound Annual Growth Rate*. 28
- CNC** *Computer Numerical Control*. 14
- CRF** *Centro Ricerche Fiat*. 47
- CT** *Computed Tomography*. x, 31, 55, 56
- DED** *Direct Energy Deposition*. ix, 1, 4, 5, 11–14
- DMLS** *Direct Metal Laser Sintering*. 4, 6, 7, 46, 47
- EBM** *Electron Beam Melting*. ix, xii, 1, 4, 6, 9–11, 18
- EMEA** *Europe Middle East and Asia*. 46
- FCA** *Fiat Chrysler Automobiles*. 46
- GA** *Gas Atomization*. ix, 16, 18
- HCF** *High Cycle Fatigue*. x, 31
- HIP** *Hot Isostatic Pressing*. 25, 28, 32, 33
- HPDC** *High Pressure Die Casting*. 37
- LCF** *Low Cycle Fatigue*. 31
- LEFM** *Linear Elastic Fracture Mechanics*. 36
- LENS** *Laser Engineered Net Shaping*. ix, xii, 1, 5, 12, 13
- LOM** *Light Optical Microscopy*. 17
- NAFTA** *North American Free Trade Agreement*. 46

**PA** *Plasma Atomization.* ix, 16, 18

**PBF** *Powder Bed Fusion.* 4–6, 10, 13

**PM** *Powder Metallurgy.* 10

**PREP** *Plasma Rotating Electrode Process.* ix, 16, 18

**RA** *Rotary Atomization.* 18

**SEM** *Scanning Electron Microscope.* ix, 9, 17, 61, 62

**SLM** *Selective Laser Melting.* ix, x, xii, 1, 4, 6–9, 11, 18–20, 25–27, 33, 36, 38–41, 96, 101

**SLS** *Selective Laser Sintering.* 1, 5

**Spark-AES** *Spark Atomic Emission Spectrometry.* 57, 67

**STL** *STereoLitography.* 2, 3

**UAM** *Ultrasonic Additive Manufacturing.* ix, 5, 13, 14

**USW** *Ultrasonic Metal Welding.* 13, 14

**UTS** *Ultimate Tensile Strength.* 32, 37

**WA** *Water Atomization.* ix, 15

# Chapter 1

## Introduction

### 1.1 Historical Background

The development of *Additive Manufacturing* (AM) technologies started in the 1980s, when the first examples of polymer 3D-Printed parts were showcased [1]. The first trials on additively manufactured metal parts were performed only towards the end of the same decade with powder bed-based systems, which still used polymer-based techniques, referred to as *Selective Laser Sintering* (SLS), and produced parts with poor mechanical properties due to the incomplete melting and adhesion of the powder [2].

This technology later evolved into *Selective Laser Melting* (SLM), which features fully melting of the powder and yields greatly superior mechanical properties.

In the same period, research at the MIT studied a technology named *three-dimensional printing* which used inkjet printing to deposit binder. The process received the name of *Binder Jetting* (BJ) and is characterized by the fact that the application of heat is separated from the build process, thus preventing residual stresses to form in the part.

A completely different class of 3D printers, referred to as *Direct Energy Deposition* (DED), relies on the direct deposition of metal feedstock in a continuously heated melt pool to create the part, tracing its roots directly back to welding. The use of powder was first studied in 1995 at Sandia National Labs and commercialized as *Laser Engineered Net Shaping* (LENS).

By the beginning of the century a variation of the powder bed process was patented in Sweden: it didn't use laser to melt the parts, but instead relied on a focused electron beam as heat source. It is referred to as *Electron Beam Melting* (EBM) and is very similar to SLM, albeit it presents much lower residual stresses.

To date, powder bed technologies such as SLM and EBM are the most widespread in the market, and the ones which have been subject to the most extensive amount of research.

The main focus of research to date has been the static characterization of various alloy-process combinations, to understand the relations between process parameters and static mechanical properties. A more limited number of studies were carried out in the field of fatigue and on the effects of post-process treatments [3].

It is accepted that additive manufactured components show comparable, and in some

cases better, static characteristics compared to conventional parts [4] [5]. However, fatigue properties might be impaired by a number of different factors: high thermal gradients during manufacturing, which cause important residual stresses and very fine microstructure; residual porosity of the material, resulting from incomplete bonding of the layers and/or evaporation of alloying materials, and significant surface roughness in the as-built condition [4] [5] [6] [7] [8] [9] [10] [11] .

Such limitations have been shown to be highly dependent on the selected post-process treatments: various heat-treatment techniques have been proposed, aiming at reducing internal defects, reducing the residual stresses or modifying the grain structure to obtain the desirable mechanical characteristics [12].

## 1.2 Process Outline

Additive Manufacturing, also referred to as 3D Printing, has undergone substantial changes since the days of its inception. It is defined by the *American Society of Testing and Materials* (ASTM) as "The process of joining materials to make objects from 3D model data, usually layer upon layer, as opposed to subtractive manufacturing methodologies. Synonyms: additive fabrication, additive processes, additive techniques, additive layer manufacturing, layer manufacturing, and freeform fabrication" [13].

All AM processes share the same layer-by-layer manufacturing method: a 3D CAD model is sliced into micrometric layers, which are then manufactured sequentially by depositing new material on top of the previous layer.

The main advantages of such an approach are a complete design freedom, which allows production of complex features otherwise impossible to obtain with conventional manufacturing processes, and significant raw material savings, as only the needed material will have to be used, given the additive and not subtractive nature of the process [14].

The process steps from the preparation of the CAD model to the finished 3D printed object can be detailed as follows [15]:

1. **CAD Model Preparation** Every part to be manufactured by AM has to be described by a virtual model that fully represents its geometry. The part might either be designed in a CAD environment or it can be the result of a reverse engineering by 3D scanning.
2. **Conversion to STL** AM machines accept as input the STereoLitography (STL) format. This file format, initially released in 1987 by 3D Systems and today's de-facto standard, approximates by means of triangles the outer and the inner surfaces of the part (a process referred to as *triangulation* or *tessellation*). This operation inherently introduces errors in the model, as a triangle would always be an approximation of a curved surface. The higher the mesh density during this step, the lower the introduced error (as shown in Fig. 1.2).
3. **STL File Manipulation** The STL file retrieved from the CAD software may

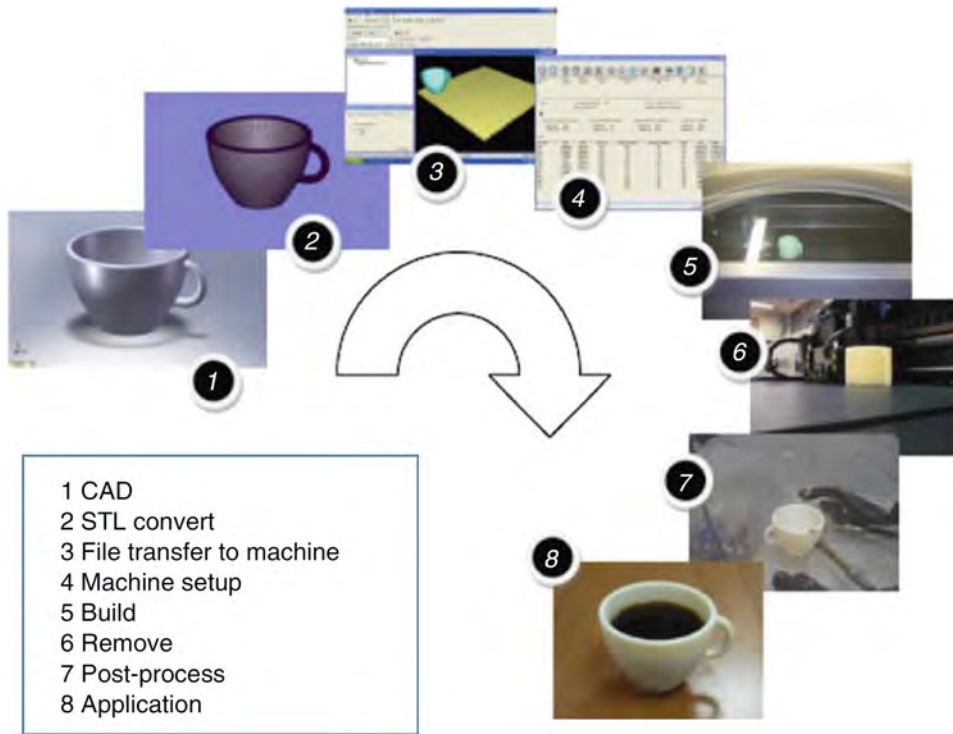


Figure 1.1: Generic AM process steps ([15])

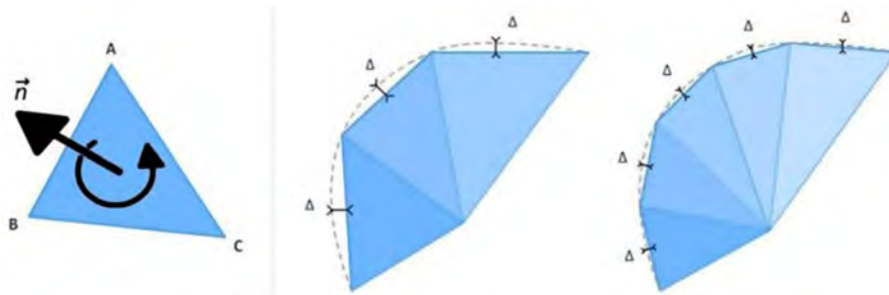


Figure 1.2: STL triangle, defined by three vertices and a normal vector  $n$ , and effect of mesh size ([16])

present meshing errors, such as triangle intersections, unwanted holes, surface mismatching or erroneous wall thickness. Specific software packages, either manual or automatic, dedicated to the repair of the meshing are commonly used to repair these flaws [16]. Once the STL is ready, it must be transferred to the machine, where it can be manipulated by the integrated machine software in order to optimize part position and orientation for building, as well as in order to create the required supporting structures for overhanging features of the part.

4. **Machine Setup** Over 280 machine parameters (related to material constraints, layer thickness, energy source, build rate, etc.) have to be set up in order to obtain a reliable process. The chosen parameters are normally a compromise between process speed, cost and final part quality.
5. **AM Build** The building itself can take anywhere from a few hours to days, de-

pending on part dimensions and complexity, technology and required final quality. Once the machine has been set up by the operator, the build is a largely automated process which requires no supervision. Monitoring can nowadays be done remotely, and a single operator can take care of multiple machines running in parallel.

6. **Part Removal** As a part is completed, it must be removed from the build chamber. This step is still highly manual and it is necessary to wait for the entire build chamber to be cold enough for safe operation. The part itself must be removed from the build chamber, cleaned from any residual excess material, and moved to the post-processing station.
7. **Part Post-processing** The as-built part must at first be removed from its supporting structures, a critical and tricky operation which requires highly skilled manual labour. Depending on the manufacturing technology, and on the required final mechanical characteristics, additional mechanical and/or heat treatments might be required, adding to the process complexity.
8. **Final Application** Only at this stage the part is ready to be applied in its intended function, or to be assembled together with other parts.

### 1.3 Available Technologies

AM can be divided into various process categories, as defined by the standard process terminology issued by the ASTM F42 Technical Committee [13], of which the following apply to Metal AM:

- ***Powder Bed Fusion (PBF)***
  - *Selective Laser Melting (SLM)*
  - *Direct Metal Laser Sintering (DMLS)*
  - *Electron Beam Melting (EBM)*
  - *Binder Jetting (BJ)*
- ***Direct Energy Deposition (DED)***
  - *Laser Engineered Net Shaping (LENS)*
- **Sheet Lamination**
  - *Ultrasonic Additive Manufacturing (UAM)*

All of these processes have been commercially exploited, but most of the attention has been dedicated to PBF and DED processes [3], which can provide the best mechanical properties to date. New technologies such as BJ or UAM are now being developed aiming at faster build rates, to bring AM to the series production environment.

Metal AM presents its own challenges, especially when compared with polymer-based AM. The energy density and the temperatures required to reach full melting of a metallic material are much higher than for polymers, exceeding 1000 °C for materials such as Titanium or Inconel, thus requiring better heat shielding as well as temperature and atmospheric control to ensure safe operation of the machine. Most metal systems also require the use of a build substrate and support structures, which are to be separated from the part in the post-processing phase, as a means to avoid part warping and distortion during cooling due to the very high temperature gradients between the molten metal and the surroundings. Part warping during the build could even cause interference between the build part and moving machine parts, resulting in abortion of the build process.

Most of the available technologies share the use of metallic powders as raw material, thus requiring appropriate powder handling systems, both to ensure optimal material properties and to protect the operator especially when dealing with reactive powders. Any metal powder handling system must meet four basic requirements [17]:

1. The powder reservoir volume must be sufficient to feed the process even when using the maximum build height, without requiring stops to refill.
2. The volume of powder distributed on the build surface shall be enough to cover the previous layer, yet not excessive.
3. The powder spreading shall be a repeatable operation.
4. Powder spreading should not create excessive shear forces which could damage the previous layers.

### 1.3.1 Powder Bed Fusion

*Powder Bed Fusion* systems were the first to be developed and commercialized. They evolved from *Selective Laser Sintering* (SLS), a process first developed in the '80s at the University of Texas at Austin, USA [2], which however could not achieve full melting of the powder and therefore presented inadequate mechanical properties. The technology has been progressively modified to improve productivity, final mechanical properties, or just to avoid patent infringements, but the basic process, schematically illustrated in 1.3, always involves controlled fusion of powder particles to create the contours of each layer of the part. Depending on the energy source used to induce powder melting, the process is known under different terms: when it involves a laser beam it might be referred to as *Selective Laser Melting* (SLM) or *Direct Metal Laser Sintering* (DMLS), on the other hand when an electron beam is used as the energy source it is referred to as *Electron Beam Melting* (EBM).

In PBF, the build volume is usually a closed chamber (with dimensions up to 800 x 400 x 500 ( $mm^3$ ) [19]) operated either in vacuum or with a filling of inert gases to prevent oxidation of reactive metallic powder [20]. A leveling system feeds the powder

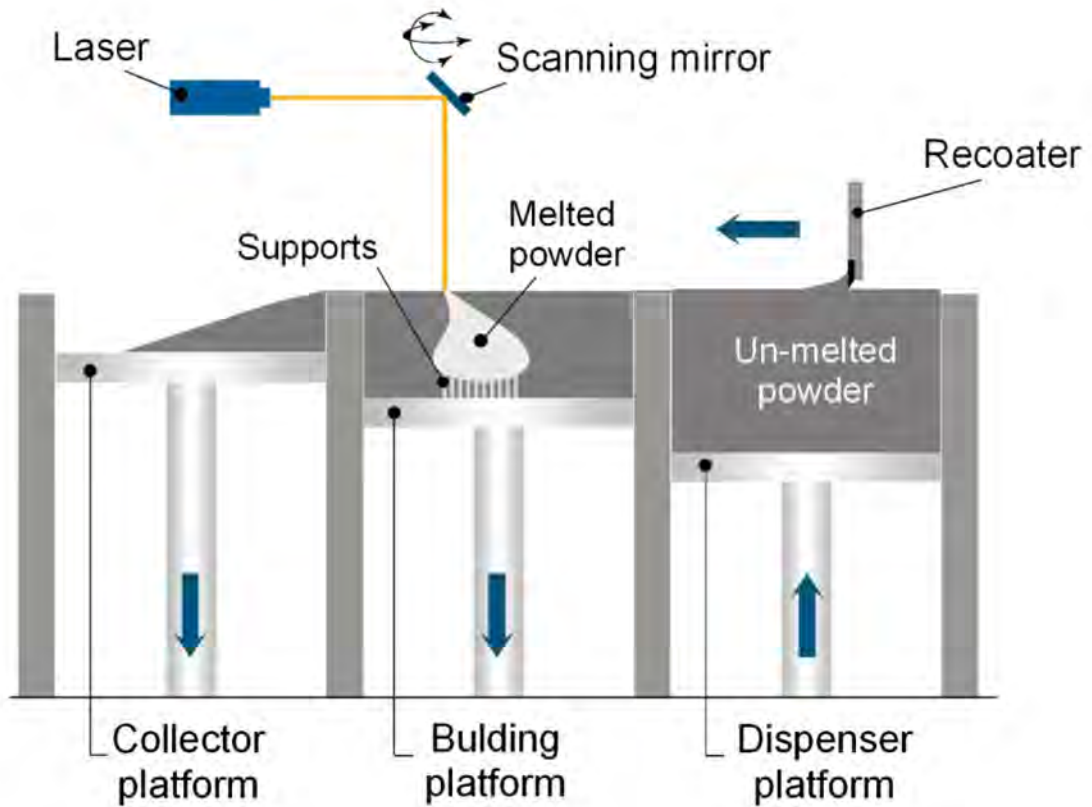


Figure 1.3: Schematic of a Selective Laser Melting machine ([18])

from a powder reservoir to the work area, on top of the build plate, which can be heated usually from 100 °C up to 500 °C [20] [3].

The pre-heating is beneficial in minimizing the laser power requirements and in preventing warping of the part due to the high thermal gradients experienced during the process, which cause non-uniform thermal expansion and contraction (curling). Once a layer has been properly formed and preheated, the energy source proceeds to selectively melt the part contours and fillings, following a pre-determined scanning strategy, to build up a layer of thickness between 20 to 200  $\mu\text{m}$  [20].

The energy provided by the laser or electron beam does not only cause the surface layer to melt, but also induces re-melting of the underlying layer, which helps to achieve complete adherence of the various layers and reduced porosity, but also leads to residual stresses due to thermal cycling [21] [3]. However the rapid melting and solidification of the metal results in unique microstructural properties, different from cast or wrought parts made of the same alloy. When a layer is completed, the build plate is lowered by a single layer thickness, a new layer of powder is fed evenly on top of the previous layer, and the process repeats itself until completion of the part. As the build is finished, a cool down period has to be observed, to ensure operator safety and to avoid uneven part cool down, which could result in warping or cracking. As the entire build chamber reaches ambient temperature, excess non-melted powder can be sifted and re-introduced in a subsequent process, and the as-fabricated part can be extracted[17].

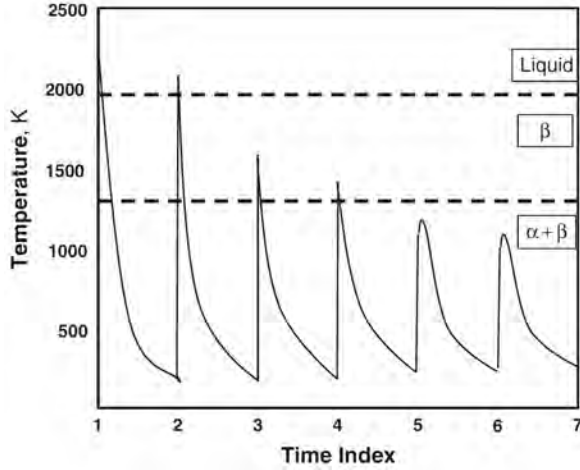


Figure 1.4: Example of thermal profile of a single layer of  $Ti6Al4V$  during SLM ([22])

### Selective Laser Melting and Direct Metal Laser Sintering

*Selective Laser Melting* (SLM) (also called *Direct Metal Laser Sintering* (DMLS)), is a powder bed fusion technology developed to produce fully dense parts, typically usable in the state in which they come out of the machine. It relies on a high-power laser beam, typically a Nd- or Yb-YAG fiber laser focused by a system of rotating mirrors, to induce local melting of the powder, which will return fully dense parts after solidification. Powder heating is due to photon absorption by the powder particles: the adoption of fiber lasers, whose wavelength is closer to the maximum absorptivity of metals has made it possible to achieve a reliable process. Laser power, scanning speed, layer thickness, hatching distance and angle are the main parameters used to optimize the process. They determine the volumetric energy density delivered to the powder, as defined by Eq. 1.1

$$E_v = \frac{P_L}{v_s \cdot h_d \cdot t_l} \quad (1.1)$$

where  $P_L$  is the laser power,  $v_s$  is the scanning velocity,  $h_d$  is the hatch distance, and  $t_l$  is the layer thickness [3]. The volumetric energy density in turn influences the mechanical properties and surface finish of the end product [18]. Modern machines can be equipped with up to four laser beams, which simultaneously scan the part contours to significantly improve process speed and productivity [23][24].

During the build process, the build chamber is flushed with inert gas (argon, nitrogen or helium) to provide the correct component cooling and to prevent oxidation of the powder. The laser beam scans the surface following a predetermined path, which influences the thermal gradients inside the part, consequently determining the end part microstructural features and residual stresses. The main scanning patterns available today are depicted in Fig.1.5. It has been proved effective for SLM to adopt island scanning as a mean to reduce residual stresses and improve final part density, performing contour passes after melting [21].

Components realized with SLM, due to the very high temperature gradients experienced through the build chamber, require the use of supporting structures, rigidly

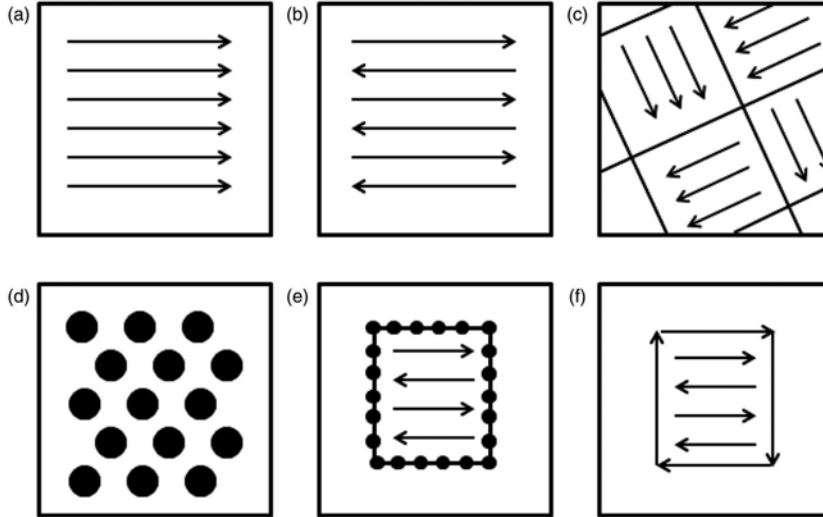


Figure 1.5: Typical scanning strategies in metal AM in the  $XY$  plane: a) unidirectional or concurrent fill, b) bi-directional, snaking or countercurrent fill, c) island scanning, d) spot melting, e) spot melting contours with snaking fill, f) line melting contours with snaking fill ([21])

Table 1.1: SLM typical process parameter

	Layer Thickness ( $\mu\text{m}$ )	Build Volume ( $\text{m}^3$ )	Build Temperature ( $^{\circ}\text{C}$ )	Laser Power (W)	Laser Speed (m/s)	Build Rate ( $\text{cm}^3/\text{h}$ )
SLM	20-200	Up to 0.8x0.4x0.5	100-500	20-1000	0.5-10	Up to 171

attached to the build plate, to avoid warping and cracking and to support overhanging features. The mechanical removal of these supports after build completion requires highly skilled operators and is both time consuming and expensive.

An excessively low energy density will result in incomplete melting, preventing optimal adherence of the various layers and causing delamination, possible melt ball formation (solidification of melted material into spheres, which prevent layer adherence) and an increase in porosity due to lack-of-fusion (characterized by a typically non-spherical shape). An excessively high energy density on the other hand leads to overheating of the material causing again melt ball formation and especially spatter ejection (the convective transport of liquid or vapor out of the melt pool), which leads to increased porosity.

## Electron Beam Melting

*Electron Beam Melting* (EBM) is a process first developed at Chalmers University of Technology in Gothenburg and brought to the market by ARCAM in 2002 [25] [26]. As in SLM a powder bed is created by a feeding system and fully dense parts can be produced. The main difference is that an electron beam, generated in an electron gun, is used as the energy source to induce local melting of the powdered metal. An EBM system could

be seen as a high powered *Scanning Electron Microscope* (SEM), as the electron beam is accelerated by a differential voltage, focused by a system of electromagnetic lenses and directed by a magnetic scan coil. The absence of moving parts allows for extremely high scan speed and increased productivity compared to single-laser SLM systems. This is also helped by the extremely high power levels achievable with electron beams, which enable the use of higher layer thicknesses compared to SLM, thus directly improving build rate (albeit at the expense of a rougher surface finish [18]).

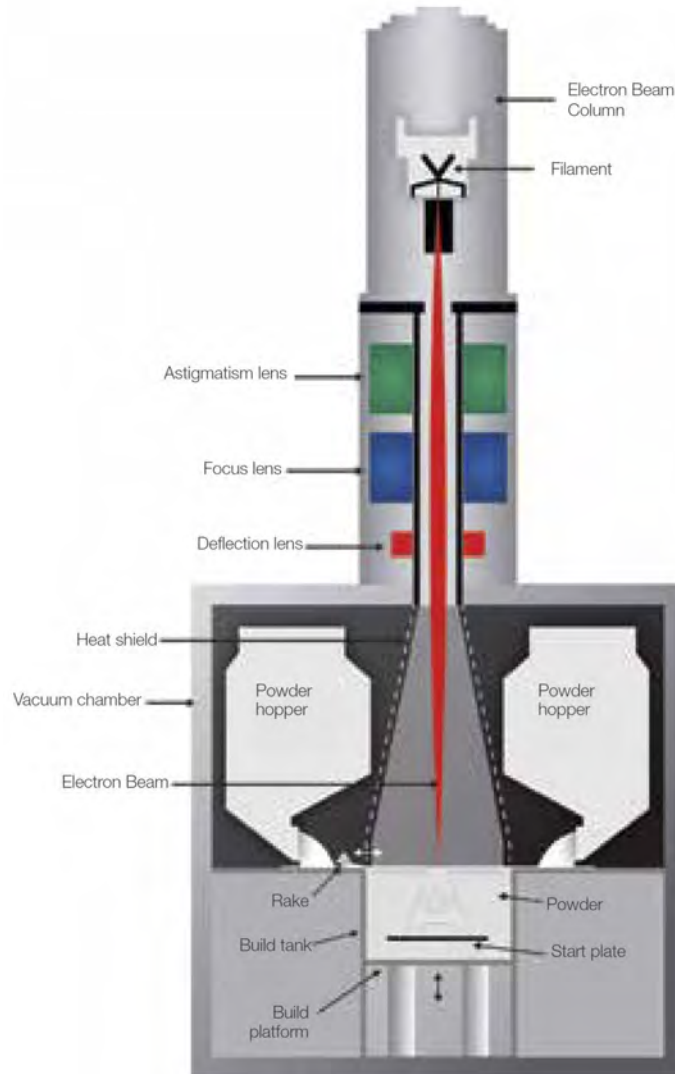


*Figure 1.6: Schematic of an Electron Beam Melting machine ([27])*

Heating of the powder is achieved by the transfer of kinetic energy from the incoming electrons to the powder particles. Therefore only conductive materials can be effectively used, otherwise local charge build-up would be detrimental to final part quality [17]. As a result of the absence of rotating mirrors used to focus the beam, EBM systems can achieve extremely high scanning speeds, thus allowing for a homogeneous pre-heating of the powder, at each layer, at much higher temperatures than SLM systems. The high process temperature is central in reducing the residual stresses in the end part, and makes it possible to use materials with extremely high melting temperatures. The lower

residual stresses also reduce the need of support structures, whose mass is an order of magnitude lower than in SLM builds [17].

A fundamental difference between SLM and EBM is that EBM systems are operated in a near-vacuum atmosphere, so as to avoid electrical charging of the powder and to reduce to a minimum the possible sources of contamination, which allows for an easier treatment of highly reactive materials such as Ti-alloys.

Table 1.2: EBM typical process parameter

	Layer Thickness ( $\mu m$ )	Build Volume (Dia x H) (m)	Build Temperature ( $^{\circ}C$ )	Beam Power (W)	Laser Speed (m/s)	Build Rate ( $cm^3/h$ )
EBM	50-200	Up to 0.35x0.38	550-1100	Up to 3000	8000	Up to 80

## Binder jetting

*Binder Jetting* (BJ) is a process which, although not involving any actual melting during the build operation, can be considered a PBF process in that it presents a powder bed, which is selectively filled with a binder that is cured immediately, layer by layer, to create a so-called "green part", a part which can sustain itself without the need for supporting structures, but will need further thermal processing in a downstream station (typically sintering in a furnace) to achieve its full mechanical properties.

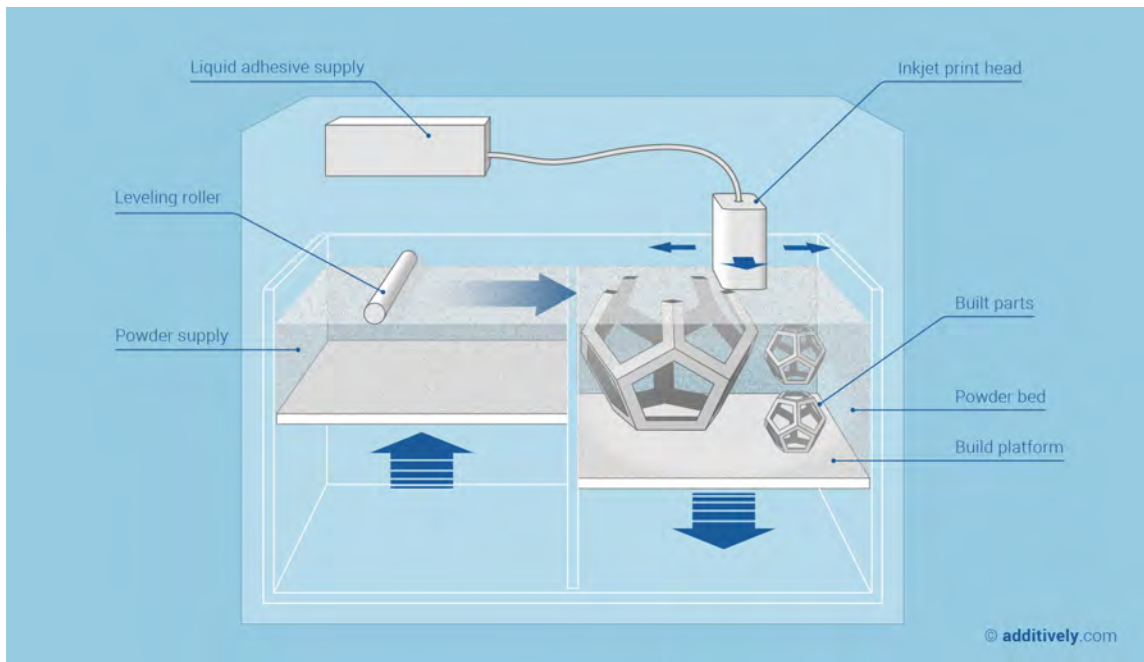


Figure 1.7: Schematic of a Binder Jetting machine (courtesy of Additively)

Binder Jetting systems are still mostly in their development phase, but are set to deliver extremely higher production rates than any other technology, together with in-

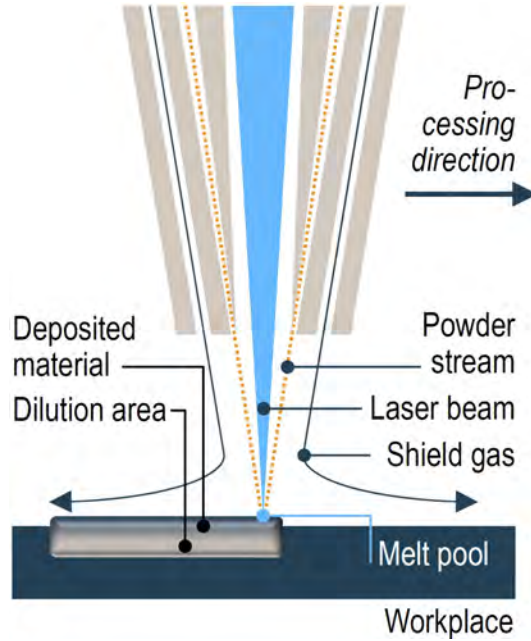


Figure 1.8: Schematic of a LENS machine ([31])

creased build volumes. However, as BJ is essentially a *Powder Metallurgy* (PM) problem it still suffers from problems typical of the PM world, namely high porosity and unpredictable sintering-induced distortion [21]. Nevertheless, recent developments from various manufacturers claim to have addressed the issues for materials ranging from steel to titanium and aluminum [17][28] and the technology is being tested for orthopedic applications [29][30].

Table 1.3: BJ typical process parameters

	Layer Thickness ( $\mu\text{m}$ )	Build Volume ( $\text{mm}^3$ )	Build Rate ( $\text{cm}^3/\text{h}$ )
BJ	15-200	Up to 800x500x400	Up to 100

An advantage of BJ systems is the possibility to work in ambient atmosphere, as powders do not present reactivity problems at low temperatures. This also allows for extremely big build chambers when compared to both SLM and EBM, enabling the manufacturing of even more complex parts.

### 1.3.2 Direct Energy Deposition

In *Direct Energy Deposition* (DED) a focused energy source, in the form of a laser, arc or electron beam melts the metallic feedstock as it is deposited onto the part. Feedstock can be either powder (Fig. 1.8) or wire (Fig. 1.9). It can be treated as an evolution of welding, and can be used to add features to an existing part or to repair damaged

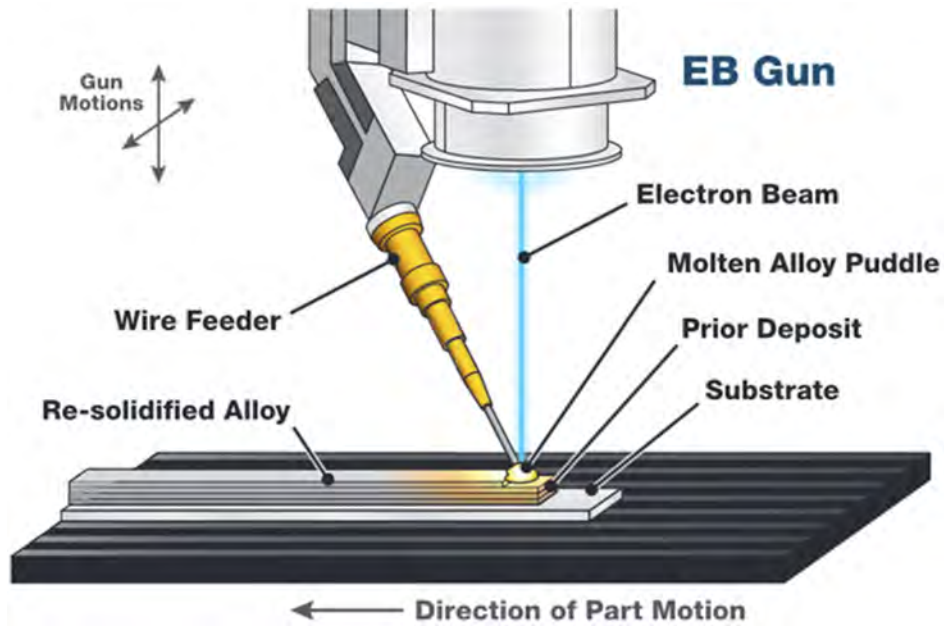


Figure 1.9: Schematic of a wire-fed DED machine ([21])

structures, especially when paired with post-process CNC machining [21]. Most systems feature a 4- or 5-axis motor system, thus overcoming the constraints of layer-by-layer production, although the absence of a surrounding powder bed performing a support action on the part itself creates the need for more complex support structures, and in the end, limiting the design freedom for such a technology [31]. The build chamber is enclosed to provide operator safety, but it is not necessarily flooded with inert gases, as the shield gas directed at the melt pool provides adequate resistance to oxidation in most cases.

As it is the case with PBF systems, the energy source causes a re-melting of the first underlying layers of material, improving part density but causing thermal cycling and residual stresses as well.

At present the use of a laser power source together with a powder feedstock is the most commonly employed DED process. It was originally developed at Sandia National Labs and patented as the *Laser Engineered Net Shaping* (LENS) process. As the only restriction to build volume is the actual motion envelope of the robot arm to which the head is attached, DED systems provide fairly large build volumes and are suited to the production of large components.

Table 1.4: LENS typical process parameters

	Layer Thickness ( $\mu\text{m}$ )	Build Volume ( $\text{mm}^3$ )	Build Temperature ( $^{\circ}\text{C}$ )	Beam Power (W)	Laser Speed (m/s)	Build Rate ( $\text{cm}^3/\text{h}$ )
LENS	40-1000	900x1500x900	Ambient	1000-2000	2.5 - 25	Up to 300

### 1.3.3 Ultrasonic Additive Manufacturing

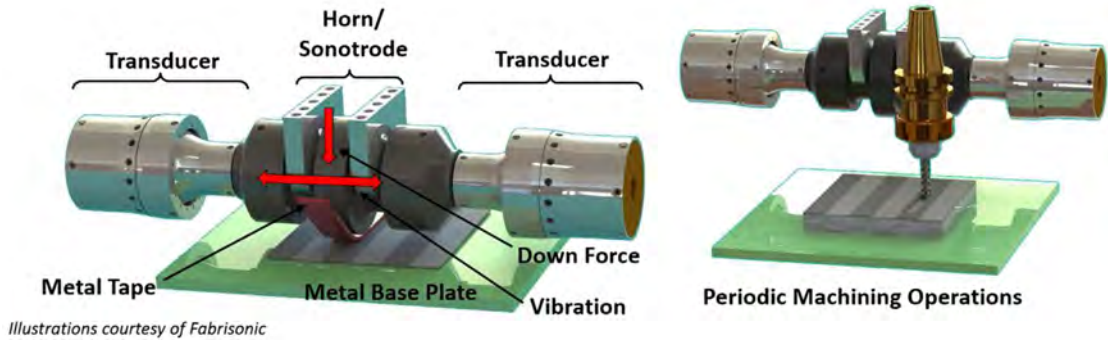


Figure 1.10: Illustration of a UAM machine (courtesy of Fabrisonic)

Sheet lamination processes involve the stacking of precisely cut metallic 2D foils to create a 3D part. A variety of joining methods have been tested and as of today *Ultrasonic Additive Manufacturing* (UAM) is one of the most used technologies in the field [21], originally commercialized by Solidica Inc. (USA) in 2000 and then licensed to Fabrisonic (USA). It involves bonding of thin metal foils (usually 100-150  $\mu\text{m}$ ) using *Ultrasonic Metal Welding* (USW) and integrates a *Computer Numerical Control* (CNC) machine to remove excess material and achieve the desired part geometry. In UAM a rotating sonotrode oscillates at around 20 kHz transversely to the direction of motion, applying a normal force to the metal foil and causing a localized welding. The technology is thus a prime example of *hybrid manufacturing*, as it incorporates novel AM approach of layer-by-layer construction with the close tolerances guaranteed by traditional CNC machining.

The key mechanisms enabling *Ultrasonic Metal Welding* are oxide fracture under pressure and plastic deformation of surface asperities. The combined action results in a very narrow weld region of less than 20  $\mu\text{m}$  presenting bulk temperatures far below melting. This allows the processing of highly heat-sensitive materials, as well as the possibility of creating multi-material parts by stacking layers of different materials, in order to locally achieve particular material properties, or to embed parts in the structure (embedded sensors or wires) [17] [32] [33].

## 1.4 Materials

Conceptually, AM allows to process almost any metallic material. In practice, however, only a limited number of materials have been used, although this number has been growing rapidly in the last few years [17]. Most AM processes require powdered raw material, notable exceptions being Wire-DED and UAM, thus limiting the process to the use of metals which can be effectively pulverized.

Nowadays the available metals range from low-melting materials such as gold or copper, to high-melting materials such as nickel superalloys. The most widely available materials include [22]:

- Gold
- Silver
- Copper alloys
- Aluminum alloys
- Tool steel
- Stainless steel
- Titanium alloys
- Nickel alloys
- Cobalt-Chromium alloys

The main issue regarding the feedstock materials in AM is the quality of the powder, determined by its morphology, size, shape, and density of the particles: distinct production techniques can lead to highly different properties and affect key powder qualities such as flowability and apparent density (defined respectively as the powder ability to flow freely without particles sticking to each other and as its capacity of closely compacting together when compressed) [3].

## **Powder Production**

Most of the available powder feedstock is manufactured through reliable and well-understood methods, such as water, rotary, gas or plasma atomization[21][34].

In all processes the metal is melted in a furnace, and then dispersed from a reservoir into an atomizing chamber.

The least complex production technique is *Water Atomization* (WA), which features high-pressure water jets that atomize a liquid metal free falling through an atomization chamber. However, this process yields coarse particles, which negatively affect both flowability and apparent density. Moreover, a marked increase in the oxygen content could lead to reactivity and oxidation problems [3].

*Rotary Atomization* (RA) does not cause any composition change, but results in highly irregular particle shapes, which make it unsuitable for AM as flowability and apparent density are both affected.

*Gas Atomization* (GA) reduces oxidation problems by using an inert gas as the atomization medium, and yields spherical particles having an increased flowability and apparent density; however, the kind of inert gas may influence the microstructure of the particles, and in turn that of the finished part [3]. The fundamental issues related to GA are increased porosity of the powder particles (due to entrapment of the gas), which will result in powder-induced porosity in the final part, and a marked presence of satellites on the spherical particles, which reduce flowability [21].

More costly and advanced production techniques, such as *Plasma Atomization* (PA) or *Plasma Rotating Electrode Process* (PREP), yield very fine particles, which highly improve the apparent density, with highly spherical and smooth shapes, which in turn improve flowability. [3] [21]. Actual particles resulting from various processes are reported in Figure 1.14.

### 1.4.1 Titanium Alloys

Conventional manufacturing of titanium alloys has always proved to be a costly, long and very complex process when carried out with traditional subtractive methods. The high performance of this material has led to its extensive use in AM, where the limitations posed by conventional processes do not apply. By far the most employed material is Ti6Al4V, which has been applied with success both in the biomedical and aerospace sectors because of its excellent mechanical properties and documented bio-compatibility [36] [37] [38].

### 1.4.2 Nickel Alloys

Nickel superalloys, Inconel 625 and 718 above all, have been of interest to the aerospace industry due to their outstanding balance of creep resistance, tolerance to damage, mechanical and chemical properties stability at high temperature. These characteristics make them the material of choice for high-temperature applications inside jet engines and gas turbines. Due to the high temperature required to process the materials their use is restricted mainly to EBM or high-power SLM.

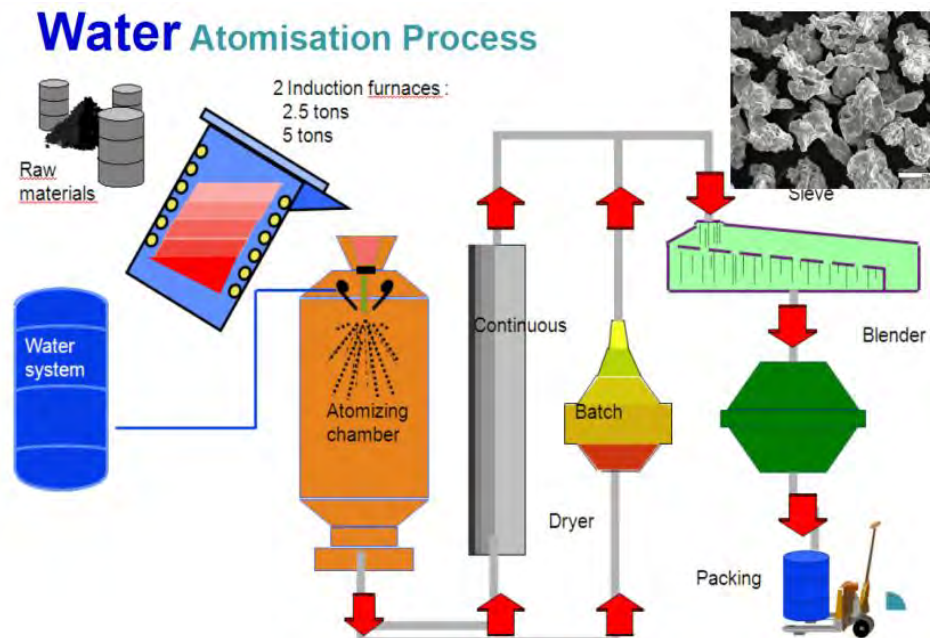


Figure 1.11: Schematic of Water Atomization process (courtesy of FCA)

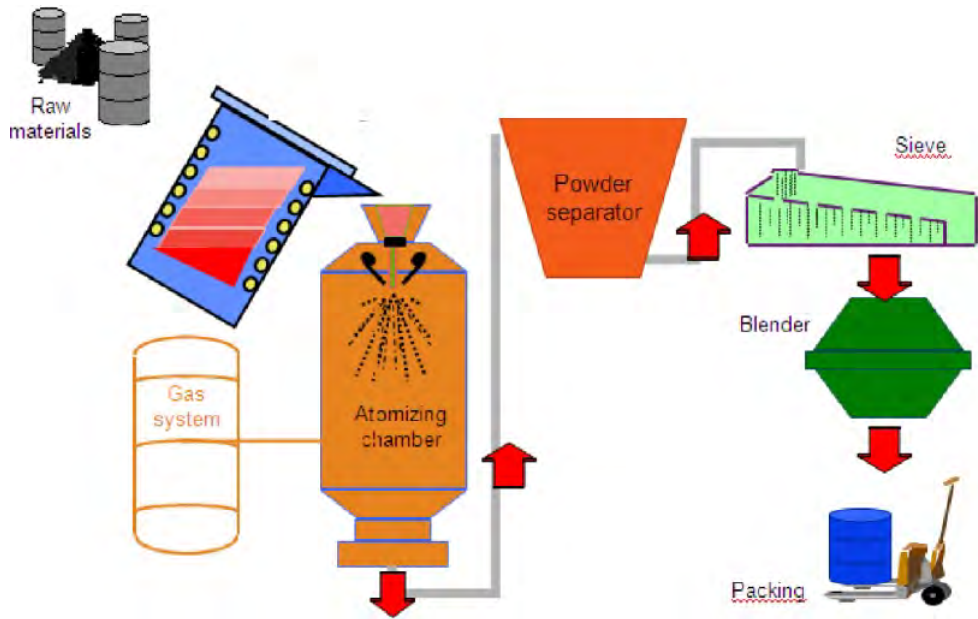


Figure 1.12: Schematic of Gas Atomization process (courtesy of FCA)

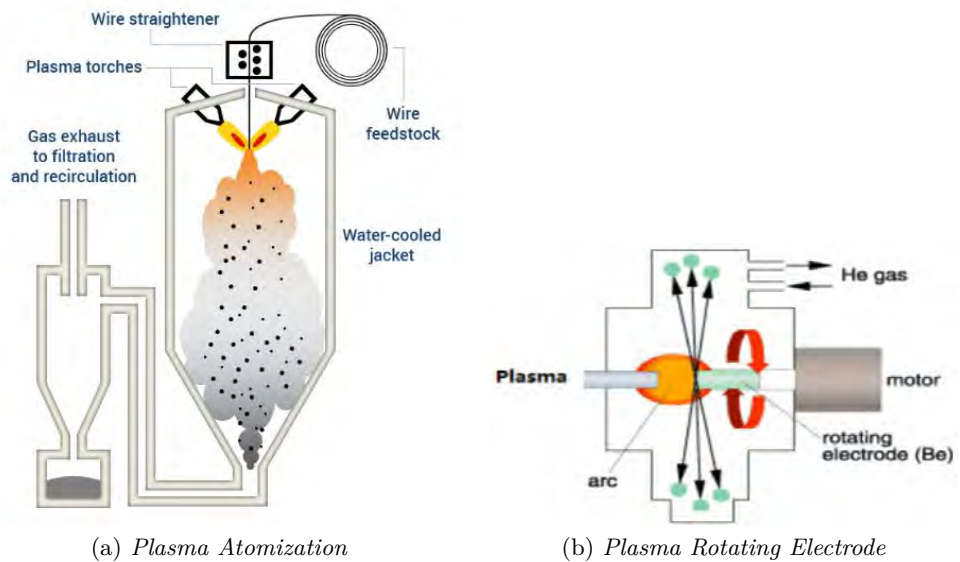


Figure 1.13: Schematic of PA and PREP processes (courtesy of FCA)

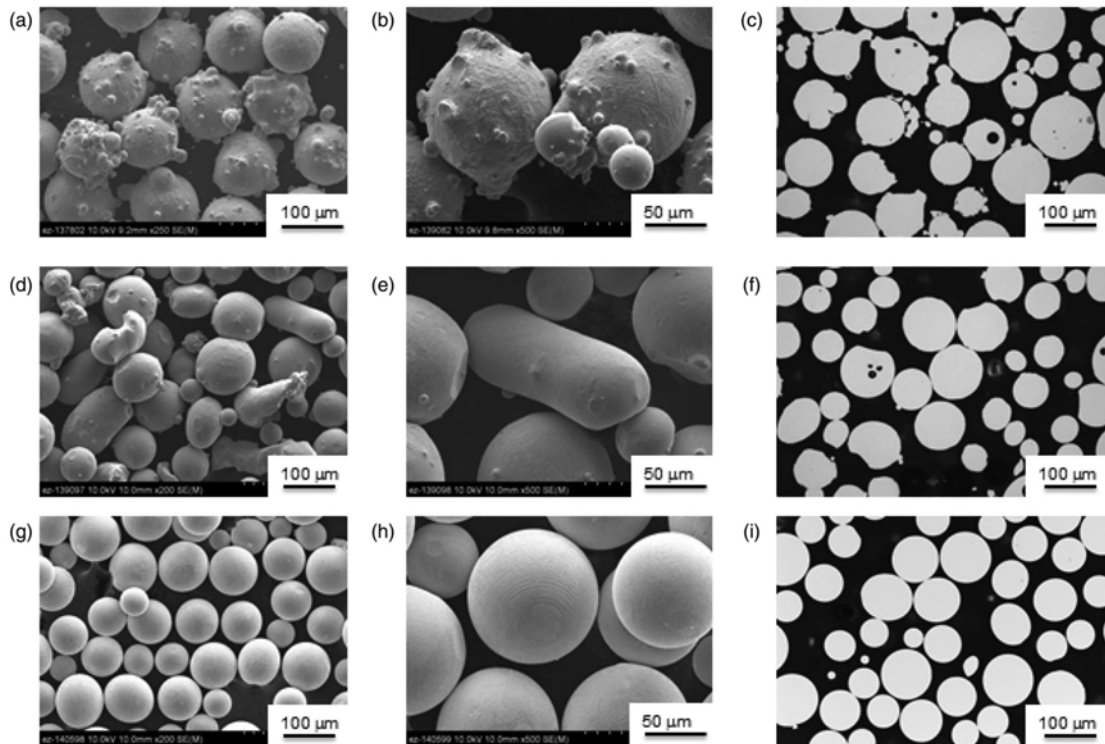


Figure 1.14: SEM images of powder particles produced with different techniques: a) SEM 250x of GA, b) SEM 500x of GA, c) LOM of GA, d) SEM 200x of RA, e) SEM 500x of RA, f) LOM of RA, g) SEM 200x of PREP, h) SEM 500x of PREP, i) LOM of PREP ([35])

### 1.4.3 Fe- Alloys

Steel, being still the most common engineering material, is obviously of high interest also for AM. Commonly available grades are austenitic stainless steels, maraging steels as well as tool steels. Since steel can be produced with many different microstructures depending on the chemical composition and thermo-mechanical processing, a high sensitivity to AM process parameters is to be accounted for, and is the subject of ongoing studies [3].

### 1.4.4 Aluminum Alloys

The development of Al-based alloys for AM has been more limited, mainly as aluminum parts are easy and inexpensive to machine even with traditional manufacturing methods. Moreover, due to the rapid cooling cycles present in AM, it is very complex to achieve significant precipitation hardening, which is the main strengthening mechanism in high-performance alloys. Another problem related to AM of Al alloys is that many alloying materials, such as Zn, Mg, Li easily vaporize, leading to increased porosity [3]. Moreover the high reflectivity of Al to the laser wavelengths usually employed in SLM creates another obstacle, increasing the required power to achieve full melting.

To reduce the influence of the aforementioned problems, alloys with high silicon content have been mostly used, as the small difference between solidus and liquidus temperature eases processing, and the high silicon % improves laser absorption and

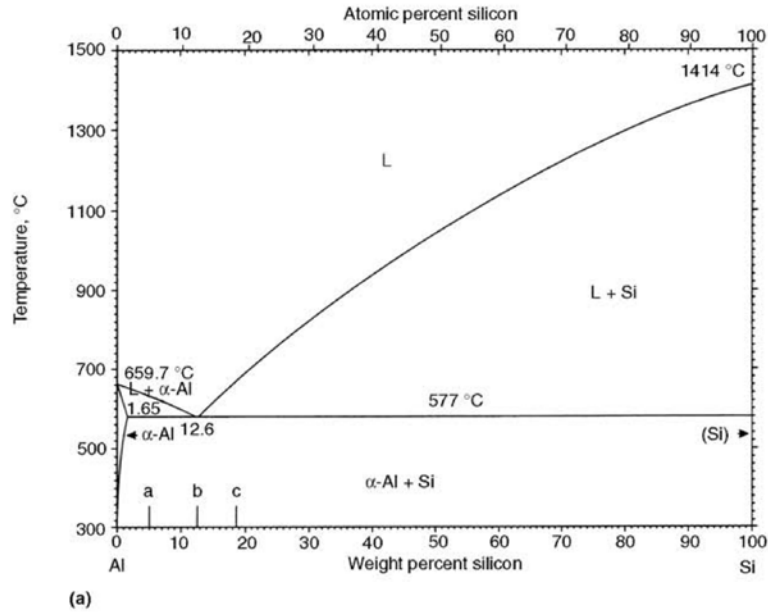


Figure 1.15: Al-Si phase diagram ([39])

reduces the chances of microstructural defects [40]. The most common alloys for SLM are, indeed, AlSi10Mg and AlSi12, both very close to the eutectic composition of 12.6 % [36] [37] [38].

## 1.5 Part Properties

Additive manufacturing processes offer the end user the possibility to tune a wide range of design and building parameters. Parameters such as powder dimensions and flowability, layer thickness, scanning speed and power, scanning strategy, build plate temperature, build chamber atmosphere all affect the final properties of the part in terms of its microstructure, density, surface finish, tensile and fatigue resistances. Particular attention has to be given to the *energy density*, given as in Eq. 1.1. Various studies have used this approach to study and model the resulting material microstructure, finding good correlations between machine parameters and part defects such as porosity and residual stresses [41][42][43].

In recent years, there has been extensive research effort to understand and parametrize all the machine settings, in order to model the process with the highest accuracy possible and prevent the formation of defects. In many cases however the knowledge is still limited and the ideal processing parameters are not available, and experience plays a major role in optimizing the process.

General characteristics of additively manufactured parts are the high tendency to present an anisotropic behavior, as a result of the layer-by-layer production, and the presence of non negligible porosity. The aforementioned issues, together with the main features of finished parts are here briefly reviewed, paying particular attention to the *Selective Laser Melting* (SLM) process.

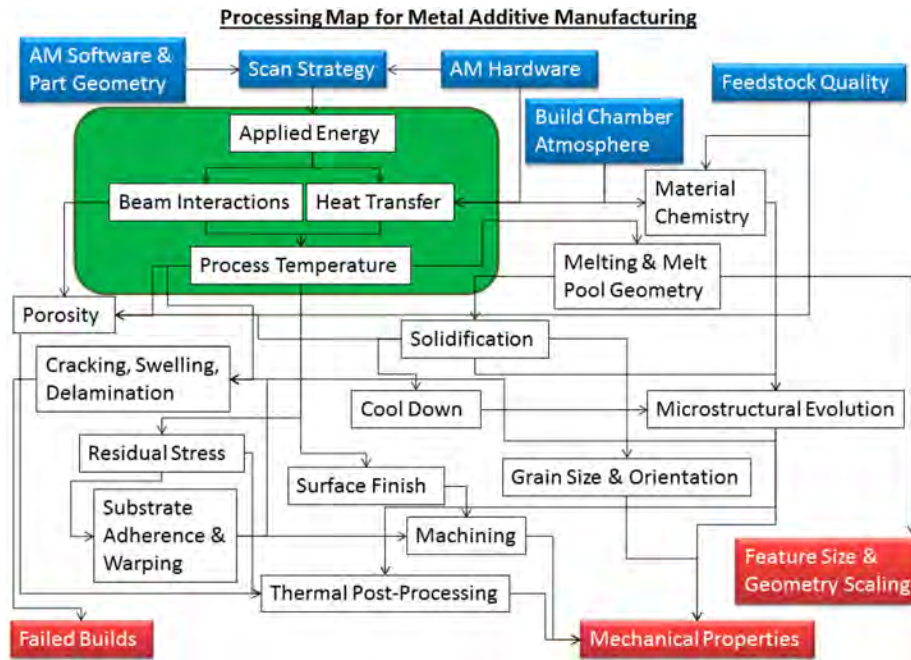


Figure 1.16: Relationship between input parameters and outcome of metal AM ([21])

### 1.5.1 Porosity

Porosity is a common issue with AM parts, which can negatively affect part properties. It has been shown that part densities of up to 99% can be achieved with optimized machine parameters and high-quality powders [44][10][21]. Final part density indeed can be influenced by powder-induced and process-induced porosity, each presenting characteristic morphologies and different causes.

Powder apparent density in its unprocessed state already has a big impact on final part density, with powders presenting higher apparent densities generally having improved performance. Also the powder compaction in the powder bed plays an influential role in final part properties, as the recoater arm delivers a decreasing powder compaction along its motion, thus impacting the final part density too [45]. Moreover, as previously reviewed in Section 1.4, gas pores might be entrapped inside powder particles during the gas atomization process, resulting in the formation of significant internal porosity in the part, characterized on average by a spherical shape [35].

Machine parameters (such as laser power, scanning speed, layer thickness, etc..) have to be optimized for each material, machine and build cycle. Considering layer thickness a fixed parameter throughout the build, as a function of the desired resolution and/or surface finish, it is possible to modify laser power, scanning speed and hatch distance in order to reduce the process-induced porosity.

A close relationship between laser power and scanning speed (exemplified in Fig 1.17) has been evidenced by multiple studies. Excessively fast scan speeds coupled with low laser power will not achieve an energy density high enough to allow for complete melting of the powder, leading to "lack of fusion" defects. On the contrary, an excessive amount of power at the speed of choice will generate overheating of the melt pool,

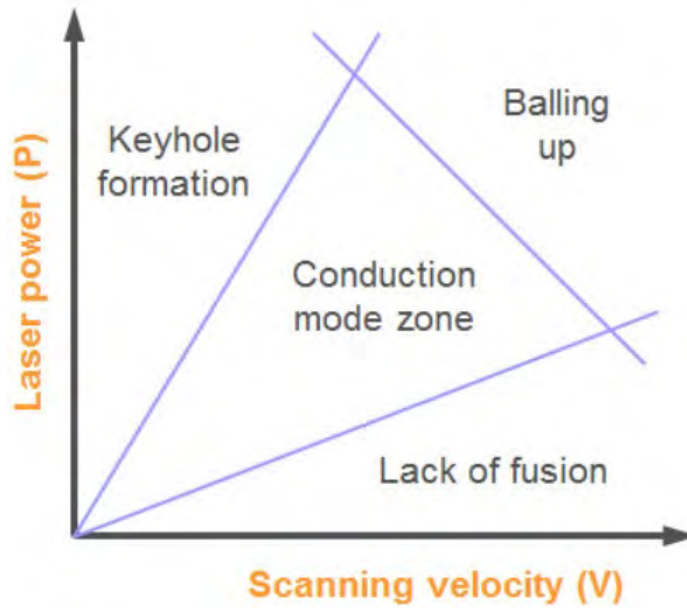


Figure 1.17: Typical relation between Laser Scanning Power and Velocity (courtesy of Renishaw)

resulting in "spatter" (ejection of metal vapors from the melt pool) and an effect known as "keyhole formation", where gas pores become entrapped at the base of the melt pool. An extreme condition might be created by applying very high laser powers at very high scanning speeds, resulting in pronounced instability of the melt pool which could cause voids to be left behind the trailing edge of the melt pool [21][43][46][41]. As a result of the motion on the laser, process-induced porosity is usually non-spherical and could be more dangerous as it induces higher stress concentrations inside the part.

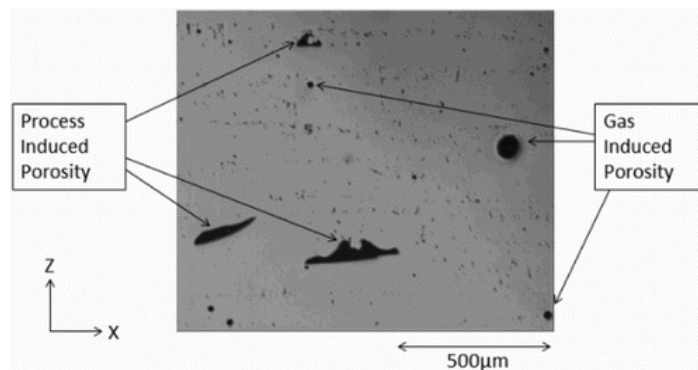


Figure 1.18: Comparison between process and powder-induced porosity ([35])

### 1.5.2 Scanning Strategy

The trajectory of the heat source during the build, layer after layer, is known as the *scanning strategy*. A number of different scanning strategies have been developed, as shown in Fig 1.5, each one optimized for particular processing techniques. Island scanning, a checkerboard pattern where alternating bidirectional tracks are used to fill the inside structure, and a subsequent contour pass is used to improve surface finish and

reduce porosity which could accumulate at the end of each individual laser track (example in Fig 1.19) [47][10]. Each layer is to be rotated by a certain *hatch angle* with respect to the previous one, in order to avoid an excessively directional microstructure and reduce defects concentration [11][43].

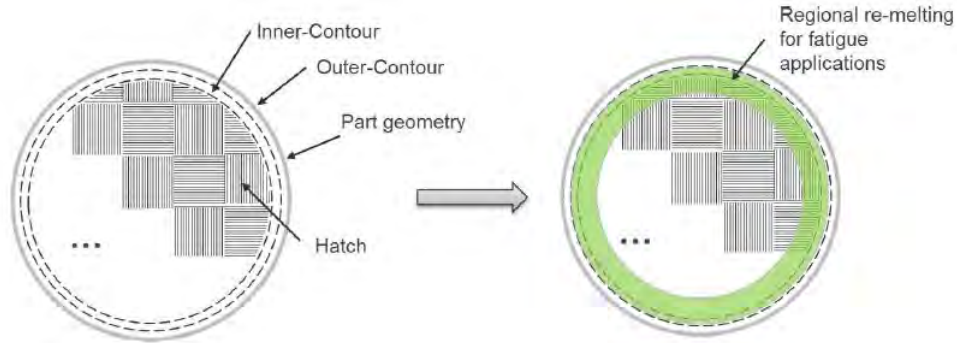


Figure 1.19: Proposed contour remelting ([10])

### 1.5.3 Residual Stresses

One of the main concerns in additively manufactured parts is the presence of non-negligible residual stresses throughout the material structure, which can severely impact industrial applications of AM. The highly localized energy input causes large thermal gradients (as in Fig 1.4) which are the main cause of residual stresses in AM parts. These stresses can dramatically affect the bulk behavior of parts, possibly causing distortions and even cracks in case the stress exceeds the local ultimate tensile strength of the material. Residual stresses largely depend on material properties, such as powder

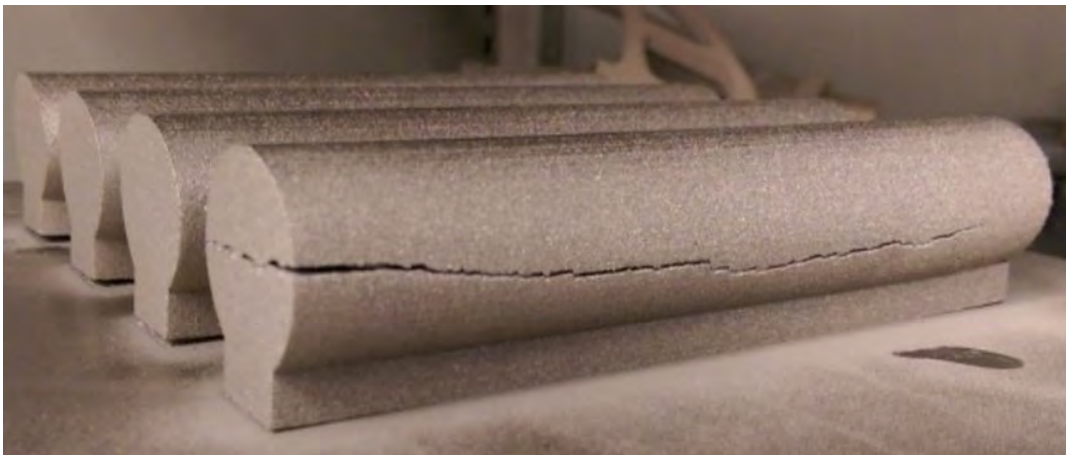


Figure 1.20: Example of severe part cracking after SLM processing (courtesy of Renishaw)

conductivity an thermal expansion coefficient; part geometry and support structure, with thin-walled parts being particularly at risk of deformation; process parameters and laser scanning strategy. The optimization of the machine parameters has been intensively studied, and many practical solutions aimed at reducing the severity of the

problem have been found: it has been proven that shorter laser tracks effectively result in lower residual stresses, thus indicating the island scanning strategy as the best one to reduce the problem, especially when coupled with low scanning speeds [48][49]. Another technique widely used to reduce residual stresses is the use of a heated build plate which is instrumental in reducing the thermal gradients throughout the build. A higher pre-heat temperature also increases atomic diffusion, resulting in the relief of internal strain energy.

The presence of non-negligible residual stresses, however, makes it necessary to prevent part distortion by using appropriate support structures, meant to dissipate heat from the build and to support and clamp overhanging features [50], as well as to adopt post-process stress relieving heat treatments. A stress relieving in the range of 250-300 °C for 2 h has been proven effective to reduce residual stresses in AlSi10Mg alloy [51][52]. Novel modeling techniques are also starting to enable the designer to compensate for the distortion by devising parts that will achieve the desired geometry after cooling.

#### 1.5.4 Anisotropy

One of the effects related to layer-wise manufacturing of metallic alloys is the creation of anisotropic mechanical properties. Although the issue might appear to be of secondary importance when compared with the presence of porosity and cracks inside the structure, it highly affects the actual performance of final AM parts, since their mechanical performance depends on their build direction [17]. The main cause of part anisotropy can be ascribed to directional heat conduction in the part during the build process: as layers are added in the z-direction, there is a complex thermal history that results in epitaxial grain growth along the build direction [40].

The microstructure of as-built parts presents elongated grains, along the build direction, and that is reflected in the mechanical properties of the finished part: multiple studies have evidenced significant differences in elongation and tensile strength depending on the build direction of the part [47][51][53][43][54]. This imposes a strict control and planning when choosing the build orientation of the part during the file manipulation phase, to maximize the properties of interest and to avoid premature failures.

Anisotropy, being related to the large thermal gradients inherent in AM, is heavily affected by the build parameters, and can be mitigated by varying the scanning strategy or applying appropriate base plate heating during the build. This will reduce the thermal gradients, and slow down the cooling of the part, enhancing atomic diffusion and the homogenization of the structure. Another technique to reduce the influence of anisotropy is the application of post-process heat treatments, designed to homogenize the material microstructure, resulting in more similar material properties in each direction [51][54][53].

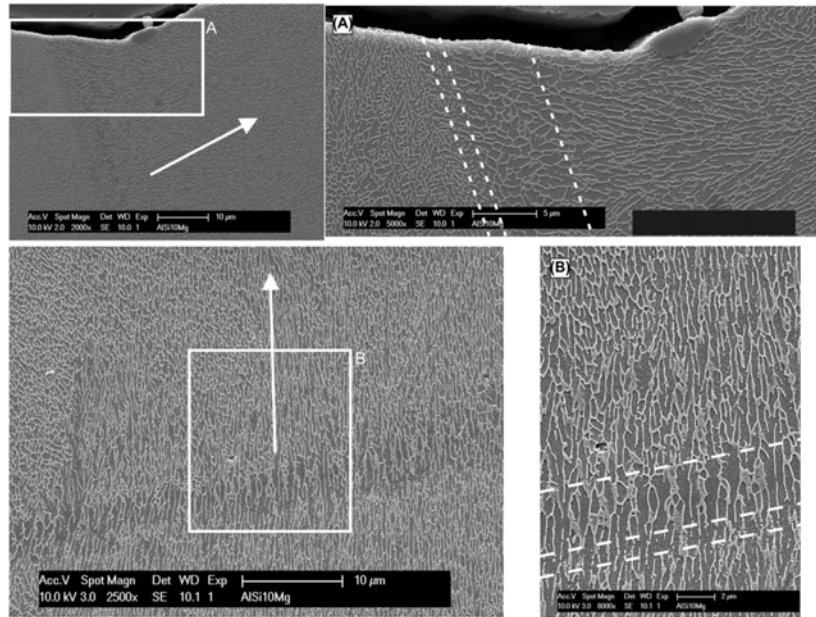


Figure 1.21: SLM AlSi10Mg microstructure showing elongated dendrites in the arrow direction. Graphs on the right are magnifications of areas in the white box ([55])

### 1.5.5 Microstructure

A small volume of the part will undergo a complex thermal cycle during manufacturing, with a rapid heating above melting temperature followed by rapid cooling, and many successive re-heating/re-cooling cycles as the laser will scan successive layers. As a consequence of these high thermal gradients, the final parts present a fine-grained microstructure, together with visible laser tracks (as in Figure 1.21), and considerable residual stresses.

Temperature gradients will be mainly influenced by the scan strategy, by the heat transfer coefficient of the surrounding material, by the supplied volume energy and by the eventual build plate pre-heating: scan strategies are highly material-dependent and also part-dependent, as different geometries require different scan paths to avoid overheating smaller features [3].

Moreover, the surrounding, non-melted powder will act as an insulator compared to the melt material, causing a highly directional heat conduction towards the build direction, resulting in elongated columnar grains (as seen in Figure 1.23) and anisotropic material properties [5]. Build plate pre-heating may be beneficial in reducing thermal gradients, thus reducing residual stresses, but may also cause a coarsening of the microstructure [5] [11].

Another distinctive feature of AM parts is the presence of pores throughout the bulk and the surface of the material (evident in Figure 1.22). They may originate from gas bubbles entrapped in the powder (powder-induced porosity) as well as from incomplete melting of the powder or evaporation of the melt pool (process-induced) depending on the level of applied volume energy (too low/too high).

The main goal and advantage of AM is to produce net-shaped parts, nevertheless it is

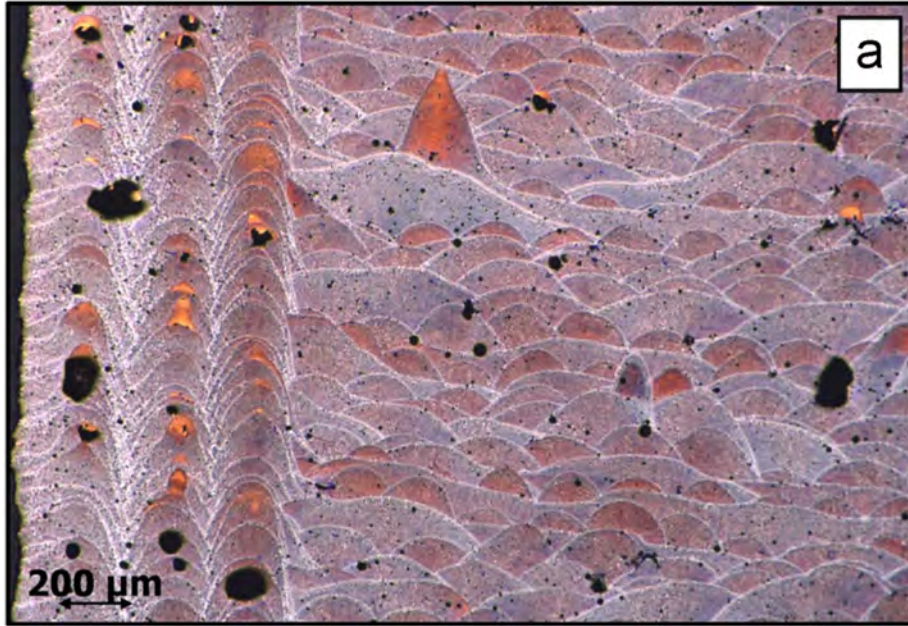


Figure 1.22: SLM AlSi10Mg microstructure, showing laser tracks, segregated Si-particles at grain boundaries and internal voids ([4])

possible to modify and improve the as-built microstructure with a range of post-process treatments aimed mostly at relieving residual stresses and/or reducing the remaining porosity.

### 1.5.6 Post-Process Treatments

In order to attain superior mechanical properties with respect to the as-fabricated parts, it may be necessary to use thermal or mechanical post-processing. Thermal post-processing is generally aimed at relieving the residual stresses, modifying the microstructure of the material or closing the residual pores. Mechanical post-processing on the other hand mainly aims at improving the surface finish of the part. A brief summary of the most common heat treatment processes is given in Table 1.5.

Stress relief can be achieved by heating the material to a high enough annealing temperature that allows for atomic mobility, but the duration of the process must be carefully regulated to avoid or otherwise control grain recrystallization and growth [21].

*Hot Isostatic Pressing* (HIP) is a process that permits to close residual internal cracks and pores present in the material microstructure by heating the material above 70% of its melting temperature in a very high-pressure environment (usually 100 MPa). The elevated temperatures will favor atomic mobility, and the high pressures will drive closure of pores by favoring gas solution inside the matrix [12]. The elevated temperatures will also favor grain growth [10]. The effects of these processes on the microstructure are exemplified in Figure 1.23 and Figure 1.24.

Mechanical post-process treatments have been shown to have an influence on mechanical properties of the material: shot peening of the specimens has been investigated by various authors [56][57], resulting in significant improvements of the mechanical prop-

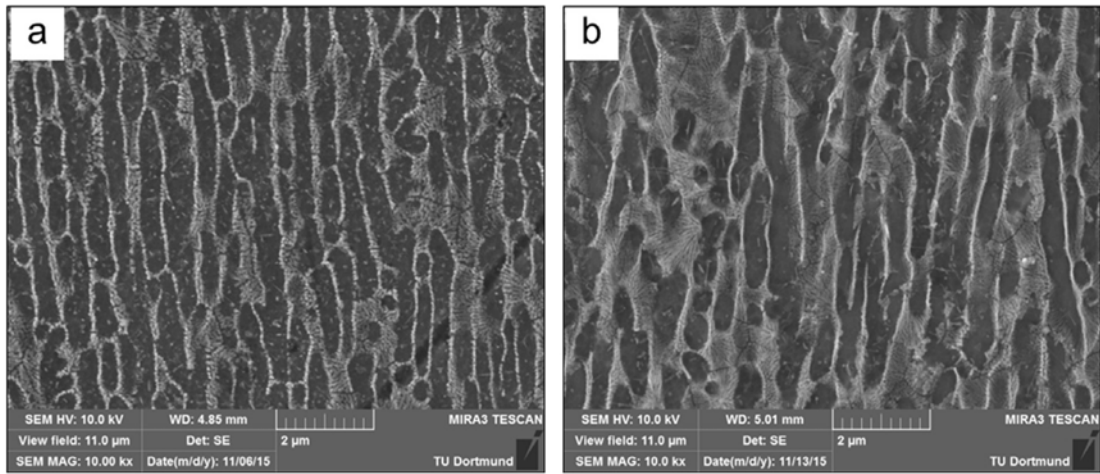


Figure 1.23: SLM AlSi12 microstructure with (a) and without (b) base plate heating, showing columnar dendrites along the build direction ([11])

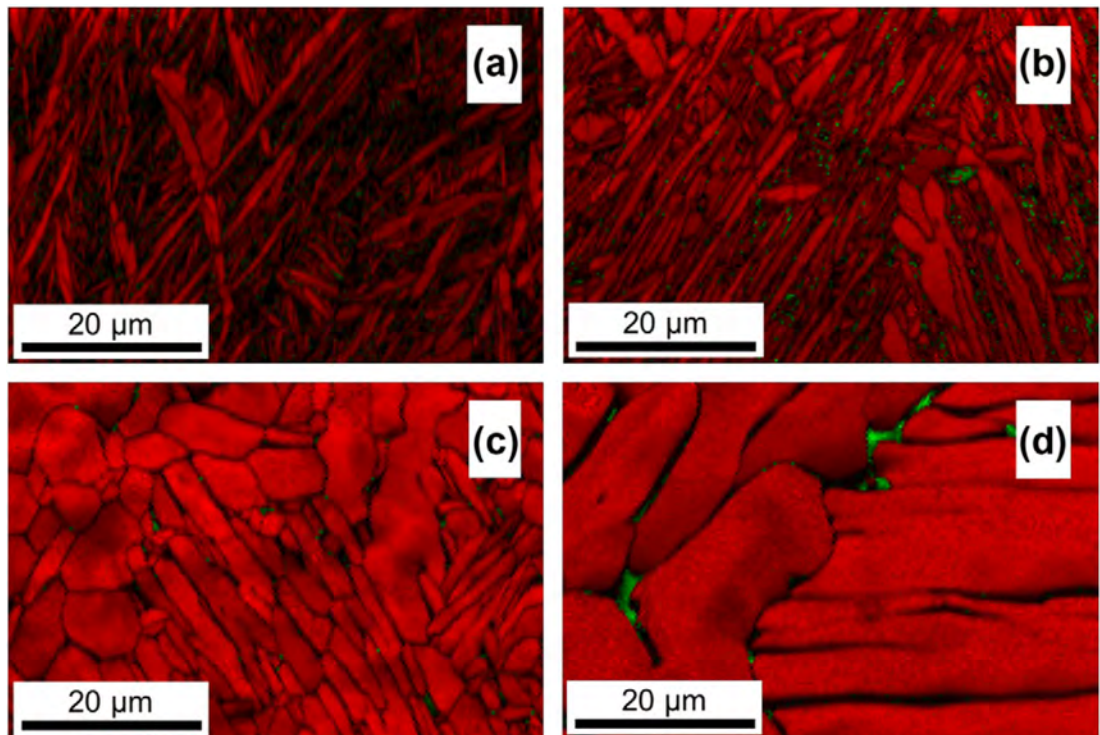


Figure 1.24: SLM Ti6Al4V microstructure for (a) as-built Ti6Al4V specimens, (b) following stress relief for 2h at 800 °C, (c) HIP processing, (d) 2h at 1050 °C ([5])

erties and fatigue strength of the material, while surface polishing has led to inconsistent results. In some cases it improved material properties [6], but the removal of the superficial layer may also cause exposure of underlying porosity, resulting in higher stress concentrations at the specimen surface [4].

Summarizing, materials for SLM:

- Require high-quality powder production
- Present fine-grained microstructure
- Retain considerable residual stresses and porosity
- Can be thermally post-processed to improve mechanical characteristics

Table 1.5: Typical heat treatment parameters

Treatment	Ti6Al4V	AlSi12 / AlSi10Mg
Stress Relief	650 – 1000 °C (2-4 h) [4][5] [6][9]	200 – 240 °C (2 h) [10][11] / 300 °C (2 h) [4]
<i>Hot Isostatic pressing</i> (HIP)	900 – 920 °C, 100 – 102 MPa (2 h) [4][5][6][12]	497 °C, 100 MPa (2 h)[10][12]

### 1.5.7 Economics of Additive Manufacturing

Additive Manufacturing is a young and disruptive technology, which is set to profoundly change the metals processing market. From a marginal market share in the 2000s, with a global market of less than 0.5 billion, it has already grown to a 5.5 bn EUR market in 2016, showing a *Compound Annual Growth Rate* (CAGR) of 20% over the 2004 - 2016 time period, and is expected to grow at least by a factor of two by 2022 [58]

The main problems related to the widespread diffusion of additive manufacturing technologies are the high manufacturing cost of components, mainly related to the high indirect costs associated with the process (labor and machining costs), and the high initial cost of AM devices and machineries due to the presently limited number of key AM systems manufacturers, mainly located in Germany. As a consequence a limited number of integrated service providers has developed, to the detriment of competition.

The AM applications have however expanded in several industries, with principal market segments being represented by the Aerospace, Automotive, Electronics and Medical industries. The business case for AM is made particularly clear when dealing with highly complex parts, which would require costly and lengthy manufacturing procedures. AM unlocks "free" complexity in parts, enabling innovative and optimized designs which can achieve high savings for the end user. A business case made for an aerospace component as simple as a seat steel buckle showed potential savings of over 2 million EUR over the lifetime of the aircraft [31]

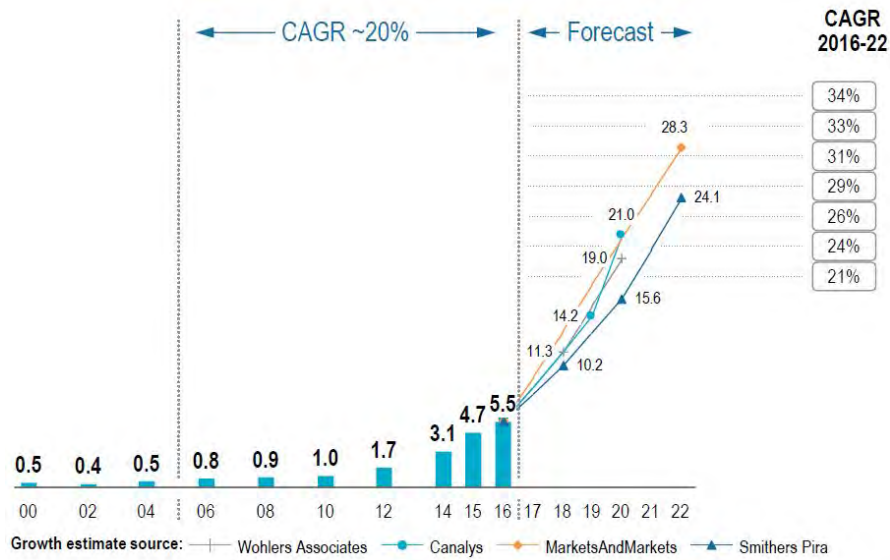


Figure 1.25: Development of metallic AM (2000-2022) world production, excluding parts and accessories ([58])

When dealing with additive manufacturing technologies it is assumed in a first approximation that unit manufacturing costs (excluding design costs) are independent of production volume, whereas with traditional production processes an inverse relation can typically be found. The break-even point between conventional manufacturing processes and additive manufacturing can be found for low- to medium-sized production lots, where AM can achieve considerable savings since there would be no need for costly equipment such as molds, dies, etc.. [59].

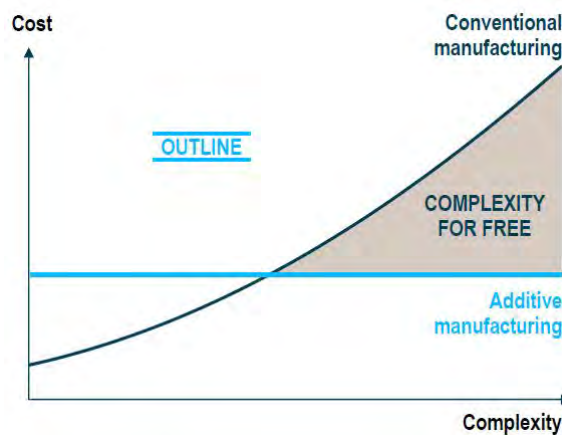


Figure 1.26: AM part complexity vs. part manufacturing cost ([31])

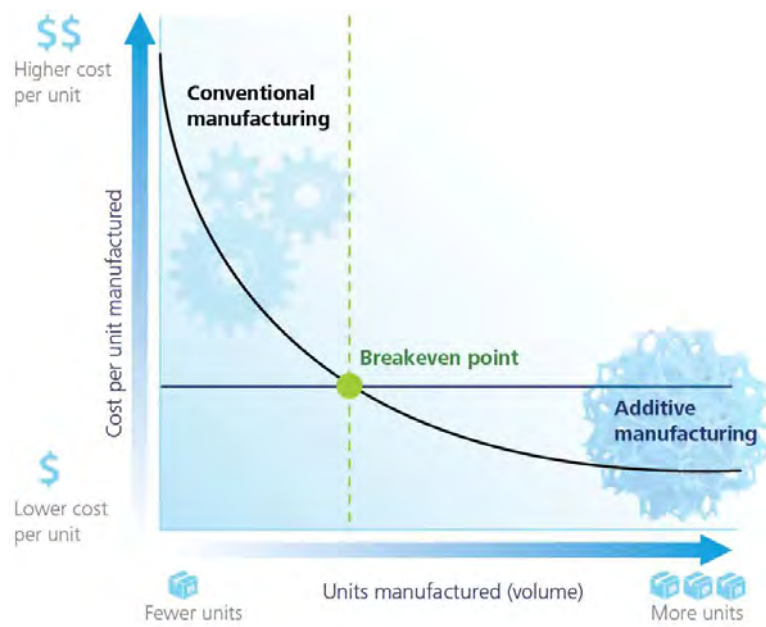


Figure 1.27: AM break-even point compared to conventional manufacturing on the base of manufacturing volume ([59] )

# Chapter 2

## Literature Review

### 2.1 Testing Procedure

The papers reviewed in this chapter focused their attention on fatigue and fracture characterization of printed materials, whilst providing results for static tests as well. An important work of correlation between microstructure defects and mechanical properties is also reported. Fatigue tests in both *High Cycle Fatigue* (HCF) and *Low Cycle Fatigue* (LCF) ranges were reportedly performed with hour-glass specimens according to ASTM E466 [60] with load ratios of  $R = \frac{\sigma_{min}}{\sigma_{max}} = 0.1$  or  $R = -1$  [53] [7]. Crack growth rate tests were performed with specimens according to ASTM E647 [61] mostly with stress intensity factor ratios of  $R = 0.1$ . Along with traditional analysis such as metallography and fractography, advanced non-destructive techniques for porosity evaluation such as *Computed Tomography* (CT) scanning have also been employed [10].

### 2.2 Titanium

#### 2.2.1 Microstructure

A fine-grained microstructure, composed of lamellar  $\alpha + \alpha'$  martensitic phases created due to the extremely rapid cooling rates of AM, has been widely observed in the as-built state [5], with clearly elongated grains in the z-direction (i.e. normal to the build layers) [6] as in Figure 2.1 a. Such a microstructure leads to very high tensile strengths but also causes a marked brittle and anisotropic behaviour. To improve elongation to failure it is usual practice to heat-treat the part, either with stress relief annealing or HIP. Different stress relief parameters have been investigated by Leuders et al. [5], varying annealing temperature from 800 to 1050 °C. A lower temperature, 650 °C, was proposed by Chastand et al. [6], as well as by Wycisk et al. [62]. Processes at higher temperatures lead to more evident grain coarsening (Figure 1.24b/d), with a decomposition of the martensitic  $\alpha'$  phase into an  $\alpha + \beta$  structure with  $\beta$  phase segregated at grain boundaries. Stress relief at lower temperatures returns a finer  $\alpha + \alpha'$  lamellar microstructure (Figure 2.1c) but does not completely remove material anisotropy, with evident columnar grains, resulting from preferential heat conduction along the build direction, still clearly visible

(Figure 2.1a). HIP parameters show much higher consistency, with most of the literature reporting 920 °C, 1000 bar to be the most appropriate for Ti6Al4V alloy. HIP treatment results not only in stress relief but also in an important porosity reduction: the microstructure shows a moderate grain coarsening, with lamellar  $\alpha$  grains, with limited increase of the  $\beta$ -phase [6] [62] [5]; porosity reduction is evident from CT scans (Figure 2.2), reducing stress concentration effects.

### 2.2.2 Tensile Properties

Heat treatments highly influence mechanical properties: the as-built condition presents brittle characteristics, with very high *Ultimate Tensile Strength* (UTS) values, in the range of 1030-1130 MPa, but the elongation to fracture can be as low as 1.2%. The as-built condition is also marked by anisotropy, with stresses perpendicular to the build layers causing premature failure [4]. Stress relief treatments and HIP alike cause a reduction of UTS, but permit to obtain higher elongation to failure values. And, HIP especially, almost eliminates the anisotropy [4][5].

### 2.2.3 Fatigue Properties

The observations made for static properties hold also for fatigue behaviour: as-built specimens show reduced fatigue resistance, while specimens subjected to additional heat treatments show a substantial improvement in performance. Leuders et al. [5] report fatigue lives, for fully reversed bending (R=-1), as low as 27000 cycles for as-built specimens, while stress relieving at 800 °C increases endurance up to 93000 cycles, and HIP provides infinite life at  $2 * 10^6$  cycles, with a calculated fatigue strength of 630 MPa, which is in line with the values of wrought materials (i.e. 630-680 MPa).

Further analyses from Mower et al. [4] as well as by Wycisk et al. [9] confirm these trends, reporting a significant enhancement of fatigue strength after HIP and pore closure, with fatigue strength values, under tension-compression testing, of 400 MPa and 575 MPa respectively, pointing to the importance of pore closure for the improvement of fatigue life. A significantly lower scatter of data is also evident (Figure 2.3). Fractographic analyses confirm that fracture-initiation sites are mostly related to porosity defects, unmelted zones or surface defects, with defects closer to the surface proving to be the most critical [5][4][9](Figure 2.4).

### 2.2.4 Crack Growth

Conventionally-processed material has a reference threshold value  $\Delta K_{th} = 4MPa\sqrt{m}$ . Tests performed by Leuders et al. [5] on CT specimens show a considerable scatter of  $\Delta K_{th}$  for the as-built specimens, with threshold values found to be consistently lower than the reference. A significant improvement can be obtained by heat-treating the parts, with threshold values even higher than the reference at  $\Delta K_{th} = 6.1MPa\sqrt{m}$ . It has also been observed how build orientation affects specifically the as-built parts, which show markedly different behaviors in the Paris-Erdogan region (Figure 2.5). This

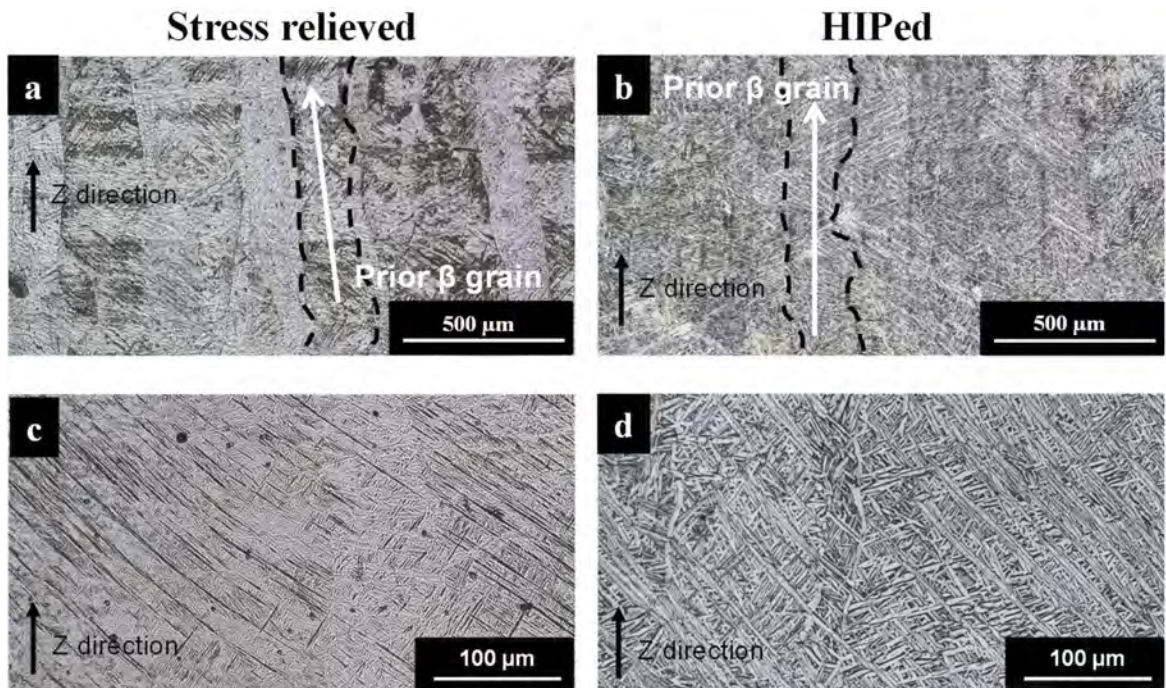


Figure 2.1: Optical micrographs of SLM Ti6Al4V specimens at different magnifications in the X-Z plane. (a, c) Stress Relieved (b, d) HIPed. ([6])

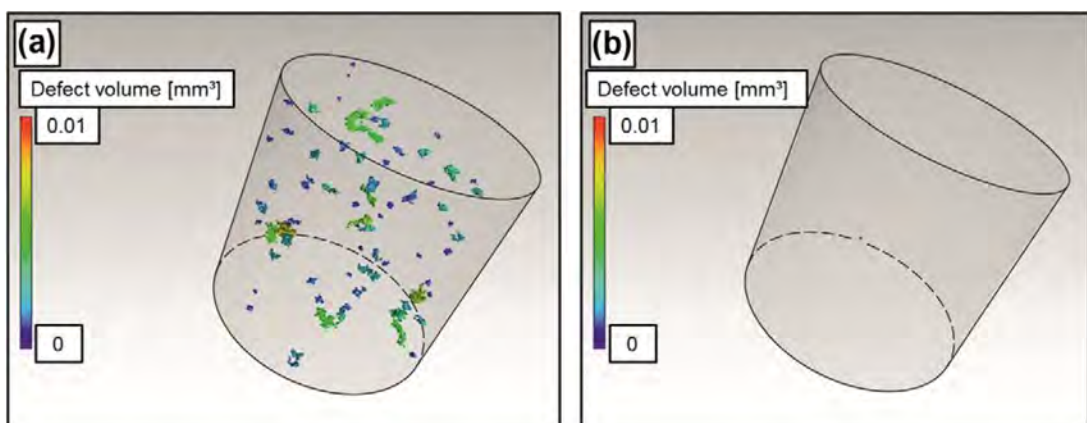


Figure 2.2: CT of (a) as-built Ti6Al4V specimens, and (b) after HIP processing. After the HIP process, any residual porosity was below the resolution limit ([5])

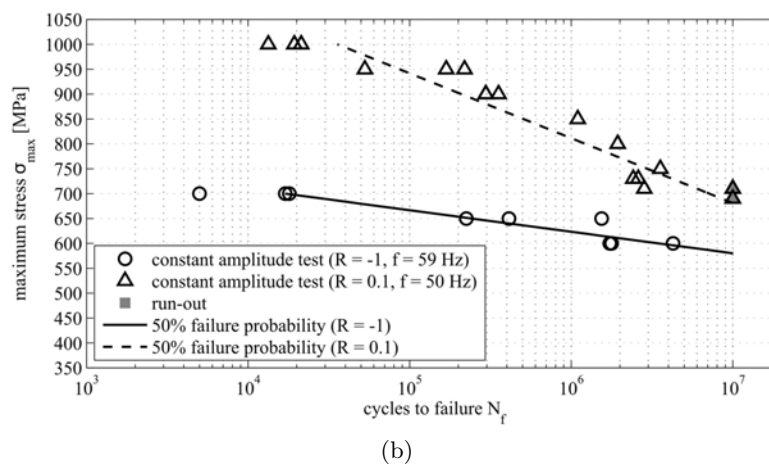
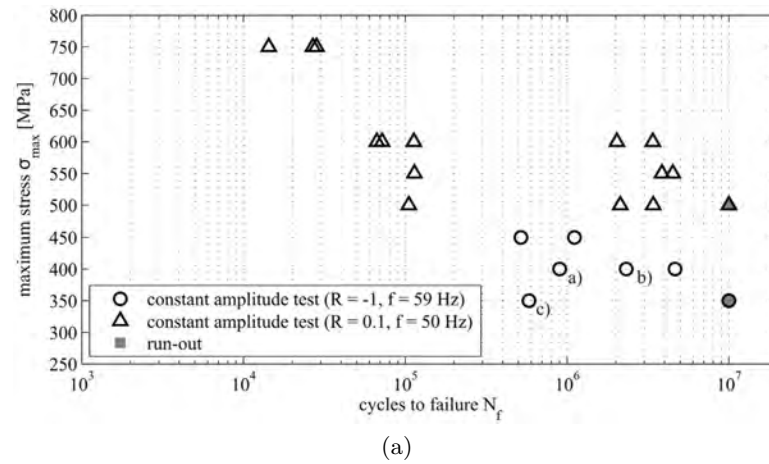


Figure 2.3: HCF properties for (a) stress-relieved and (b) HIPed Ti6Al4V specimens ([62])

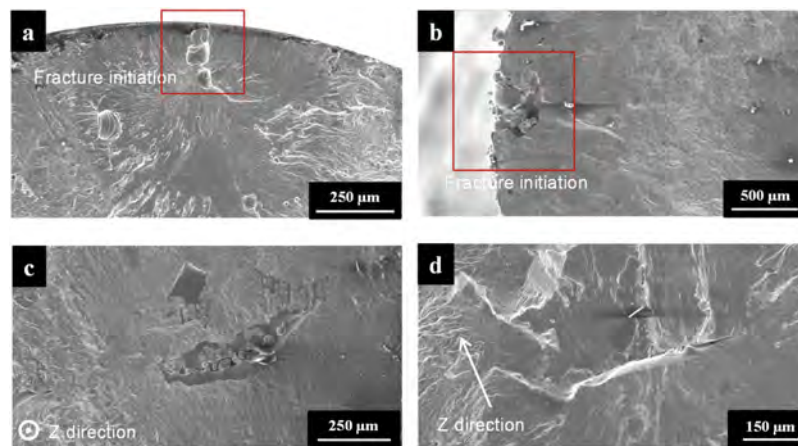
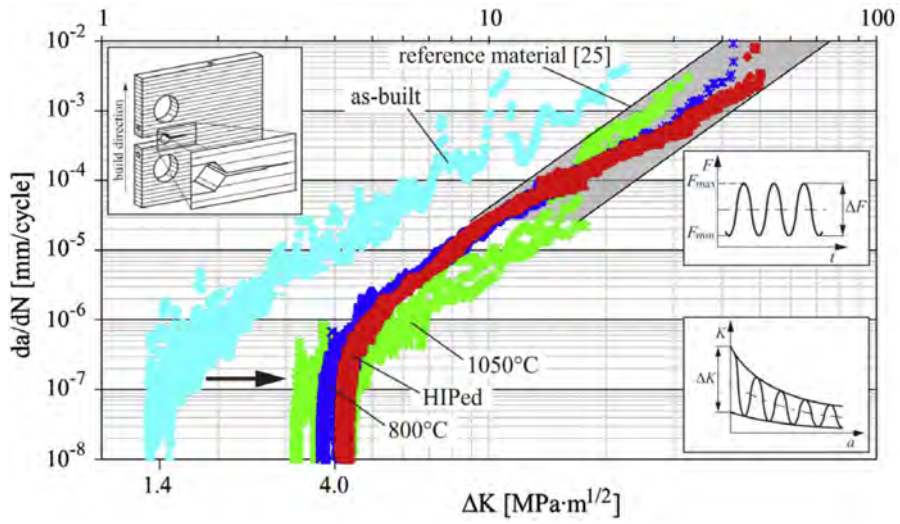
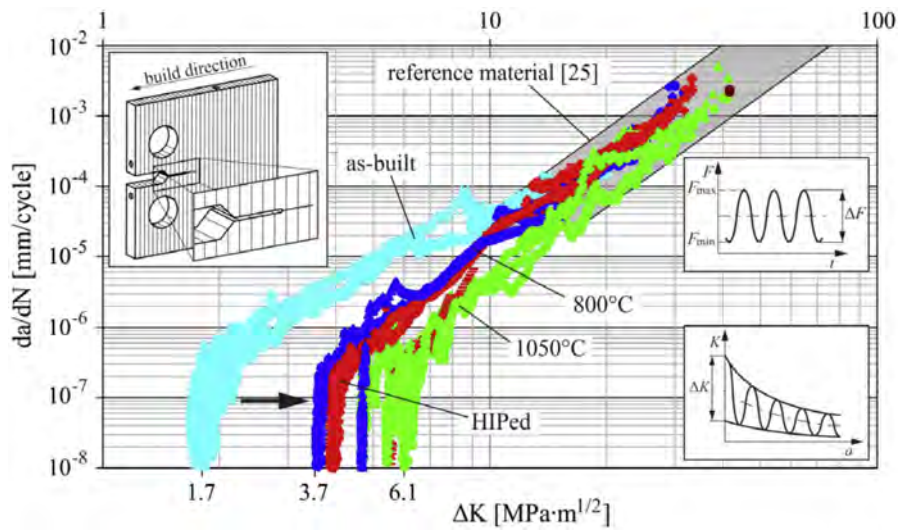


Figure 2.4: Fractography of different defects: (a) porosities, (b) surface defect, (c)(d) unmelted zones/bonding defects ([6])



(a)



(b)

Figure 2.5: Crack growth curves for SLM Ti6Al<sub>4</sub>V alloy. (a) Crack growth perpendicular to build direction, (b) Crack growth parallel to build direction. Scatter band shows reference material properties. ([5])

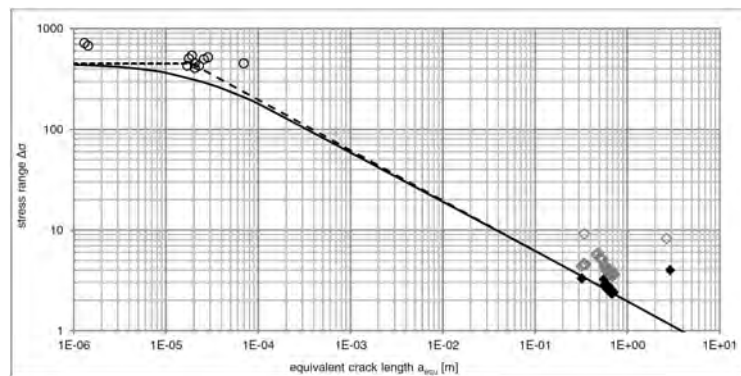


Figure 2.6: SLM Ti6Al<sub>4</sub>V Kitigawa-Takahashi diagram on experimental data from HCF and crack propagation tests. ([9])

could point at the importance of residual stresses: high tensile stresses were reported for the as-built specimens in the build direction, while hardly any were measurable in the heat-treated materials [5]. Comparable results have also been obtained by Wycisk et al, who calculated a  $\Delta K_{th} = 3.48 MPa\sqrt{m}$  for stress relieved specimens [9]. Wycisk et al. performed also a *Linear Elastic Fracture Mechanics* (LEFM) analysis to correlate defect size with the stress range adopting both Kitigawa-Takahasi and El Haddad-Topper approaches and found a good correlation of experimental results with the models (Figure 2.6). Extensive literature review on the subject has been performed also by Beretta et al. [7].

## 2.3 Aluminum

### 2.3.1 Microstructure

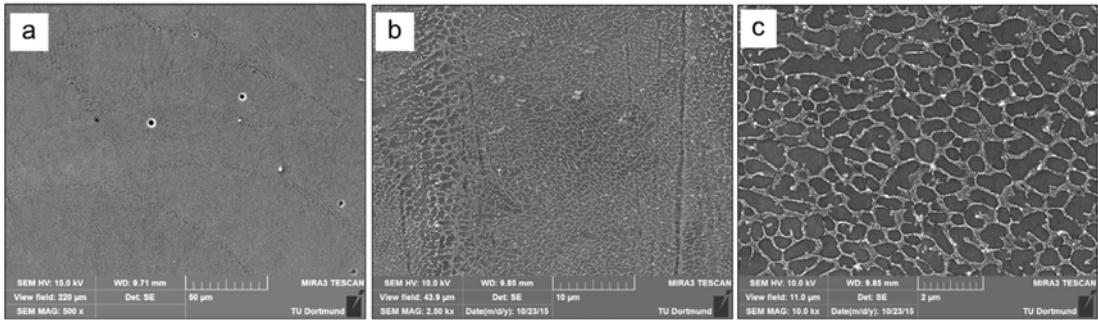


Figure 2.7: SLM AlSi12 microstructure, showing fine dendrites perpendicular to the build direction ([11])

SLM returns very fine microstructures also when aluminum alloys are employed, with columnar dendritic structure growing in the build direction for both AlSi12 and AlSi10Mg alloys [11][4][47]. Laser tracks are evident (Figure 1.22) and Si-particles can be seen at the grain boundaries, as a result of high cooling rates, which prevent the formation of precipitates (see Figure 1.23, Figure 1.22 and Figure 2.7). Precipitation-hardening alloys such as AlSi10Mg, necessarily require post-process heat treatments to allow precipitation of Mg<sub>2</sub>Si to form at the grain boundaries [53].

As with Ti-alloys, heat treatments also give rise to a grain coarsening effect, remove material anisotropy and give a stress-relief effect [21]. Build platform heating to 300 °C and peak-hardening processes to T6 condition have been studied by Brandl et al. [53], which found peak-hardening to have substantial effects on the removal of anisotropy thanks to microstructure homogenization, and platform heating to cause a reduction of internal defects [53]. Similar conclusions were reached by Siddique et al. [11], who observed a reduction in porosity from 0.25% to 0.12% with a platform heating up to 200 °C (Figure 2.8).

Stress relief annealing to 240 °C has been investigated by Siddique et al. [11], which, along with an expected grain coarsening and stress-relief, observed an increase in pore size due to the increased ductility at elevated temperatures, causing entrapped gases to

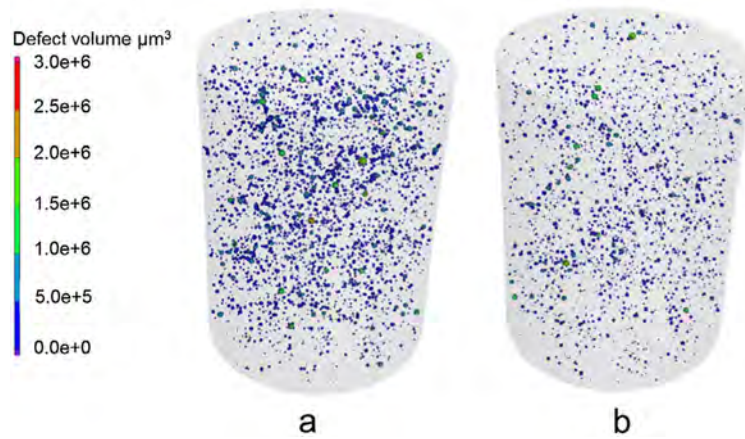


Figure 2.8: SLM AlSi12 CT scans of stress-relieved specimens (a) without and (b) with base-plate heating ([11])

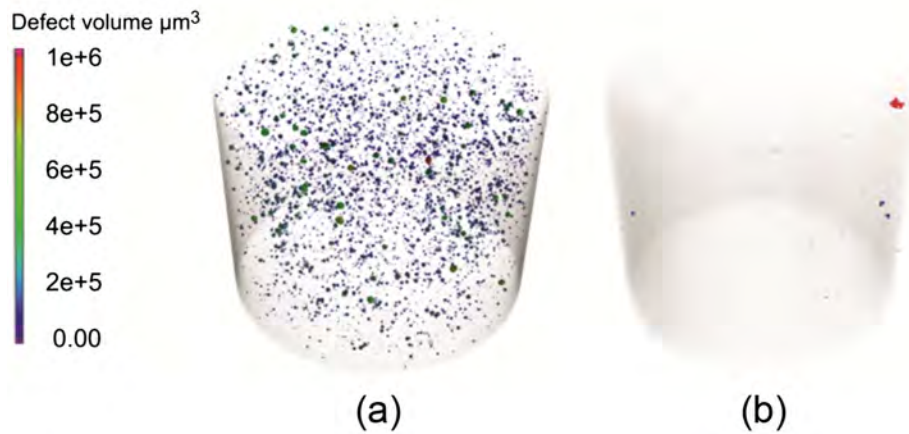


Figure 2.9: SLM AlSi12 CT scans: (a) Stress-relieved, and (b) HIPed ([10])

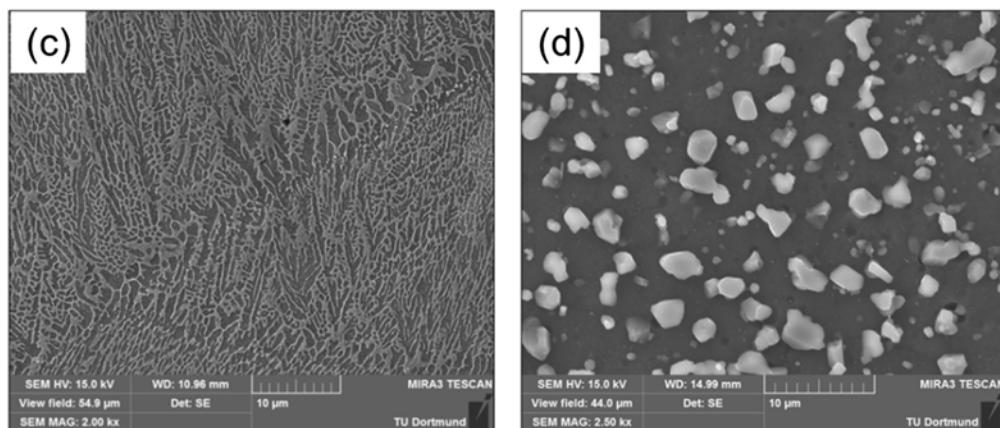


Figure 2.10: SLM AlSi12 surface micrographs: (c) Stress-relieved with Si-deposits at grain boundaries, and (d) HIPed with accrued Si-crystals ([10])

expand more freely. Similar tests were performed by Mower et. al, although porosity and bonding defects remained evident, which lead to brittle fracture and anisotropic behavior [4].

HIP was investigated by Siddique et al. [10], observing a completely recrystallized structure without dendrites and with Si-crystals accrued in the Al-matrix, together with a dramatic reduction in porosity, from 0.30% to less than 0.01% (see Figure 2.9 and Figure 2.10).

### 2.3.2 Tensile Properties

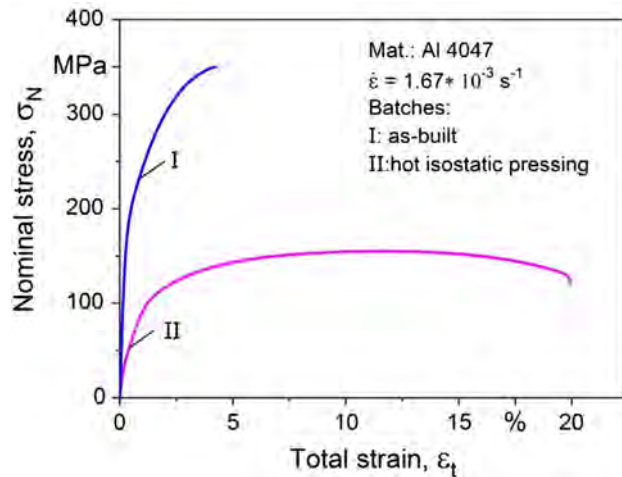


Figure 2.11: SLM AlSi12 characteristic stress-strain curves for (I) as-built and stress relieved and (II) HIPed specimens ([10])

Quasistatic properties of Al alloys show similar behaviour to SLM Ti alloys with respect to the microstructure/elongation relationship. The very fine grains resulting from the rapid cooling cycles of AM process lead to increased strength values with respect to wrought materials, albeit with a reduced elongation at failure.

Siddique et al. [10] report UTS values of 361 MPa for AlSi12 specimens in the as-built condition, or around 275% of the value for the reference cast alloy, but with a halved elongation to failure of about only 4%. HIPed specimens show roughly halved UTS, at 155 MPa, but also present an excellent elongation to failure of 19.2% as in Figure 2.11.

Despite the difficulty in forming precipitates due to rapid cooling rates, precipitation-hardening alloys such as AlSi10Mg produced by SLM show comparable strength with cast parts in the as-built condition. Kempen et al. [47] observed UTS of around 390 MPa in as-built specimens, which exceed even *High Pressure Die Casting* (HPDC) properties (UTS=300-365 MPa). They also observed elongation to failure values in the same range as the HPDC parts ( $\epsilon_f = 3 - 4\%$ ), albeit with a marked anisotropy. Parts tested along the build direction failed prematurely due to increased influence of internal pores.

These findings were confirmed by studies from Mower et al. [4], who observed anisotropy even after a stress-relieving heat treatment (see Figure 2.12) and a markedly

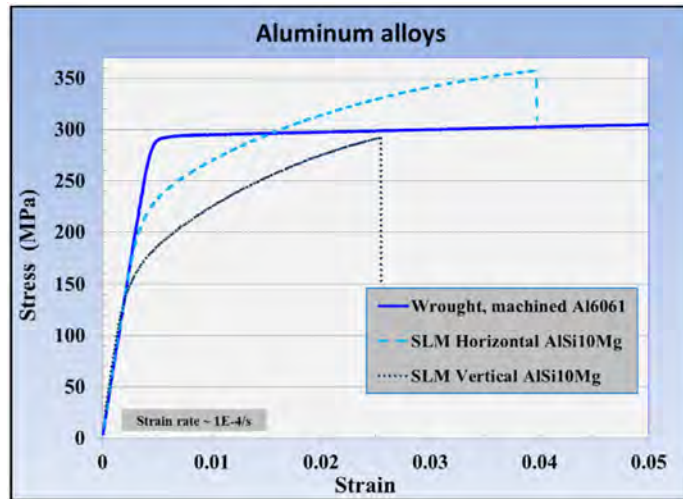


Figure 2.12: SLM AlSi10Mg characteristic stress-strain curves for stress relieved specimens in Z- and XY-direction, compared to cast material ([4])

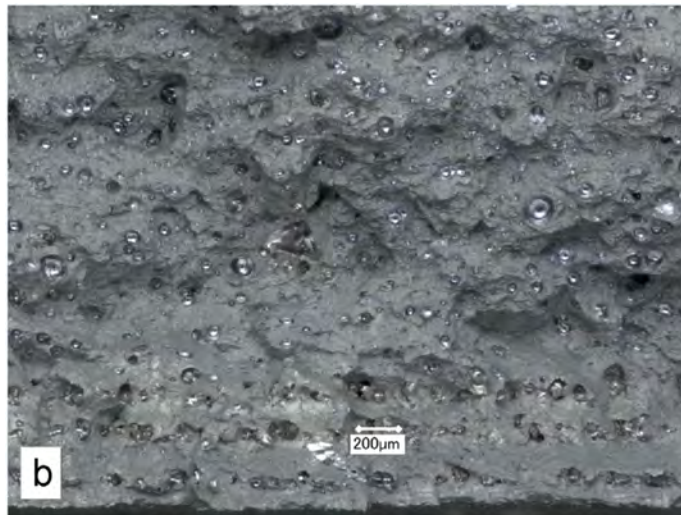


Figure 2.13: SLM AlSi10Mg tensile specimen brittle fracture surface, with evident porosity ([4])

brittle and faceted fracture surface, with evident porosity defects as shown in Figure 2.13.

### 2.3.3 Fatigue Properties

Fatigue behavior is highly influenced by microstructural properties. Siddique et al. [63] observed evident differences in the behavior of stress-relieved AlSi12 specimens with and without base plate heating. The reduction in internal defects resulting from base plate heating gives noticeably higher fatigue strength values as shown in Figure 2.14.

Fracture surface analysis confirms how specimens without base plate heating failed predominantly due to large sub-surface flaws, with non-uniform distribution of pores causing a significant scatter of the data, while in the other batch, surface defects were the main crack-initiation sites [11]. In any case, both batches showed fatigue strengths

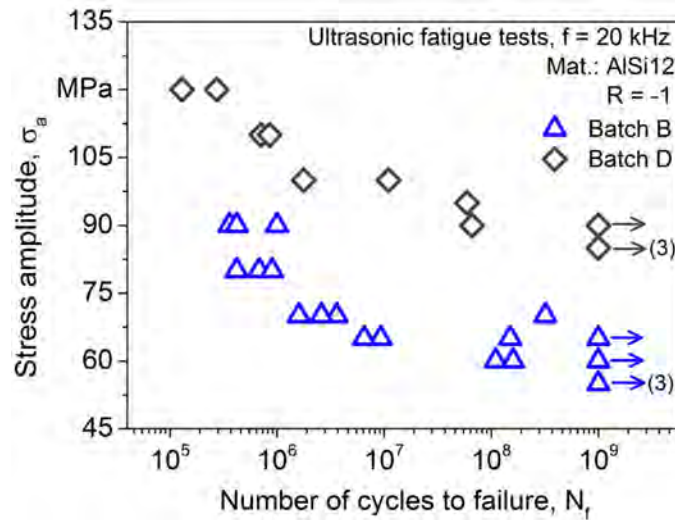


Figure 2.14: Wohler diagrams for AlSi12 stress-relieved specimens with (batch D) and without (batch B) base plate heating at 200 °C ([63] and [11])

greater than, or comparable to, a conventional cast alloy, usually rated at 55 MPa [11].

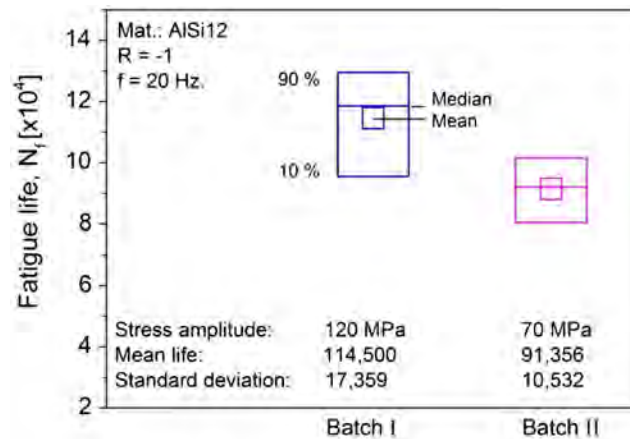


Figure 2.15: Constant amplitude test fatigue life of AlSi12 specimens (I) with base plate heating and (II) with HIP ([10])

HIP post-treatment, while virtually eliminating any porosity, also increases grain size as previously noted (Section 2.3.1). Additional studies from Siddique et al. [10] reported a reduced scatter of data for HIPed specimens, but also denoted a marked reduction of fatigue resistance: the elimination of sub-surface defects reduces the possible initiation sites to surface defects only, but finer grains offer higher crack initiation resistance, resulting in the behaviour shown in Figure 2.15.

Precipitation-hardening alloys like AlSi10Mg mostly benefit from peak-hardening treatments as shown by Brandl et al. [53]: peak-hardened specimens show consistently improved fatigue strength, independently of the build direction (see Figure 2.16), outperforming the wrought material (rated at 60-90 MPa).

Fracture surface analysis reveals that all peak-hardened specimens show ductile fractures, as opposed to the brittle fracture surfaces of as-built specimens as shown in Figure 2.17. Further analysis by Brandl et al. [53] on the effects of base plate heating denotes

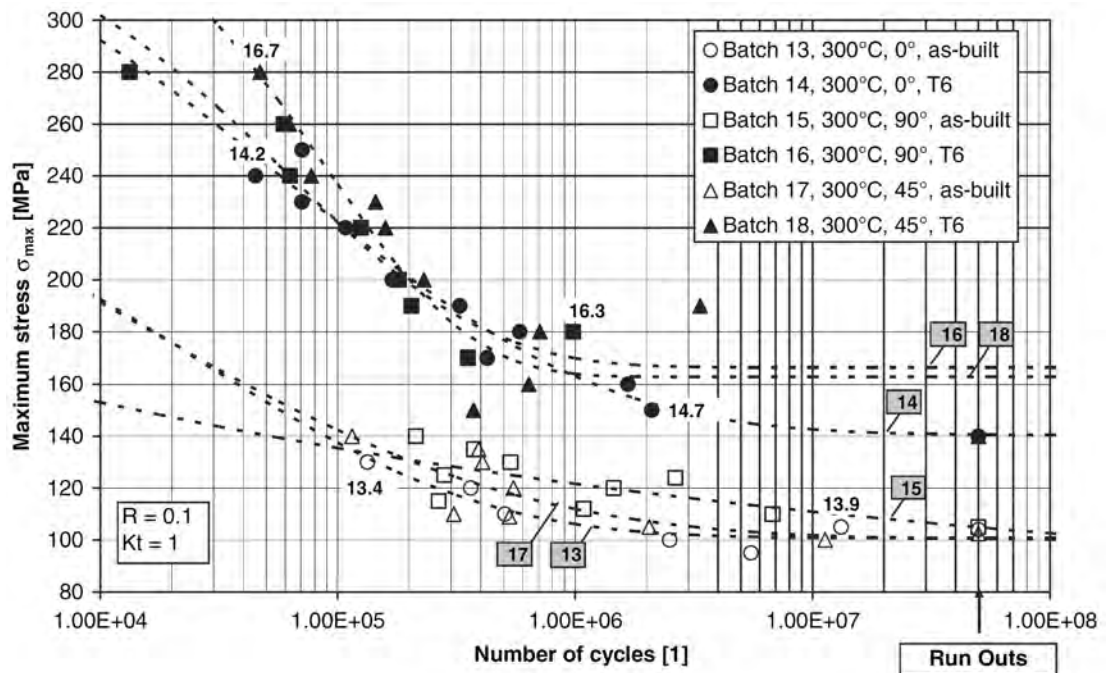


Figure 2.16: Wohler diagrams for AlSi10Mg specimens with and without peak-hardening ([53])

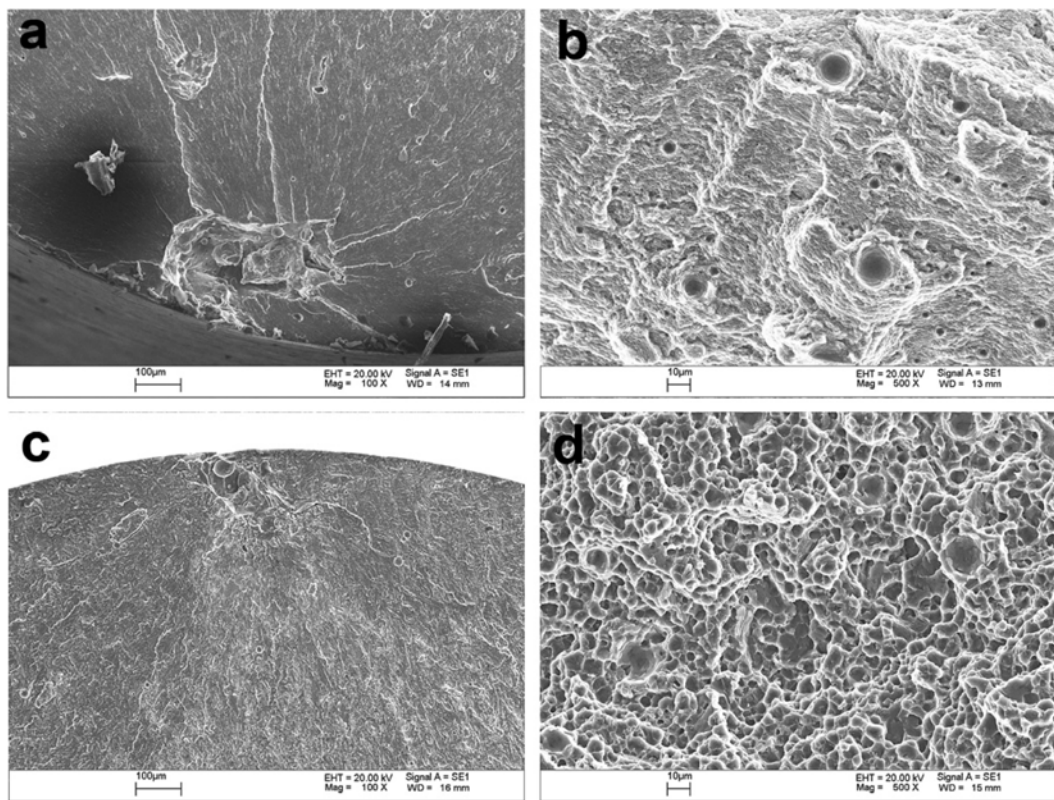


Figure 2.17: Fracture surface of AlSi10Mg specimens: (a,b) as-built condition, faceted fracture (c,d) peak-hardened, dimpled fracture ([53])

how heating helps in reducing residual stresses and bonding defects, effectively increasing the fatigue limit.

Comparable results for stress-relieved, non-peak hardened specimens have been obtained by Mower et al. [4], showing brittle fracture surfaces with a strong predominance of porosity-induced failures, and fatigue limits slightly below those of the wrought material, ranging from 50 to 80 MPa.

### 2.3.4 Crack Growth

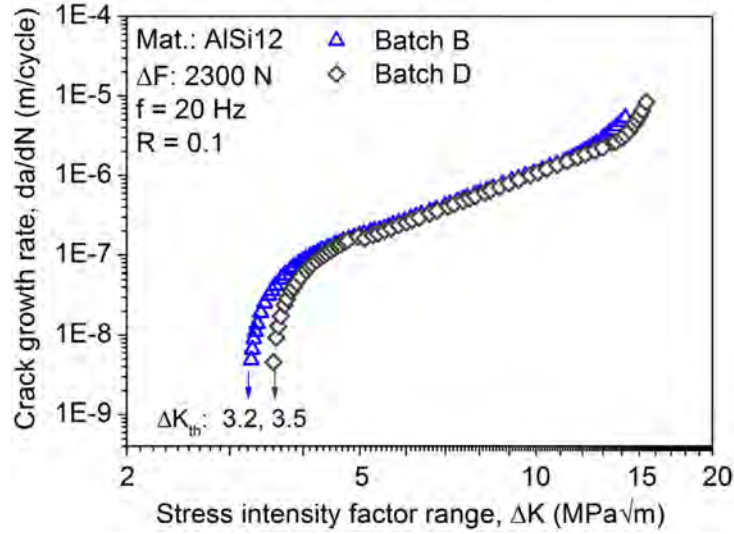


Figure 2.18: Crack growth curves for AlSi12 stress-relieved specimens with (Batch D) and without (Batch B) base-plate heating. (from [11])

Crack propagation behavior in AlSi12 has been studied by Siddique et al. [11], observing the effects of base plate heating on stress-relieved material: coarser grains due to base-plate heating, while providing less resistance to crack initiation, as analyzed in Section 2.3.3, also provide more resistance to crack propagation, as shown in Figure 2.18. Moreover, the authors suggest that, as pores can be considered as initial microcracks, reduction in initial pore size and fraction yields a reduction of the effective stress intensity factor range  $\Delta K$  as per the expression of the cyclic stress intensity factor (Eq. 2.1), resulting a decreased crack-growth as per the Paris-Erdogan equation (Eq. 2.2).

$$\Delta K = Y \Delta \sigma \sqrt{\pi a} \quad (2.1)$$

$$\frac{da}{dN} = C \Delta K^n \quad (2.2)$$

Where  $\Delta \sigma$  is the stress range,  $a$  and  $a_0$  are the instantaneous and initial crack lengths respectively,  $\frac{da}{dN}$  is the crack growth rate and  $A$ ,  $B$ ,  $C$  are fitting parameters. Effects are limited, with little change in threshold values as well as in the Paris-Erdogan region behavior. No analysis of the effects of residual stresses was presented.

Extremely scarce literature is available on AlSi10Mg crack propagation behavior, preventing from any meaningful review to be done.

## 2.4 Discussion

Mechanical properties of AM-SLM parts are highly material and process-dependent, with tensile, fatigue and fracture behaviors all influenced by microstructural defects, which in turn are influenced by selected processes and process parameters.

Tensile properties have been shown to be mainly influenced by microstructural features such as grain size and phase distribution in both Ti6Al4V and Al-alloys. Process parameters should be optimized to retain as fine a structure as possible while not causing excessively brittle behavior. It has been shown for Ti6Al4V that annealing heat treatment is sufficient to noticeably improve elongation-to-failure values, due to the evolution of the  $\beta$ -Ti phase in the microstructure, while residual stresses and porosity have lower effects on tensile properties. HIP process has been shown to lead to the best elongation-to-failure values, as more complete microstructural changes take place, together with the reduction in the size of defects.

Al-alloys show comparable trends: the fine structure resulting from rapid cooling cycles promotes excellent tensile strength values. The associated relatively brittle fracture behavior can be reduced by subsequent heat-treatment of the part: as-built AlSi12 parts have been shown to possess properties comparable with those of cast material, but following HIP it is possible to retain comparable UTS values with doubled elongation-to-failure values. Precipitation-hardening AlSi10Mg alloy has been shown to possess, also in the as-built conditions, properties comparable to the most advanced casting techniques (such as HPDC), albeit internal porosity hindered parts ductility, suggesting that further efforts have to be made in order to increase part density and reduce porosity, while retaining the fine grain size typical of AM process.

Fatigue properties investigation mainly suggests a strong influence of internal porosity: it induces strong stress concentration effects at the pores, facilitating crack propagation and brittle fracture. Ti6Al4V specimens have always shown significant improvements in fatigue life and fatigue strength when HIPed, suggesting that density optimization is of utmost importance to improve fatigue life of SLM parts. Moreover, it was also evidenced that also pore distribution plays a strong role in determining the fatigue life of a component, with pores closer to the surface inducing stronger notch effects.

Similar observations can be made for Al-alloys: reducing internal defects yields improved fatigue lives, with reduced scatter of data obtained through the reduction of possible crack initiation sites. It has also been shown that fine grain sizes prevent crack initiation, thus a microstructure optimization must be performed to have optimal part density while retaining fine-enough grains: while base plate heating yields evident improvements due to a reduction of large internal defects, HIP also yields coarser grains that negatively impact fatigue life. For precipitation alloys, it has been confirmed that peak-hardening treatments can have substantial effects on fatigue life, with SLM peak-hardened specimens outperforming wrought materials.

Crack propagation has been shown to be mainly dependent on residual stresses and

grain shape in Ti6Al4V alloy, as porosity plays a limited role in determining threshold values for crack propagation. For components in the as-built condition, residual stresses would also cause noticeable anisotropy, which is eliminated by heat treating the part.

Although no analysis on the effects of residual stresses for AlSi12 alloy was found, only limited influence of base plate heating was shown, pointing to limited effects of porosity, as for Ti-alloys. Further studies should address both the effect of residual stresses in AlSi12 alloys as well as the entire crack propagation phenomenon in AlSi10Mg alloy.

## 2.5 Conclusions

- SLM-AM parts show comparable, if not superior, mechanical properties with respect to conventional cast parts
- Rapid cooling cycles in AM cause formation of very fine-grained microstructures, yielding high strength.
- Mechanical characteristics are hindered by internal defects and residual stresses due to the rapid cooling.
- Following post-process heat treatments SLM parts show excellent mechanical properties, which, together with the design freedom of AM, suggest that this process is suitable for series production of highly complex and high-performing parts.
- Internal defects, mainly porosity and insufficient bonding, must be addressed by density-optimized processes or by post-process heat treatments.

## Chapter 3

# Experimental Procedures

As the use of aluminum alloys in the field of AM is still relatively unexplored, it was decided to focus the analysis on the static properties of the material, in order to get a complete mechanical characterization and evaluate the feasibility of its use in the automotive industry as a substitute for cast parts.

A parallel work was carried out with the help of *Fiat Chrysler Automobiles* (FCA) EMEA and NAFTA, with specimens being built and tested both in Italy and in North America, in order to verify and compare the material properties with suppliers in different business areas, and to verify the repeatability of the process.

An initial phase of benchmarking between different service providers was followed by a complete characterization of the mechanical properties of the as-built material with one selected supplier. The study was then completed by analyzing the influence of different heat treatments on the material properties.

### 3.1 Manufacturing Process

All the specimens were manufactured using *Direct Metal Laser Sintering* and the ISO AlSi10Mg alloy (equivalent to AA 359.0 in North American notation and to EN AC-43000 according to Euronorm), provided by TLS Technik GmbH in North America and by EOS in Italy, with nominal composition as reported in Table 3.1. Both suppliers used inert gas atomization process to pulverize the aluminum alloy. As discussed in Section 1.4 gas atomization is, among the processes available for the production of AM powders, the most cost-effective for reactive materials such as aluminum, which are easily subject to oxidation and require the use of inert gases as atomizing media.

Table 3.1: Nominal AlSi10Mg powder chemical composition in weight %

	Si	Mg	Fe	Cu	Mn	Zn	Ti	Ni	Al
TLS	9.0–11.0	0.2–0.45	≤ 0.55	≤ 0.05	≤ 0.45	≤ 0.10	≤ 0.15	≤ 0.05	Balance
EOS	9.0–11.0	0.2–0.45	≤ 0.55	≤ 0.05	≤ 0.45	≤ 0.10	≤ 0.15	n/d	Balance

All specimens were built on a EOS M 290 machine. EOS, founded in 1989, is the global leader in DMLS machines, and can provide a complete equipment package to the end user, including the machine, the powder, optimized build parameters and technical assistance. On the North American side it was necessary to resort to an external supplier based in Charlotte (NC), for the manufacturing of the specimens. On the Italian side, the manufacturing was done directly in-house. The main characteristics of the machine are reported in Table 3.2.



*Figure 3.1: EOS M 290 machine (Courtesy of EOS)*

*Table 3.2: Technical data EOS M 290*

Building volume	250x250x325 mm
Laser type	Yb fibre laser; 400 W
Precision optics	F-theta lens; high-speed scanner
Scanning speed	Up to 7.0 m/s
Focus diameter	100 $\mu\text{m}$
Power supply	32A / 400V
Power consumption	max 8.5 kW / average 2.4 kW
Inert gas supply	7000 hPa; 20 m <sup>3</sup> /h

The printing parameters, given in Table 3.3, were suggested by the supplier in North America and could not be modified, whereas in Italy the direct ownership of the machine allowed for a more complete control of the process and the parameters could be modified to verify the effect of two different layer thicknesses (30–60  $\mu\text{m}$ ). It is to be noted that exact values of laser power, scanning speed and hatch were not exactly provided by the supplier to protect their own proprietary parameters, and only the volumetric energy

Table 3.3: Printing parameters EOS M 290

North America		Italy	
Laser power	n/d	Laser power	370 W
Laser scanning speed	n/d	Laser scanning speed	1.3 m/s
Laser hatch angle	n/d	Laser hatch angle	67 deg
Laser hatch	n/d	Laser hatch	0.19 mm
Layer thickness	60 $\mu\text{m}$	Layer thickness	30–60 $\mu\text{m}$
Volumetric Energy Density	29.25 J/mm <sup>3</sup>	Volumetric Energy Density	49.93–24.96 J/mm <sup>3</sup>
Scanning pattern	Raster scan	Scanning pattern	Raster scan
Build plate temperature	165 °C	Build plate temperature	200 °C

density, as defined in Eq. 1.1, was provided.

### 3.2 Specimens

The purpose of this thesis work is the mechanical characterization of SLM-printed AlSi10Mg in terms of static tensile properties. On the North American side the specimens were subdivided into two lots of 18 specimens each, both manufactured with the parameters reported in Table 3.3. The first production lot was subsequently subject to a stress-relieving heat treatment for 2h at 300 °C as recommended by EOS to eliminate residual stresses and generate a microstructure similar to T6 peak hardened AlSi10Mg casting alloy [36]. Each lot contains bars built along the three main directions: 6 specimens along the Z-axis, 6 lying on the XY-plane and 6 in the 45° direction, as in Fig

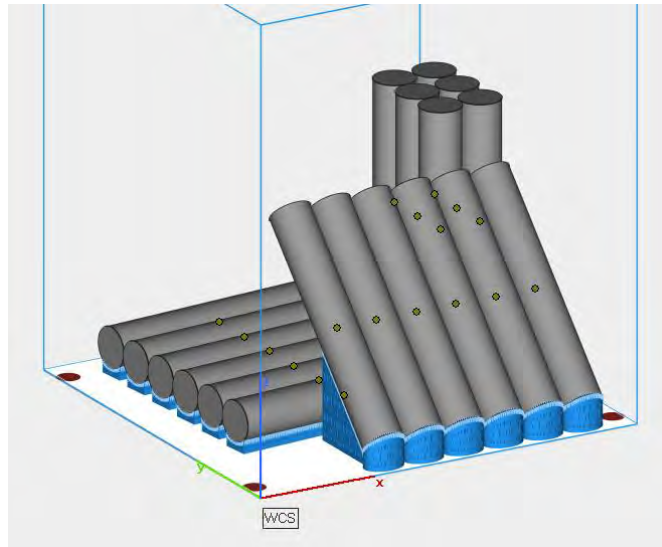


Figure 3.2: North American specimen arrangement in the build chamber

### 3.2.

All specimens were fabricated as cylindrical rods, and then machined to ASTM E8/E8M - 16a #4 specifications as in Fig. 3.3 and Table 3.4 [64]. Each specimen was marked in order to maintain traceability even after machining, as the material removal process eliminates the different appearances from the three different build directions.

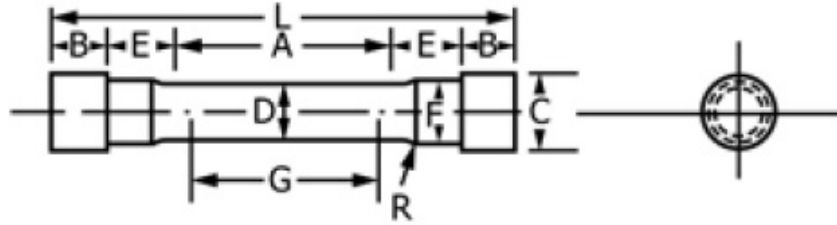


Figure 3.3: ASTM specimens dimensions ([64])

Table 3.4: ASTM specimens specifications

Dimensions [mm]	
<b>For Test Specimens with Gauge Length Four times the Diameter [E8]</b>	
D - Diameter	$12.5 \pm 0.2$
G - Gauge Length	$50 \pm 0.1$
A - Length of reduced parallel section	56
L - Overall length	140 min
B - Length of end section	15 approx.
R - Radius of fillet	10
C - Diameter of end section	22
E - Length of shoulder and fillet section	20
F - Diameter of shoulder	15



(a) As-built cylindrical rods



(b) Evidence of build supports on XY-plane rod

*Figure 3.4: North American as-built rods showing build support marks*

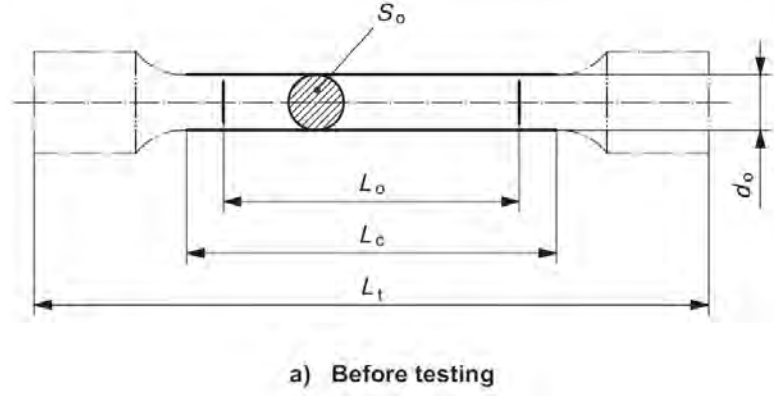


*Figure 3.5: ISO specimens dimensions ([65])*

*Table 3.5: ISO specimens regulated dimensions*

Dimensions [mm]	
<b>For Test Specimens with Proportional Gauge Length</b>	
$d_o$ - Original Diameter	$5 \pm 0.05$
$L_o$ - Gauge Length	25
$L_c$ - Length of Parallel Section	$30 \pm 0.1$
R - Radius of Fillet	10

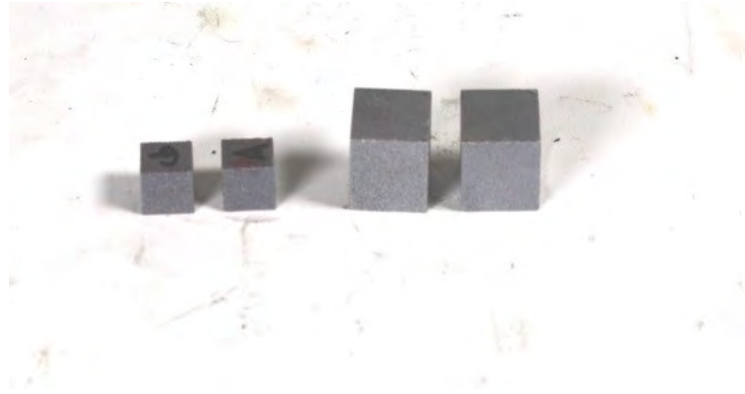
On the Italian side the specimens were subdivided into three lots, manufactured with the parameters reported in Table 3.3, with specimens from the third job having layer thickness of  $60 \mu\text{m}$ . Certain specimens from each lot were subjected to a stress-relieving heat treatment for 2 h at  $300^\circ\text{C}$  as recommended by EOS to eliminate residual stresses and generate a microstructure similar to T6 peak hardened AlSi10Mg casting alloy [36].

All three lots included cubic and parallelepiped specimens, built to be subject to density and hardness tests and optical micrography analysis, as well as cylindrical bars manufactured in the Z-axis and XY-plane, to be machined for tensile testing according to UNI EN ISO 6892-1 (equivalent to ASTM E8 standard) specifications as in Fig 3.5 and Table 3.5 [65]. Proportional specifications were used, with specimens having a gauge length  $L_o$  equal to:

$$L_o = k\sqrt{S_o} \quad (3.1)$$

where  $k$  is a proportionality constant set at 5.65 and  $S_o$  is the original area of the gauge section. It is also mandatory for the parallel section length to be at least equal to:

$$L_c = L_o + (d_o/2) \quad (3.2)$$



(a) Cubic (1x1 cm) and parallelepiped (2.65x1.4 cm) specimens



(b) As-Built cylindrical rods

(c) Machined specimens

*Figure 3.6: Italian cubic and cylindrical specimens (before and after machining)*

### 3.3 Powder Particle Size Distribution

As the powder atomization process yields a range of particle sizes it is important to determine the particle size distribution. Depending on the particle size, different interactions with the recoater and with the laser itself can happen, influencing the final part properties. Literature research [34] shows that it is generally preferable not to have too fine powder particles (preferably  $\geq 10 \mu\text{m}$ ), as it would hinder the flowability of the powder and prevent the machine recoater arm from spreading an even layer of fresh powder.

On the North American side it was possible to obtain a powder certification by the powder provider, containing both the actual chemical composition of the powder batch and the particle size distribution.

On the Italian side it was possible to directly test the supplied powder at the Politecnico di Torino using a Fritsch Analysette 22 NanoTec Laser Particle Sizer. The machine offers a measuring range of  $0.01 - 2000 \mu\text{m}$  by employing a laser measuring system based on the diffraction of a laser beam. A characteristic diffraction pattern, consisting of concentric rings whose intensity and dimension is dependent on the particle size, is generated as the laser beam hits the powder. Larger particles will generate very close rings, while the contrary is valid for smaller particles. Fritsch software, through comparison with a database specific for each material, can determine the size distribution.

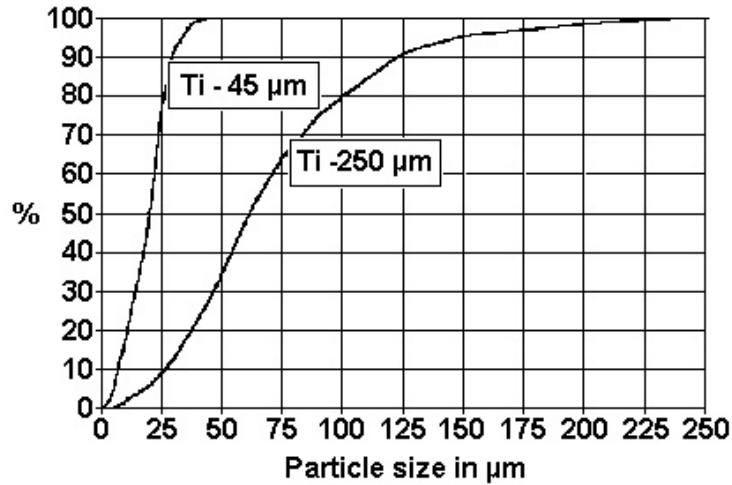


Figure 3.7: Example of powder size distribution chart (courtesy of TLS Technik)



Figure 3.8: Fritsch ANALYSETTE 22 NanoTec laser particle sizer (courtesy of Fritsch)

### 3.4 Tensile Test

A tensile test allows to strain the specimen with an increasing uniaxial stress along the specimen axis. Once a limit value is reached, it will cause failure of the specimen. Generally speaking a number of factors can influence the test results:

- Specimen conditions (surface finish, adherence to dimensional specification)
- Test temperature and humidity
- Strain rate
- Gripping devices
- Load alignment

In North America, to ensure the repeatability of results, tensile tests were conducted according to ASTM E8/E8M - 16a standard, adopting a strain rate of 0.0508

mm/mm/min (i.e. 0.00085 mm/mm/s). The resulting data were the *Yield Strength* (YS), *Ultimate Tensile Strength* (UTS), *% Elongation in 2.0"* ( $\epsilon$ ) and *Elastic Modulus* (E). The machining and the tensile tests were conducted by an external supplier based in Cleveland (OH). Tensile tests were conducted on a Tinius Olsen R60 servohydraulic machine, gripping the specimens so as to ensure uniaxial loading and measuring deformations with an axial extensometer.



Figure 3.9: Tinius Olsen universal testing machine

In Italy tensile test were performed according to the equivalent ISO standard, UNI EN ISO 6892-1 [65] cylindrical cross-section specimens as per the aforementioned standard. The test is strain-controlled but is divided in two parts: in the elastic range of the material a strain rate of 0.00025 mm/mm/s is adopted, while in the plastic range a strain rate of 0.003125 mm/mm/s is to be followed. Tests were performed in Politecnico di Torino as well as in-house using respectively a MTS Criterion Mod. 43 and a Galbadini SUN40.

### 3.5 Density Test

As mentioned in previous chapters, porosity is a known problem with additively manufactured components, and the verification of the part density is necessary to predict the material behavior. Today the main verification methods are provided by Archimedes' principle-based electronic scales or by *Computed Tomography* (CT) scans of sample materials. The first one is able to give an estimation of the % density and porosity, while the second one can give an exact picture not only of the density but also on the shape, size and location of the porosity throughout the bulk of the material.



Figure 3.10: MTS Criterion Model 43 tensile testing machine (courtesy of MTS)

On the North American side it was possible to perform X-Ray CT of selected specimens coming from a different build. Results are not representative of the performances of the alloy-machine combination under study but are just an example of the possibilities offered by CT applied to additively manufactured specimens. X-Ray Computed Tomography is an imaging technique in which multiple X-Ray scans of the specimens are taken from different angles, as the specimen is rotated from 0 to 360°. During this process numerous two-dimensional images representing the attenuation (mostly density-dependent) are obtained by the machine algorithms. Successively, reconstruction algorithms can stack together the 2-D images to create a 3-D model of the specimen, composed of volume elements (*voxels*), which is a high-fidelity representation of the internal density of the specimen under study.

X-Ray Computed Tomography is a completely non-destructive testing technique, which in theory can even be applied to the entire finished part. However, as the resolution of a CT scan is inversely proportional to the specimen size, in order to obtain high-resolution images, with voxels in the order of micrometers, specimens of reduced size (less than 13mm on each side) had to be cut, slicing the test bars significant locations. Vertical and 45° specimens were sliced at the top and at the bottom, to provide a better representation of the evolution of porosity along the build direction, while only one slice was taken from the horizontally-built specimens.

On the Italian side an estimate of the density was obtained on the cubic and parallelepiped specimens. Multiple measurements were performed on a gravimetric scale based on the buoyancy method: the scale is equipped with two plates, as in Fig 3.12: one is immersed in a liquid of known density (usually distilled water) and on it the weight of the immersed specimen is obtained ( $W_{wet}$ ); the second one is not immersed and on it the weight of the specimen in air is obtained ( $W_{air}$ ). Using the Archimedes' principle it is possible to compute the specimen bulk density using in Eq 3.3.

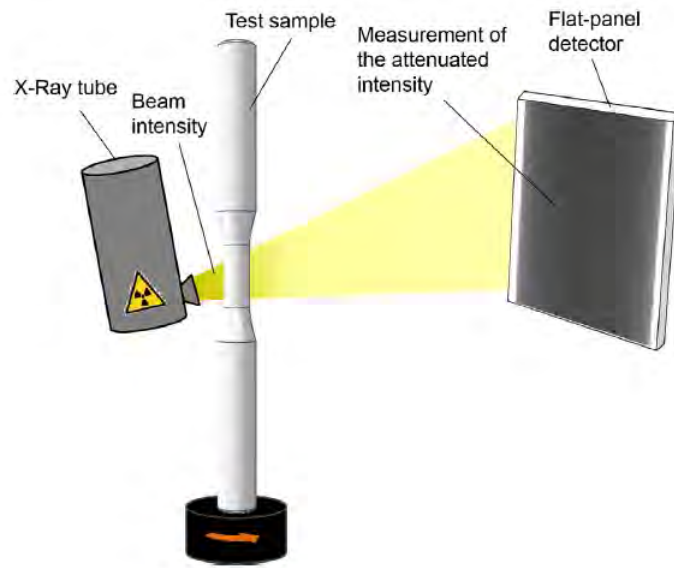


Figure 3.11: X-Ray CT general setup ([10])



Figure 3.12: Example of gravimetric density scale based on Archimedes' Principle (courtesy of Mettler Toledo)

$$\rho = \frac{\rho_{fl} \cdot W_{air}}{W_{dried} - W_{wet}} \quad (3.3)$$

where  $W_{dried}$  is the weight of the dried specimen after wet weighting. By comparing the computed density with the theoretical one it is possible to find the relative % bulk density, and in turn the % porosity as the complementary to 100%.

### 3.6 Chemistry Test

The actual composition of a material is always subject to variability, and to properly assess the elemental composition of the test specimens it was deemed necessary to analyze the chemical composition of the parts.



Figure 3.13: Baird Spectrovac DV-3 setup

On the North American side the standard test method ASTM E1251-11 for Aluminum alloys was adopted [66], on a Baird Spectrovac DV-3 machine: *Spark Atomic Emission Spectrometry* (Spark-AES) is a test method used for the analysis of solid metallic specimens, in which an electric spark is generated in an argon atmosphere between the prepared flat surface of the specimen and an electrode. The spark discharge energy must be sufficient to physically remove material from the material surface, break metallic bonds and cause the dispersed atoms or ions to emit radiation at their characteristic wavelength. The emitted radiation is converted into an electrical signals, from which the chemical composition of the specimen is derived.

The intensity of each electrical signal corresponding to different wavelengths is compared to standard calibration tables for the specific class of alloy under test, and the differential reading is converted into a percentage reading according to ASTM-defined calculations (as per ASTM E158-86 [67]).

No chemistry analysis was performed on the specimens built in Italy.

### 3.7 Hardness Test

Hardness testing provides useful information on the resistance to indentation of a material. It is generally determined by measuring the permanent depth of the indentation when a material is indented using a standard load and indenter. In general hardness testing gives a good measure of the ductility and strength of a given material, while remaining a mostly non-destructive testing technique and thus useful to test even finished parts. Several test methods have been devised, such as Rockwell, Brinell, and Vickers. Each one has different specifications regarding geometry and size of the indenter, load conditions and hardness calculations. On a general basis, in Vickers and Brinell tests the measured hardness is inversely proportional to the footprint left by the indenter on the specimen surface, while in the Rockwell technique hardness is inversely proportional to the penetration depth of the indenter.

On the North American side it was decided to adopt Rockwell hardness testing in order to comply with company database of hardness testing, following the ASTM E18-17e1 standard test method and adopting the HRFW scale, which prescribes a 60 Kgf load with a tungsten 1/16" ball. A Wilson 4JR testing machine was used and three measurements for each specimen were taken in order to compute a meaningful average.

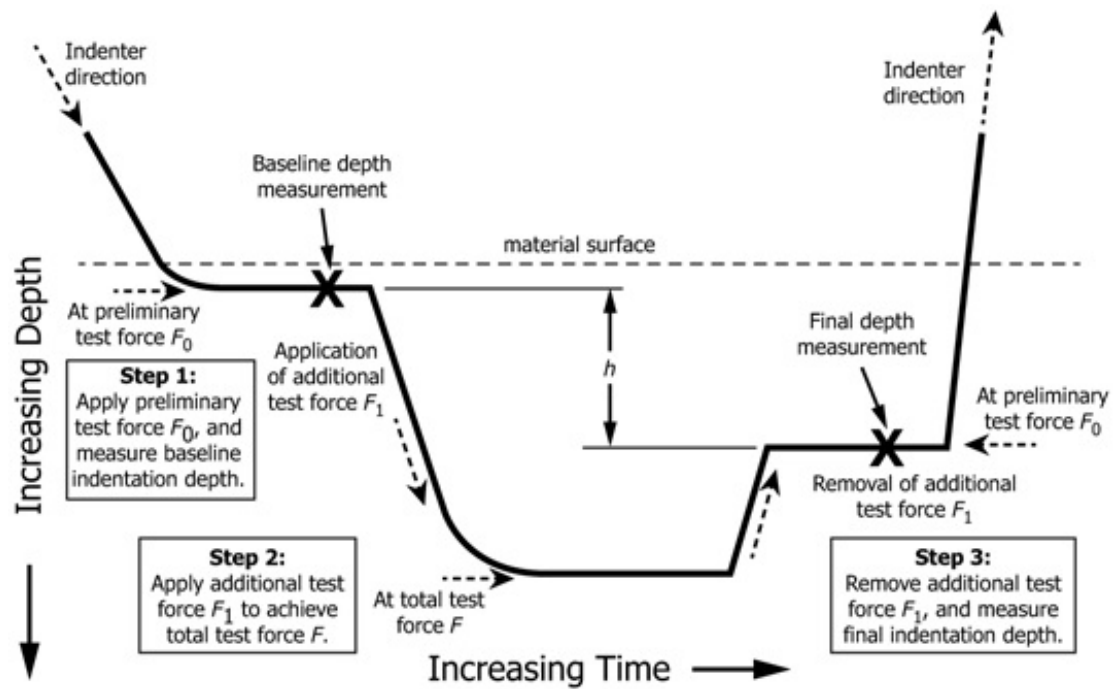


Figure 3.14: Rockwell hardness test method (schematic diagram) ([68])

The test procedure can be summarized in three different phases of force application and removal [68]:

1. Preliminary test force application: The indenter is brought into contact with the specimen and a preliminary force  $F_0$  is applied. After a specified *dwell* time the baseline depth is measured.

2. Additional test force application: The force on the indenter is increased at a controlled rate to achieve the final specified test force  $F$ , which is held for a specified dwell time.
3. Removal of test force and final depth measurement: The force is lowered to the preliminary  $F_0$  value. The final indentation depth is then measured. Rockwell hardness is measured from the difference  $h$  in millimeters between the final indentation depth and the baseline indentation depth.

The Rockwell hardness, for scales using a ball indenter, can be calculated using Eq. 3.4, and results were given as the average of three measurements.

$$HR = 130 - \frac{h}{0.002} \quad (3.4)$$



(a) Wilson 4JR Rockwell hardness testing machine



(b) EMCOTEST M5U 300/030 Brinell hardness testing machine

*Figure 3.15: Hardness testing machines at the North American supplier (a) and in Italy (b)*

On the Italian side hardness was evaluated on the cubic and the parallelepiped specimens adopting Brinell hardness tests as per UNI EN ISO 6506-1 standard [69] on an EMCOTEST M5U 300/030 machine. The test involves the use of a 2.5mm spherical indenter, made of tungsten carbide, and of a 10 N load, maintained for 10 s. The tests were carried out on both parallel and perpendicular faces of the specimens (with reference to the build direction of the specimens), and measurements were taken on 3 points per face, to create a meaningful average.

The actual hardness calculation is carried out by measuring the mean diameter of the indentation as in Eq 3.5, where  $d_1$  and  $d_2$  are the indentation diameter measured at 90 deg. It is thus possible to compute the Brinell hardness using Eq 3.6, where  $F$  is the

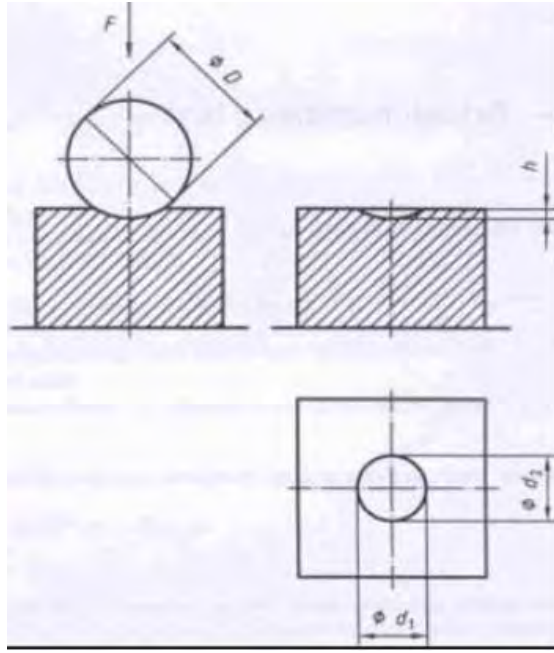


Figure 3.16: Brinell hardness test measurement principle ([69])

applied force in N and  $D$  is the sphere diameter in mm [69].

$$d = \frac{d_1 - d_2}{2} \quad (3.5)$$

$$HB = \frac{2F}{\pi D \cdot (D - \sqrt{D^2 - d^2})} \quad (3.6)$$

### 3.8 Optical Microscopy

After the previous analyses were completed, optical microscopy was used to obtain the metallography of the material in different build conditions. Mechanical properties of a metallic material are influenced not only by the different phases of an alloy, but also by their distribution and by the grain structure. It is therefore important to clearly evidence the relations between different metallic structures and the material properties. The metallographic study is carried out with the help of an optical microscope, using specimens treated with special etching agents which highlight the different phases and the grain structure.

To analyze the specimens it is at first necessary to cut small specimens from the metallic specimen, ensuring that during the cutting operation sufficient lubrication is provided between the cutter and the piece, to avoid excessive heating of the material and possible microstructural modifications. To proceed with the analysis it is necessary to prepare the specimens by mounting them in a structure suitable for handling and long-term storage such as an epoxy resin, and then it is necessary to polish and etch the surface to be observed.

The cutting operation is completed with a circular saw, rotating at high speed but fixed in space. The piece is held in place by a system of grips designed to avoid any

vibration which could compromise the operation. The piece is then motioned towards the saw at a controlled speed. It is important to avoid excessive speeds which would cause an excessive heating of the material and would cause a modification of the microstructure. The machine is also equipped with a lubrication system designed to reduce friction between the cutting tool and the workpiece.

The cut specimens were then cold-mounted in an epoxy resin, to facilitate handling and provide a durable storage medium. The mounting was done by placing the specimen inside a cylindrical container, with the surface to be analyzed facing downwards. The container was then filled up with an equal mix of epoxy resin and curing agent.

After they were cured, specimens were polished using progressively finer sandpaper and water lubrication and finally a diamond suspension to obtain an optimal surface finish. A final etching to highlight grain structure and morphology was made with hydrofluoric acid in North America (0.5%  $HF$ , 99.5% water), while in Italy the specimens were etched with the Keller's reagent (1.0%  $HF$ , 1.5%  $HCl$ , 2.5%  $HNO_3$  and 95% water), both of which are recommended etchants for aluminum [70].

### 3.9 Scanning Electron Microscopy

The fracture surfaces of the tensile specimens were observed under the *Scanning Electron Microscope* (SEM), which provides high-resolution images that are extremely useful to understand the fracture mechanisms.

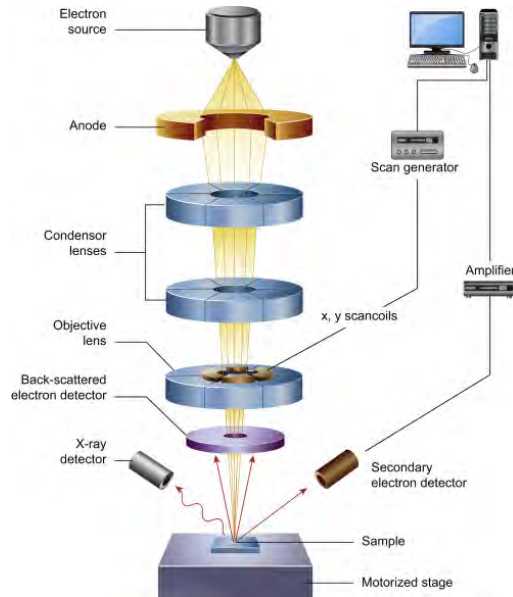
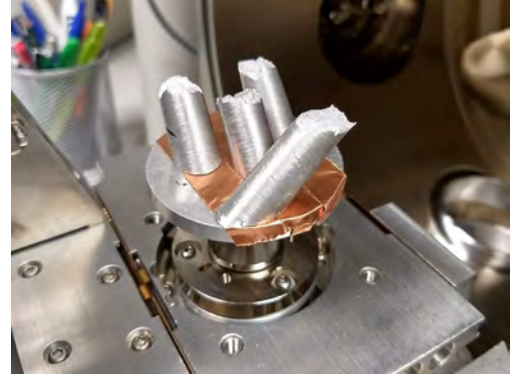


Figure 3.17: Schematics of a SEM (courtesy of [71])

As shown in Fig 3.17, a *Scanning Electron Microscope* operates based on the interaction between a focused electron beam and the specimen surface. The electron beam is generated by the thermoionic emission from a Tungsten or LaB6 cathode inside an electron *gun*. The electrons are then accelerated by the voltage difference between the cathode and the anode, in the order of 5 - 30kV. The electron beam is then focused



(a) SEM machine with post processing hardware



(b) Sample setup

*Figure 3.18: Setup of the SEM used at the University of Windsor*

and properly deflected by a system of electromagnetic lenses and it finally impacts the specimen, causing the emission of a number of different radiations, of which X-Ray and secondary electron emission are the most interesting. By capturing the first one it is possible to conduct microstructural analysis of the specimen and determine its chemical composition, whereas the latter gives the actual scan of the specimen surface morphology.

The SEM requires conductive specimens to be used, in order to allow for the conduction of the excess electrons received, and it also requires high vacuum conditions, in the order of  $10^{-4}$  Pa, to maintain proper operating conditions of the electron beam. The electron beam is not stationary in space but is scanned in a raster pattern on the specimen, by deflecting it with a magnetic lens. The secondary electron emission is captured by a proper detector, which converts the radiation in an electric signal to be amplified. This signal is interpreted as an intensity distribution that can be displayed as a black and white digital image of the specimen surface [72].

It was possible to capture SEM imagery both in at the University of Windsor, as well as in Italy using in-house laboratories. The specimens did not have to be prepared as aluminum is a conductive material, and image post-processing was performed directly on the SEM.

## Chapter 4

# Experimental Results

The main results of this research work are presented in this chapter. The powders used to manufacture the specimens are characterized and then an initial characterization of the AlSi10Mg alloy in use is given in terms of chemical composition, microstructure and material properties such as bulk density and hardness. The tensile properties of the material are then presented along with the SEM characterization of the fracture surface.

### 4.1 Powder Characterization

In any powder-based additive manufacturing process the raw powder properties, in terms of its chemistry, particle shape, particle size distribution and its flowability play a fundamental role in determining the final part properties. No chemical change occurs during the atomization process, and the maximum flowability should be achieved in order to improve the powder deposition process in the build chamber and avoid process-induced defects inside the structure.

#### 4.1.1 North American Experimental Results

The powder used in the production of the specimens in North America was provided by TLS Technik, who also provided a powder characterization study to certify the quality of their product. The certification is focused on establishing the particle diameter size distribution and assessing the real powder chemistry.

*Table 4.1: Nominal vs. actual TLS-supplied AlSi10Mg powder chemical composition in weight %*

	Si	Mg	Fe	Cu	Mn	Zn	Ti	Ni	Al
Nominal	9.0	0.2	–	–	–	–	–	–	–
	–	–	≤ 0.55	≤ 0.05	≤ 0.45	≤ 0.10	≤ 0.15	≤ 0.05	Bal.
Actual	10.250	0.391	0.144	0.04	0.003	≤ 0.002	0.016	0.006	Bal.

The chemistry test of the powder certifies that the powder is well within the nominal

values expected for the AlSi10Mg alloy. No contamination occurred during the gas atomization process and thus the powder can be expected not to induce any lack-of-fusion phenomena due to oxidation problems.

The particle size distribution is reported in Fig 4.1. The shape of the distribution clearly does not fit a normal distribution, showing instead a marked asymmetrical shape. The size distribution is centered towards the higher end of the size spectrum, with an average particle diameter of around 45  $\mu\text{m}$  and the distribution itself is quite narrow, with most particles ranging from 20 to 60  $\mu\text{m}$ . The large amount of bigger particles can be used to predict a good flowability for the powder, as smaller-sized particles tend to cling to each other. In fact, when the number of finer particles increases, the Van Der Waals attraction forces between particles become non-negligible and tend to be comparable with the gravitational force, creating a non-flowing conglomerate of powder. When coarser particles are present the particles do not cling together and, as long as they are of spherical shape (as ia expected from the gas atomization process) they flow much easier better.

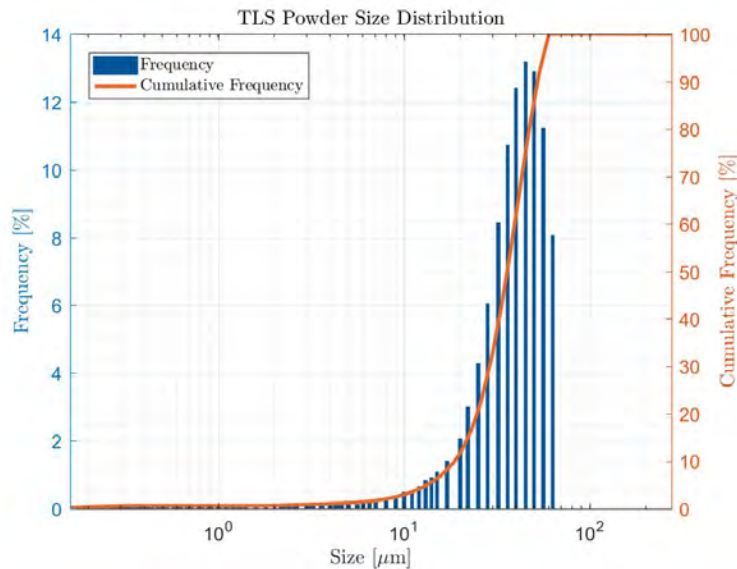


Figure 4.1: Particle size distribution for TLS AlSi10Mg powder

The cumulative size distribution is also shown in Fig 4.1, and is summarized in Table 4.2 with the D10, D50 and D90 values, corresponding to 10%, 50% and 90% of the cumulative distribution, meaning that the stated percentage of powder particles has a lower size than the one indicated.

Table 4.2: TLS powder particle cumulative size distribution percentiles

	D10	D50	D90
Diameter ( $\mu\text{m}$ )	20.29	38.15	55.04

### 4.1.2 Italian Experimental Results

The powder used for the specimens built in Italy was supplied directly from the machine manufacturer, EOS. The characterization was carried out in-house and at the Politecnico di Torino laboratories. The main focus was on establishing the powder morphology through SEM observations, and assessing the particle diameter size distribution.

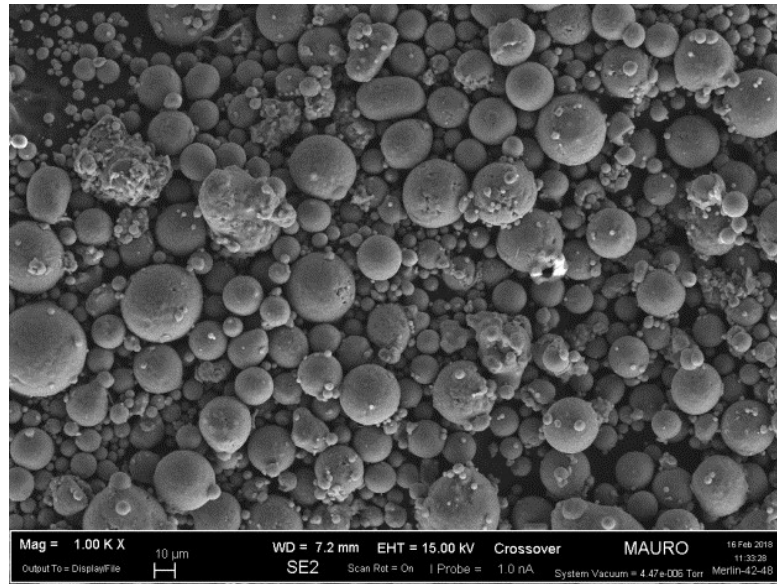


Figure 4.2: EOS-supplied powder morphology at 1000x magnification

Fig 4.2 shows the powder morphology as observed through the SEM. The particles, as characteristic of gas-atomized powders, present a generally spherical shape that closely resembles the one found in literature surveys (see Fig 1.14), although with a noticeable presence of satellites attached to the main particles. Spherical particle shapes are recommended to improve the flowability of the powder and improve the homogeneity of the fresh powder layer during the re-coating process.

The particle size distribution, together with the cumulative size distribution, is reported in Fig 4.3. The distribution of the particle sizes approximates a Gaussian curve, with an average particle size of around 27  $\mu\text{m}$ . The distribution is not as narrow as in the TLS-supplied powder, with most particles ranging from 10 to 60  $\mu\text{m}$ . The lower amount of bigger particles certainly indicated lower flowability with respect to the powder used in North America, as the particles will have an increased tendency to cling to each other and create agglomerates.

The cumulative size distribution is summarized in Table with the D10, D50 and D90 values.

Table 4.3: EOS powder particle cumulative size distribution percentiles

	D10	D50	D90
Diameter ( $\mu\text{m}$ )	19.30	40.70	74.80

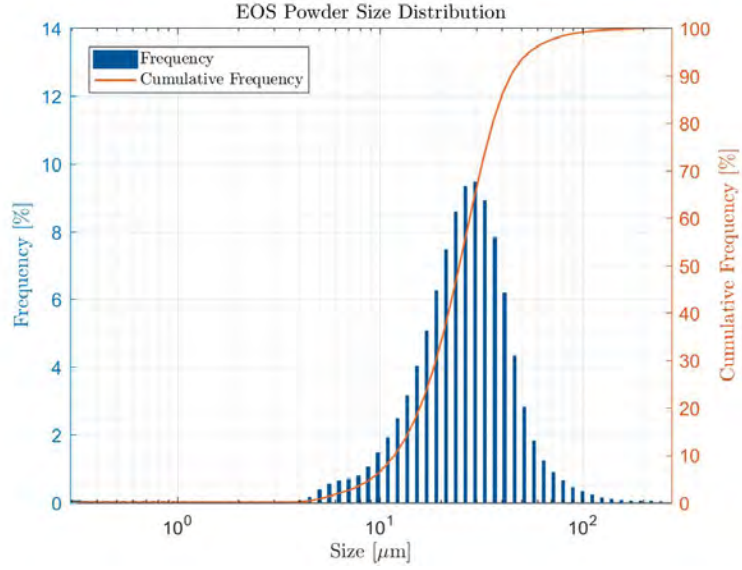


Figure 4.3: Particle size distribution for EOS AlSi10Mg powder

Table 4.4: Average weight % chemical composition of Batch 1 (stress-relieved specimens)

	Si	Mg	Fe	Cu	Mn	Zn	Ti	Al
Powder	10.250	0.391	0.144	0.04	0.003	≤ 0.002	0.016	Bal.
Part	9.557	0.447	0.187	0.025	0.003	0.010	0.018	Bal.
Variation (%)	-6.764	14.237	29.630	-36.667	0.000	383.333	10.417	n/d

## 4.2 Chemistry

Initially it was important to characterize the chemical composition of the specimens, to ensure that no contamination of the powder was present and the results are actually representative of the properties of the AlSi10Mg alloy.

### 4.2.1 North American Experimental Results

The batches manufactured in North America were tested with *Spark Atomic Emission Spectrometry* (Spark-AES) after the build to verify that the material chemistry was maintained throughout the build. The results of the analysis, compared to the initial composition of the raw material, are presented in Table 4.4.

The chemical composition is consistent with the one of the starting AlSi10Mg alloy powder, thus results are representative of the alloy's properties, although a consistent evaporation of silicon and copper can be observed, which causes an increase in the weight % of other alloying elements, in particular Magnesium and Iron.

The chemical composition of Batch 2 is consistent with the starting powder, and in this case a lower decrease of the silicon content can be noticed. Moreover, the magnesium

Table 4.5: Average weight % chemical composition of Batch 2 (as-built specimens)

	Si	Mg	Fe	Cu	Mn	Zn	Ti	Al
Powder	10.250	0.391	0.144	0.04	0.003	$\leq 0.002$	0.016	Bal.
Part	10.144	0.376	0.130	0.009	0.003	0.008	0.007	Bal.
Variation (%)	-1.034	-3.836	-9.722	-76.500	0.000	290.000	-56.250	n/d

and iron contents decrease instead of increasing with respect to those of the raw powder. The difference can be induced by the fact that the thermal heat treatment undergone by Batch 1 may cause precipitation of silicon particles inside the structure, thus reducing the amount of silicon dissolved in the microstructure.

#### 4.2.2 Italian Experimental Results

The batches manufactured in Italy were built using an EOS-supplied powder with nominal chemical composition as in Table 4.6.

Table 4.6: Nominal AlSi10Mg EOS powder chemical composition in weight %

Si	Mg	Fe	Cu	Mn	Zn	Ti	Sn	Pb	Al
9.0–11.0	0.2–0.45	$\leq 0.55$	$\leq 0.05$	$\leq 0.45$	$\leq 0.10$	$\leq 0.15$	$\leq 0.05$	$\leq 0.05$	Bal.

### 4.3 Microstructure

Microstructural analysis allows to compare the different production lots, and analyze the effect of the layer-by-layer deposition as well as the effect of heat treatments. Both in North America and in Italy it was generally possible to observe the microstructure characteristic of additively manufactured components: very fine grains and evident laser tracks, together with the presence of non-negligible porosity.

#### 4.3.1 North American Experimental Results

Optical microscopy observations were made on both batches. Fig 4.4 shows the micrographs from Batch 2 in all building directions. For specimens built along the Z-axis images were taken at the top and at the bottom to highlight possible microstructural differences.

Laser tracks are visible in all the directions and highlight the scanning pattern of the part, with the overlapping laser tracks. On the Z-axis it is possible to observe the hatch angle between two successive layers, due to the different direction of the laser tracks, while on the XY specimens it is possible to visualize the effect of directional cooling,

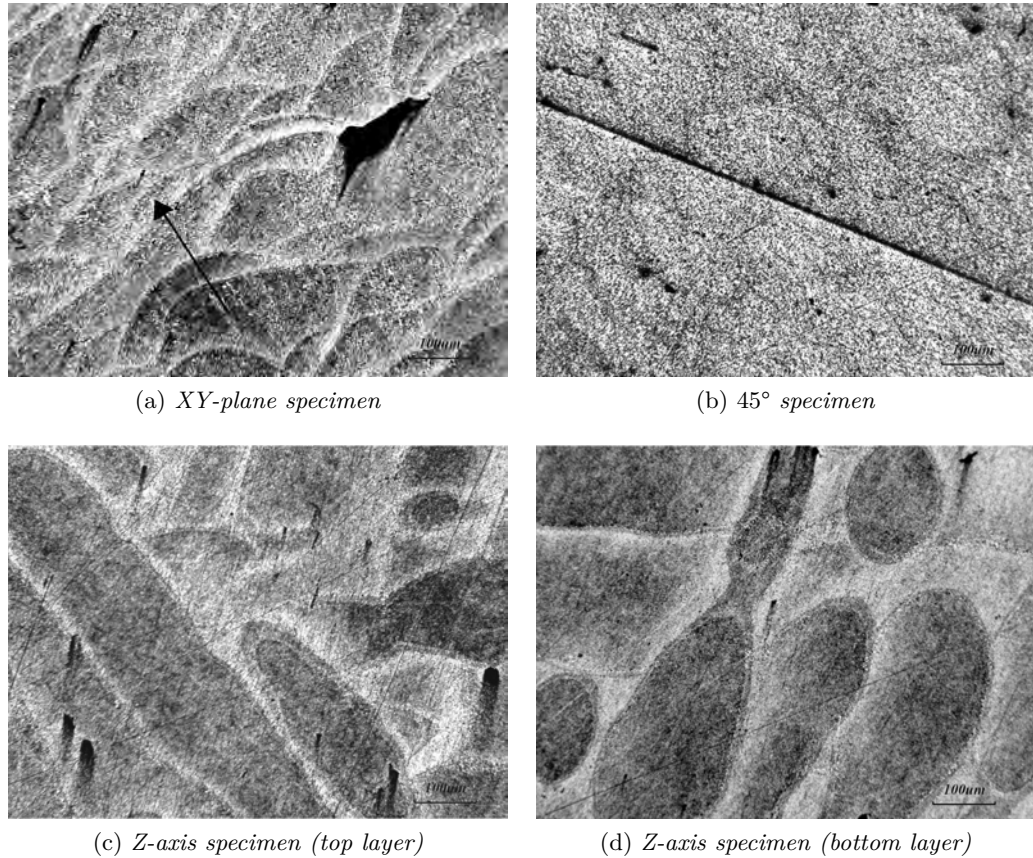


Figure 4.4: Microstructure of as-built specimens from Batch 2 at 100x magnification

with the melt pools having an elongated circular shape according to the thermal gradient inside the build.

The microstructure of all the specimens is fairly inhomogeneous, with evident segregation of silicon particles at the melt pool boundaries, where solidification is faster and segregation more likely to happen. It is possible to observe porosity evenly distributed throughout the structure, with some gaps being particularly big and not round shaped, creating important stress concentrations.

Fig 4.5 shows the micrographs of stress-relieved specimens from Batch 1 in all three directions. For the specimens grown in the Z-axis two longitudinal and transversal micrographs were taken with respect to the build direction in order to highlight possible microstructural differences.

The stress-relieving heat treatment has a noticeable effect, as now all the three different directions present a similar microstructure, without noticeable differences even between the longitudinal and the transversal direction. A very finely-grained structure is retained even after the heat treatment, but the silicon now appears to be evenly distributed in the structure. No significant grain boundaries can be observed, and no laser tracks are visible in the structure, which gives the appearance of an isotropic microstructure.

It is however possible to notice porosity (black areas) in all the specimens. Most of the porosity can be found to be highly aligned along straight lines, pointing at the

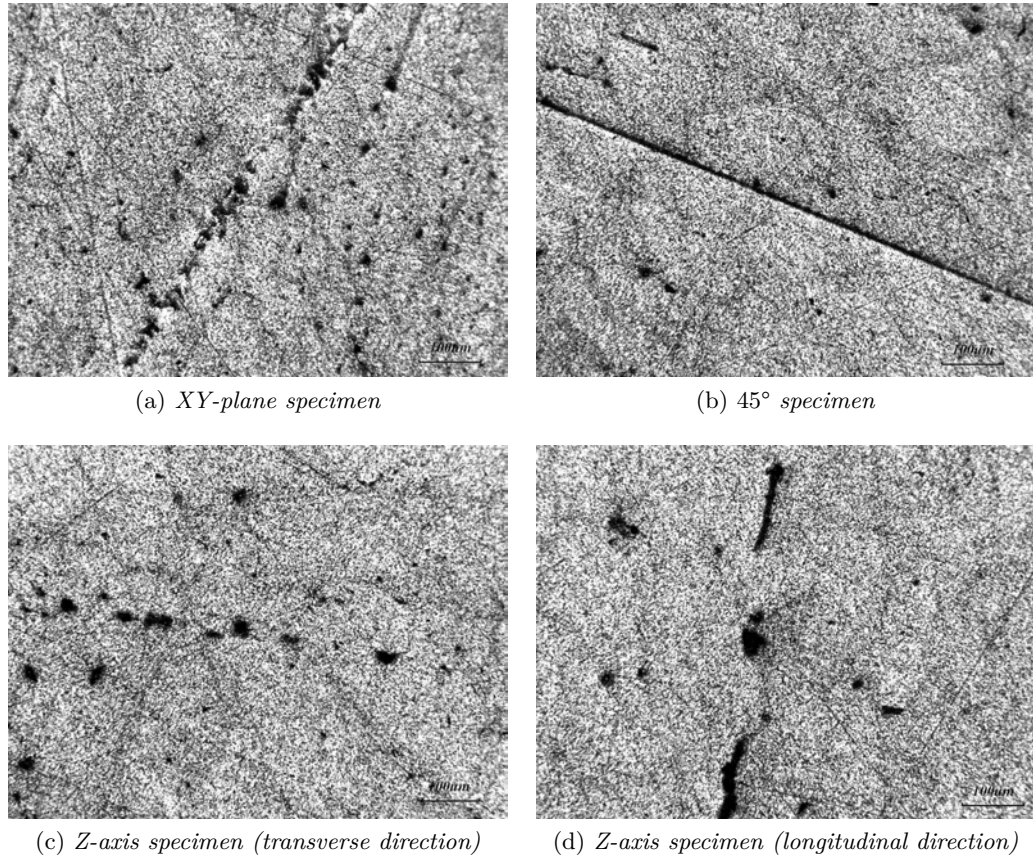


*Figure 4.5: Microstructure of stress-relieved specimens from Batch 1 at 100x magnification*

possibility of it being due to process-induced lack of fusion between successive layers. It is possible to notice this alignment of the porosity especially in the XY-plane specimen and in the longitudinal Z-axis (Fig 4.5 (a),(d)), with evident lack-of-fusion areas in the Z-axis specimen, measuring more than 100  $\mu\text{m}$  in length. The evident straight line in the 45° specimen was determined to be a scratch induced by an incorrect polishing.

### **4.3.2 Italian Experimental Results**

Multiple micrographs were taken for all three production lots, in both the as-built and heat-treated conditions, and the microstructure was found to be consistent between the three production lots. Fig 4.6 shows low-magnification micrographs of as-built and heat-treated specimens from the Batch A, in both the perpendicular and parallel direction with respect to the Z-axis. The images highlight the laser tracks resulting from the raster scanning pattern and the hatch angle between the various layers, and on the perpendicular section it is possible to appreciate the multi-layer melting effect induced by the laser beam, with the melt pools overlapping between various layers.

As in the case of the specimens produced in North America, it is possible to see evidence of some porosity within the material structure (visible as black areas), which however is of much smaller dimensions (less than 10  $\mu\text{m}$  than in the American specimens

of Batch 1, and is always circular-shaped, resulting in lower stress concentrations than the elongated ones of Fig 4.5. It is possible to notice that porosity is more concentrated at the melt pool boundaries, pointing to possible lack of consolidation during the solidification of the material. By observing sections of the specimen surface at higher magnification it is possible to proceed to a more detailed analysis of the material structure.

In Fig 4.7 (a) it can be seen how the laser tracks are aligned to each other and that each layer is rotated with respect to the previous one by the hatch angle (defined in Section 3.1, Table 3.3), resulting in constant and controlled superposition of the layers to improve the consolidation of the material. In Fig 4.7 (b) it is possible to see evidence of the directional heat conduction along the build direction, resulting in elongated shape of the melt pools according to the thermal gradient. It is also possible to observe a segregation of Si-particles at the grain boundaries, as a result of the very quick solidification process. By increasing the magnification (500x - Fig 4.8) it is possible notice the directional growth of the grains, parallel to local heat transfer, particularly at the edges of the melt pools.

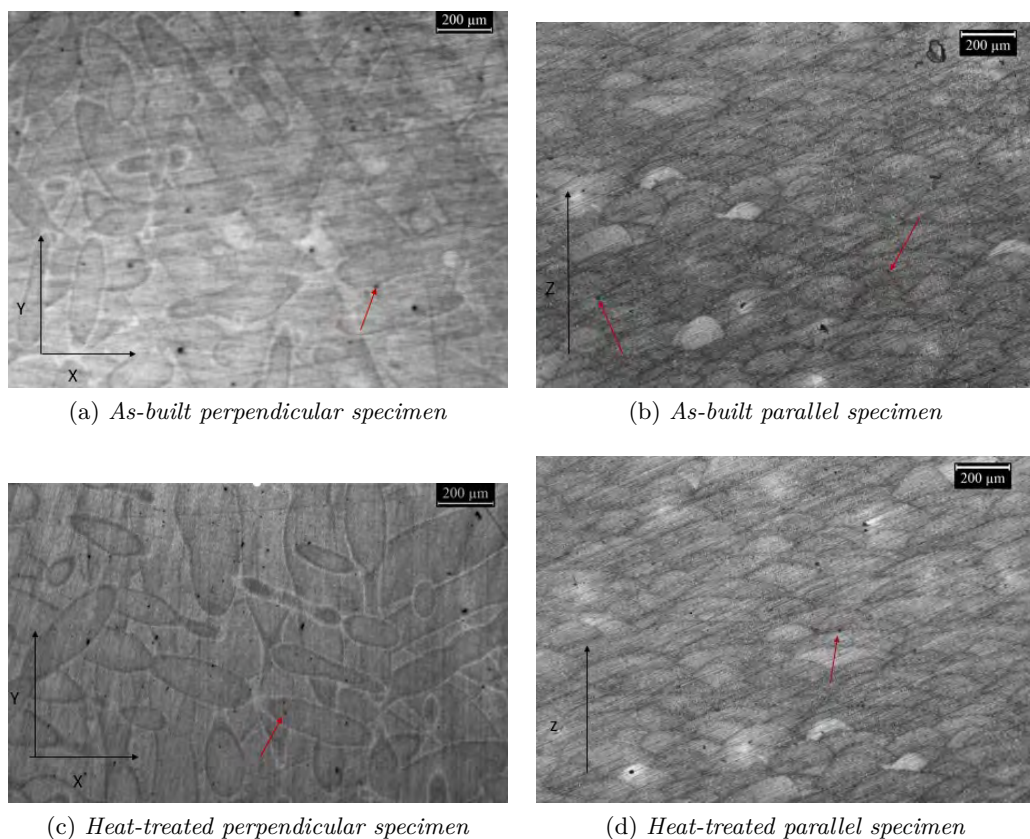


Figure 4.6: Microstructure of specimens from Batch A at 50x magnification

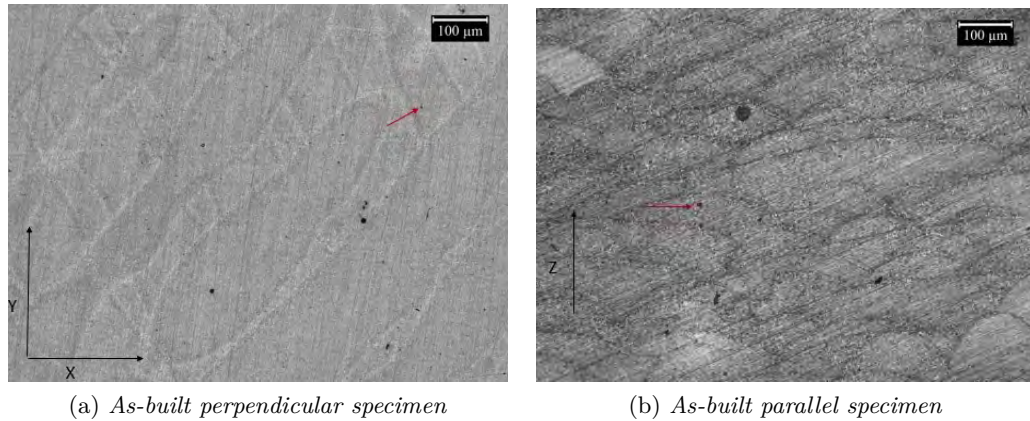


Figure 4.7: Microstructure of specimens from Batch A at 100x magnification

## 4.4 Density

Density measurements give a good understanding of the process capability to produce fully dense parts, suitable for functional usage. Changes in density between the different production lots and the effect of the different production parameters were also investigated.

### 4.4.1 North American Experimental Results

No density measurements could be taken of North American specimens as the necessary equipment was not available.

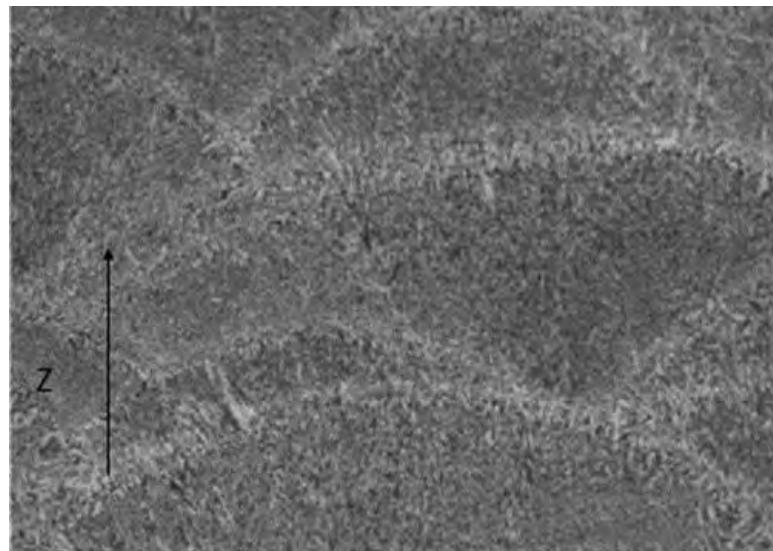


Figure 4.8: Microstructure of a specimen from Batch A at 500x magnification, parallel section

#### 4.4.2 Italian Experimental Results

Table 4.7 reports the density measurements carried out in Italy for the parallelepiped specimens, grown along the Z-axis. As-built and stress-relieved states are indicated as *As-B* and *S-R* respectively. In addition to experimental figures also theoretical values, resulting from the EOS datasheet, are reported to give a comparison of the actual process performance with respect to the manufacturer’s indications [36].

Table 4.7: Bulk density and porosity measurements of parallelepiped specimens

	Batch A		Batch B		Batch C	
	As-B	S-R	As-B	S-R	As-B	S-R
Bulk Density ( $g/cm^3$ )	2.63	2.63	2.63	2.63	2.63	2.61
EOS Datasheet Density ( $g/cm^3$ )	2.67					
Relative Bulk Density (%)	98.37	98.29	98.37	98.28	98.24	97.92
Porosity (%)	1.63	1.71	1.63	1.72	1.76	2.10
EOS Datasheet Porosity (%)	0.998					

In all the three production lots, and in all processing conditions, it is possible to highlight porosity values that are greater than the theoretical figure supplied by EOS. Porosity is also consistent between the different production batches at equal layer thickness (Batch A and B), while it is possible to observe a slight increase in porosity in the third Batch grown at double layer thickness (Batch C). A minimal increase in porosity following stress relieving heat treatment could also be noticed within all production batches.

It is therefore possible to infer that porosity can be influenced both by process parameters, such as layer thickness, as well as post-process treatments, such as stress-relieving. It is conceivable that the increased layer thickness may lead to a slight increase of lack-of-fusion zones, as the energy density provided to the material is lowered by increasing the processed material thickness. On the other hand the post-process stress relieving can induce softening of the material: the entrapped gas in the pores would naturally tend to expand at higher temperatures, and the material softening eases the process, resulting in an increase of the void fraction.

#### 4.5 Hardness

Material hardness is a mechanical property which is highly dependent on the material microstructure, and can give important information on the effect of process parameters or post-process heat treatments on the material. Although different hardness measurement scales have been used, it is possible to compare the results with the help of

conversion tables provided by the supplier and developed starting from ASTM standards [73].

#### 4.5.1 North American Experimental Results

Hardness was measured for each specimen build direction in both batches, and results were given as an average of the measurements to represent the average material hardness. Conversions were done according to the conversion charts provided by the supplier [74], developed following ASTM standards [68][73].

Table 4.8: Rockwell and Brinell hardness results for Batch 1 & 2

Hardness	Batch 1		Batch 2	
	HRFW (Avg)	HBW (Avg)	HRFW (Avg)	HBW (Avg)
XY	75.00	69	66.50	60
45° - Top	75.00	69	70.00	63
45° - Bot.	75.00	69	66.00	59
Z - Top	75.00	69	70.50	64
Z - Bot.	75.00	69	65.50	59
EOS Datasheet Hardness	119±5 HBW			

It is possible to evidence a high repeatability of results between the various build directions, with all the specimens from Batch 1 presenting the same average hardness. On the contrary specimens from Batch 2 highlight a substantial difference in hardness between the various areas of the build. The bottom of a part was found to be consistently softer than the top layers. This phenomenon can be linked to the fact that the bottom of the specimen has to remain at high temperatures for a much longer period of time, giving rise to a coarsening of the structure and to a decrease in hardness, while the top layers retain the fine structure caused by the high cooling rates associated with SLM.

The differences between the two batches are linked to the effect of the stress-relieving heat treatment: the high temperatures give rise to a microstructural homogenization, as seen in Section 4.3.1, which explains the similar results in all of the different locations. The greater levels of hardness recorded in stress-relieved specimens may be due to fact that, in addition to the removal of anisotropy, stress relieving may also cause the precipitation of silicon and Mg<sub>2</sub>Si particles, which are responsible for the hardness increase (AlSi10Mg being a *precipitation hardening* alloy).

#### 4.5.2 Italian Experimental Results

In Italy it was also possible to separately test as-built and stress-relieved parallelepiped specimens and to repeat measurements on both parallel and perpendicular faces with

respect to the build direction (Z-axis). Table 4.9 summarizes the results obtained for all three batches.

Table 4.9: Brinell hardness results for batches A, B & C

	Batch A		Batch B		Batch C	
HBW (Avg)	As-B	S-R	As-B	S-R	As-B	S-R
Face Perpendicular to Build Direction	103.30±2	109.30±1	105.53±1	109.43±2	109.61±1	109.43±1
Face Parallel to Build Direction	81.66±6	82.6±1	88.80±1	89.86±2	91.00±1	92.73±3
EOS Datasheet Hardness	119±5					

For Italian batches it was possible to achieve good levels of hardness, comparable with *High Pressure Die Casting* (HPDC) results. The high cooling rates typical of the SLM process yield a finely grained structure, which can be expected to show good hardness levels already in the as-build state. It is also possible to observe a small yet repeatable increase in material hardness after stress relieving. The hardness increase can be linked to the precipitation hardening effect introduced by the heat treatment, causing precipitation of Mg<sub>2</sub>Si particles within the material structure.

Moreover, it is possible to notice a significant difference in results from the parallel or perpendicular direction with respect to the build direction. Values from the parallel face refer to material layers that have remained at elevated temperature for a long time causing a grain coarsening, while the perpendicular face is the top layer, which has solidified last and remained at high temperature for a shorter amount of time, leading to a finer microstructure and higher hardness values.

The difference in results between specimens manufactured in North America and in Italy can mostly be linked to different process parameters yielding different material microstructures: the build plate temperature, as well as the volumetric energy density values, are different, causing a great variation in thermal gradients inside the build chamber and resulting in highly different material microstructures, as discussed in Section 4.3. This difference in results highlights the profound effect on material properties of both process parameters (influencing the solidification conditions) and of post-process heat treatment parameters, which can induce significant modifications to the mechanical properties.

## 4.6 Tensile Properties

The mechanical properties obtained from the tensile test consist of the Elastic Modulus ( $E$ ), Yield Strength ( $YS$ ), Fracture Strain ( $\epsilon$ ) and Ultimate Tensile Strength ( $UTS$ ). Results from all the batches and all the directions were collected to evaluate in detail the

mechanical properties of the material and how they are affected by process parameters, build orientation and post-process heat treatment.

#### 4.6.1 North American Experimental Results

Tables 4.10 and 4.11 report results for the North American as-built and stress-relieved material, together with target values provided by EOS for stress-relieved material, while Fig 4.9 gives an example of the raw tensile test data from the Z-axis specimens of Batch 1.

Table 4.10: Tensile test results for Batch 1 (stress-relieved)

	XY Specimens	45° Specimens	Z Specimens
$UTS$ [MPa]	269.5±1.4	266.3±1.0	270.1±1.7
EOS $UTS$ [MPa]	345±10	/	350±10
$YS$ [MPa]	169.8±1.6	173.5±1.9	173.1±3.9
EOS $YS$ [MPa]	230±15	/	230±15
$E$ [GPa]	74.2±2.6	75.4±5.8	75.3±2.0
EOS $E$ [GPa]	70±10	/	60±10
$\epsilon$ [%]	11.34±0.34	12.62±0.67	8.89±0.87
EOS $\epsilon$ [%]	12±2	/	11±2

Table 4.11: Tensile test results for Batch 2 (as-built)

	XY Specimens	45° Specimens	Z Specimens
$UTS$ [MPa]	378.5±3.4	384.6±9.4	376.9±13.8
EOS $UTS$ [MPa]	460±20	/	460±20
$YS$ [MPa]	265.5±4.7	260.2±4.6	258.8±6.3
EOS $YS$ [MPa]	270±10	/	240±10
$E$ [GPa]	79.2±6	83.9±5.4	76.7±3.0
EOS $E$ [GPa]	75±10	/	70±10
$\epsilon$ [%]	6.21±0.41	4.43±1.13	3.53±0.71
EOS $\epsilon$ [%]	9±2	/	6±2

The results highlight a consistently different tensile behavior between the two builds. The first batch shows a ductile behavior, while the second one presents a less ductile response. It is thus possible to appreciate the effect of the stress-relieving heat-treatment, which is beneficial in reducing internal defects in the structure and effectively lowering the residual stresses yielding a very ductile material. On the contrary the as-built struc-

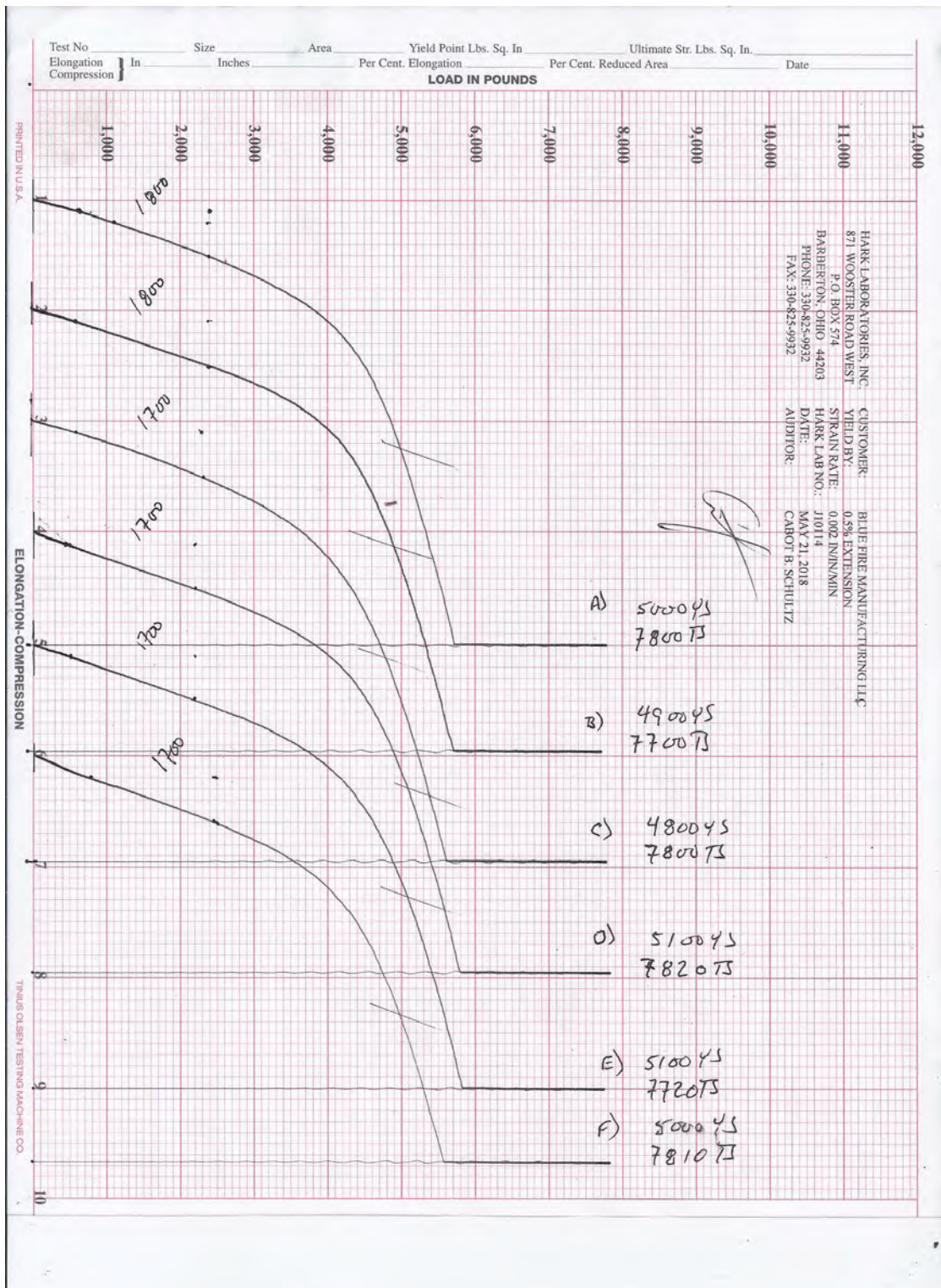


Figure 4.9: Tensile curves as produced by the Tinius Olsen Machine for the Z-axis specimens of Batch 1

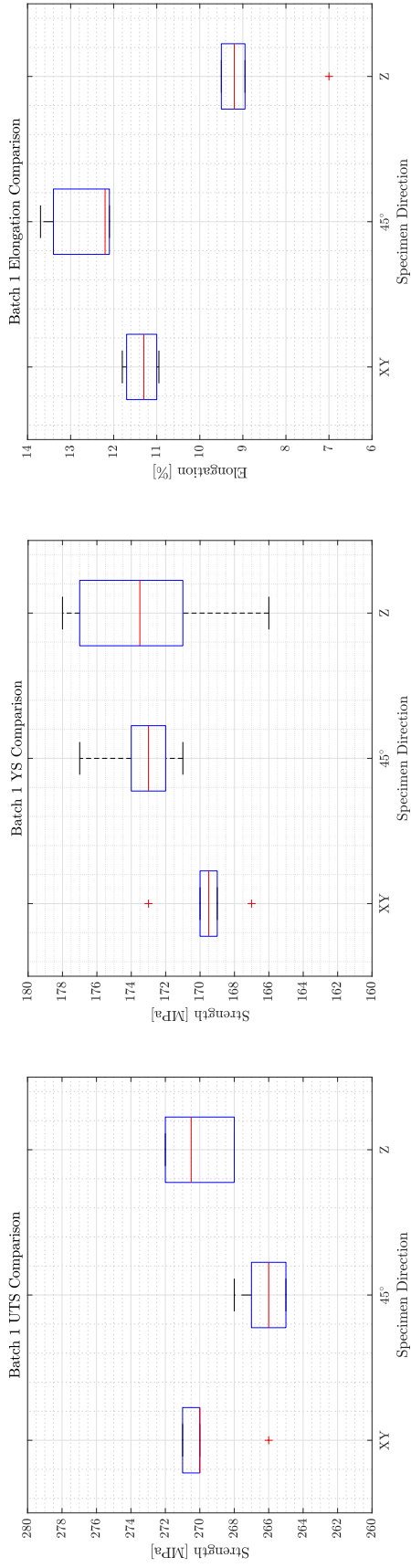
ture, due to the very fine-grained structure resulting from the SLM process shows very high levels of strength. The effects of the stress-relieving heat treatment are evident by comparing the two builds as in Table 4.12. The stress-relieving treatment, at the price of an average 30% loss in strength, yields a minimum increase of 82% in elongation, with the most evident effect for the specimens built along the Z-axis, where the residual stresses due to layer-wise manufacturing are greater to begin with.

*Table 4.12: Percent variation in mechanical properties between as-built and stress-relieved AlSi10Mg specimens*

	XY Specimens	45° Specimens	Z Specimens
<i>UTS</i>	-28.8	-30.8	-28.3
<i>YS</i>	-36.0	-33.3	-33.1
<i>E</i>	-6.3	-10.1	-1.8
$\epsilon$	+82.6	+184.9	+151.8

*Table 4.13: Common mechanical properties for sand-cast and permanent mold-cast AlSi10Mg ([75][76])*

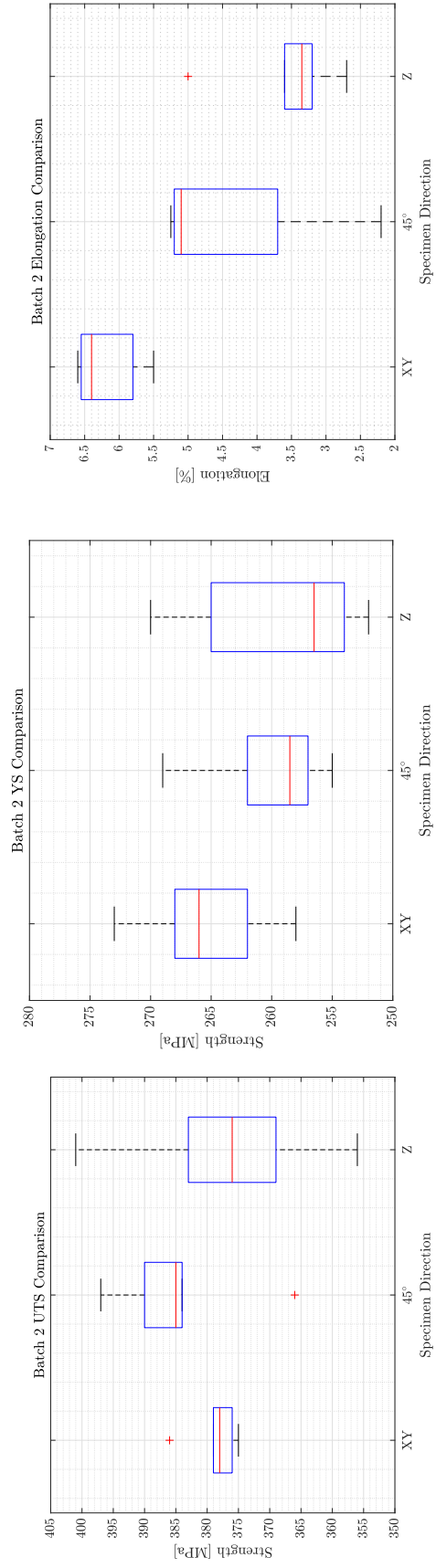
Condition	<i>UTS</i> [MPa]	<i>YS</i> [MPa]	$\epsilon$ [%]
Sand-cast / As-cast	140	80	2
Sand-cast / T6 aged	220	180	1
Permanent mold / As-cast	170	90	2.5
Permanent mold / T6 aged	260	220	1
Permanent mold / T61 aged	330	255	6



(a) Batch 1 UTS

(b) Batch 1 YS

(c) Batch 1 elongation



(d) Batch 2 UTS

(e) Batch 2 YS

(f) Batch 2 elongation

Figure 4.10: Box-plot analysis of mechanical properties variance for North American batches (1 and 2)

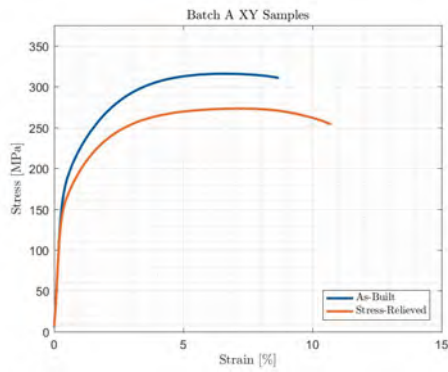
Although neither batches meet EOS target values for, respectively, stress-relieved and as-built specimens they do exceed the mechanical properties expected from conventional cast metal. It is possible to notice that even properties normally attained with complex heat treatments (such as after T61 aging) are met and even surpassed also by the as-built material. It is possible to see how stress-relieved specimens exhibit a behavior exactly comparable with T6 aged cast material, as stated by EOS, while increasing the elongation tenfold. The as-built specimens on the other hand show properties comparable with high-performance T61 aged foundry alloys. At any rate, the worsening of tensile properties, compared to the target values provided by EOS, could be traced back to non-optimized process parameters, yielding a porous structure in all directions (as evidenced by the micrographs), causing a marked decrease of strength due to the actual cross-sectional area of the gauge length being less than the theoretical area. The porosity could also be a common failure initiator by causing crack initiation at lack-of-fusion sites. On the other hand a mostly ductile behavior is conserved due to the stress relieving process.

An important finding is that the process parameters, although not capable of attaining the target values provided by EOS in terms of mechanical properties, yield parts that do not show excessive anisotropy. It is not generally true that Z-axis specimens show higher *UTS* or *YS* than XY specimens, on the contrary as-built specimens show slightly greater strength in the XY direction, while stress-relieved ones show comparable results. The only trace of anisotropy can be found in the elongation behavior of the material: in the as-built material it is possible to notice a decrease in elongation of 43.2% between the XY and Z-axis specimens. This difference is however reduced to only 21.6% after stress-relieving the material, confirming the usefulness of the process to reduce residual stresses and the anisotropy due to layer-wise manufacturing.

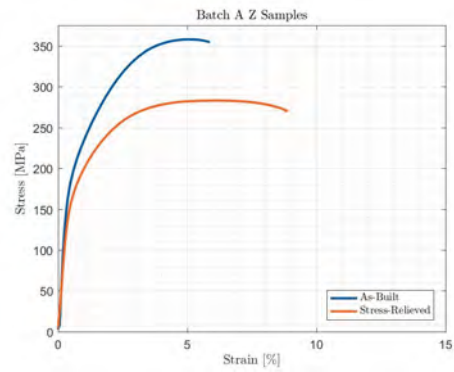
It is moreover interesting to underline that the variability of the results, as shown in Fig 4.10, is minimal. The process parameters are able to deliver parts with high and most importantly consistent performance levels.

#### **4.6.2 Italian Experimental Results**

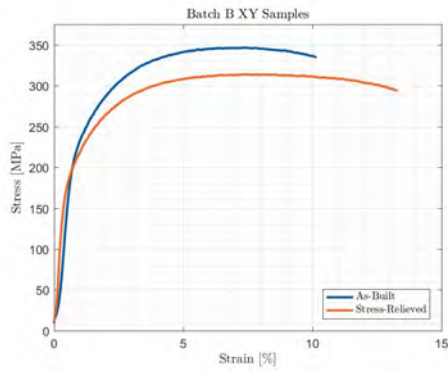
Tensile tests were conducted on specimens grown in both orientations (XY and Z-axis) and in both as-built and stress relieved conditions. Tensile test results are here shown in Fig 4.11 a-d, reporting the stress-strain relationships for as-built and heat treated specimens from batches A, B and C.



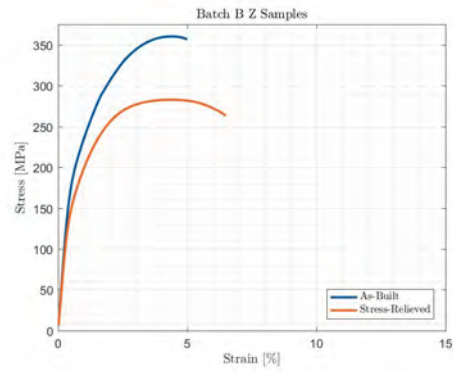
(a) Batch A - Engineering stress-strain curve of XY-plane specimen



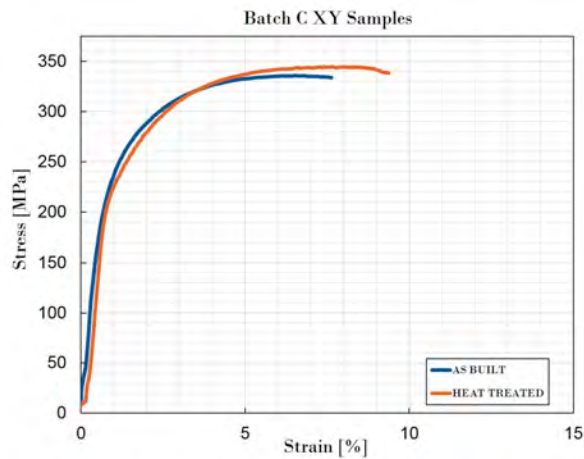
(b) Batch A - Engineering stress-strain curve of Z-axis specimen



(c) Batch B - Engineering stress-strain curve of XY-plane specimen



(d) Batch B - Engineering stress-strain curve of Z-axis specimen



(e) Batch C - Engineering stress-strain curve of XY-plane specimen

Figure 4.11: Engineering stress-strain curves for specimens tested in Italy

Table 4.14: Average tensile test results for specimens tested in Italy

	XY-plane specimens						Z-axis specimens					
	As-built			Stress-relieved			As-built			Stress-relieved		
	Batch A	Batch B	Batch C	Batch A	Batch B	Batch C	Batch A	Batch B	Batch C	Batch A	Batch B	Batch C
UTS [MPa]	315±0.2	346±0.5	335±0.2	274±0.7	313±1	344±4	352±4	361±4	283±1	280±4		
EOS UTS [MPa]	460±20	460±20	460±20	345±10	345±10	345±10	460±20	460±20	350±10	350±10		
YS [MPa]	189±1	225±1	205±3	165.4±2	186±2.5	217±3.5	184±3	187±3	163±6	153±2		
EOS YS [MPa]	270±10	270±10	240±10	230±15	230±15	230±15	240±10	240±10	230±15	230±15		
E [GPa]	62±2	37.73±3	67.8±6	58±2	56.64±3	47.93±6	61±1	70±3	52±8	68±2		
EOS E [GPa]	75±10	75±10	75±10	70±10	70±10	70±10	70±10	70±10	60±10	60±10		
ε [%]	8.45±0.2	10.15±0.5	7.85±0.5	10.5±2	13.25±1	9.1±1	5.65±0.2	4.98±0.4	8.8±2	6.7±0.3		
EOS ε [%]	9±2	9±2	9±2	12±2	12±2	12±2	6±2	6±2	11±2	11±2		

Contrary to what was observed for the specimens built and tested in North America, the specimens tested in Italy do not show an excellent repeatability of results: specimens built along the same direction from Batch A and B show significantly different behaviors. Z-axis specimens from the two batches show different elongation, Batch B being less ductile, while XY-plane specimens from Batch A exhibit a clearly lower level of mechanical strength and elongation with respect to Batch B, although they share the same production parameters with a 30  $\mu\text{m}$  layer thickness; at the same time batches B and C show comparable behavior always in the XY direction, with Batch C slightly less ductile, although they differ in production parameters, Batch C having a 60  $\mu\text{m}$  layer thickness. The differences between Batch A and B in the XY-plane as well as in the Z direction are even larger after the stress relieving process. Anisotropy of the mechanical behavior can moreover be evidenced, especially in Batch A, with specimens grown along the Z-axis showing higher *UTS* than XY-plane specimens, but lower *YS* and elongation. Specimens from Batch B on the other hand show anisotropy only in the elongation behavior, with Z-axis specimens being evidently more fragile.

The post-process stress relieving heat treatment has an evident effect on batches A and B, in both cases determining a decrease in *UTS* and *YS*, and an increase in elongation. The XY specimens from Batch A seem to be outliers, since they show only a limited decrease in strength but show a remarkable increase in ductility. Results from Batch C have to be analyzed considering the different process parameters used for the build. The specimens show excellent mechanical properties: strength levels are comparable with those found in specimens grown in the Z-axis in batches A and B, while the ductile behavior proper of specimens grown in the XY-plane is maintained. The post-process heat treatment however does not significantly affect mechanical strength, but at the same time increases even more the ductility of the material, resulting in an optimal combination of high strength and ductility.

It is important to compare results from Batch C with the results obtained in North America, as the two were built with the same layer thickness. While the results in the as-built condition are comparable, the lack of effects from the heat treatment is reason for further investigation: the process differences lie in the different temperature of the base plate during the build (200  $^{\circ}\text{C}$  vs 165  $^{\circ}\text{C}$  in North American specimens) and in the energy density, lower for Italian specimens. The combination of a higher process temperature with a lower energy density can effectively reduce the level of residual stress throughout the part, leading to a decrease of the effectiveness of the stress-relieving process.

## 4.7 Fracture Surface Characterization

SEM fractography allows for closer investigation of the fracture surfaces and mechanisms, which can highly differ depending on the specimen characteristics.

### 4.7.1 North American Experimental Results

Specimens from both batches were analyzed under the SEM, in order to gain a better understanding of the fracture mechanics of the material both in the as-built and heat-treated condition, comparing specimens in all of the three directions. The general behavior is one of ductile fracture, as typical of aluminum alloys, although the fracture mode varies between the build directions and is affected by the heat treatment. The different build directions can be expected to react differently to the applied stress due to the different layer orientation, as per Fig. 4.12.

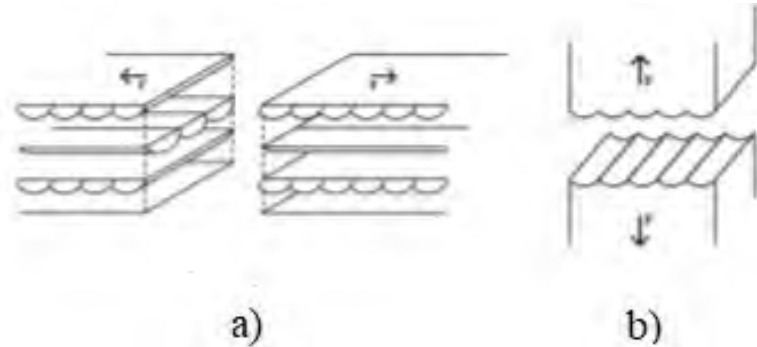
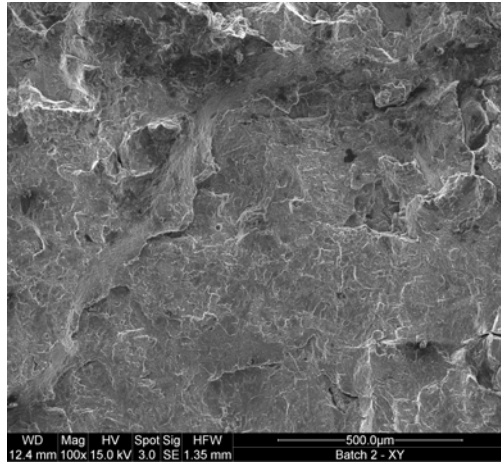


Figure 4.12: Schematics of the interaction between build and stress orientation for (a) XY-plane and (b) Z-axis built specimens

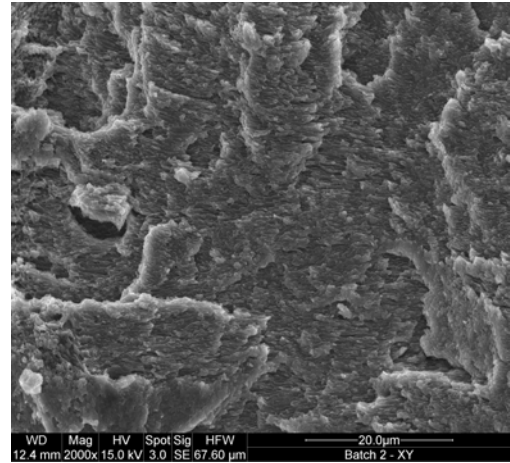
As-built specimens in the XY plane show fracture propagation through the layers, with a progression mechanism in which the single laser tracks fracture once the fracture load is reached, leaving a gap in the structure referred to as *tunnels*, and give a preferential pathway for crack growth. This can be observed Fig 4.13 a, which shows the small gaps left behind by the pre-existing laser tracks. When observing the structure at higher magnification (Fig 4.13 b) it is possible to recognize a ductile intergranular fracture, which also highlights the layered nature of the material, all the grains being oriented parallel to each other. It is however also possible to notice the presence of lack-of-fusion sites throughout the structure, which conceal unmelted powder particles and cause localized brittle fracture as seen in Fig 4.13 c-d.

As-built specimens in the Z direction on the other hand are prone to undergo failure due to inter-layer fracture, possibly enhanced by material defects such as internal porosity and lack-of-fusion sites. The fracture surface appears very rough, with evident cavities caused by local structural defects as shown in Fig 4.14 c-d, where it is possible to observe loose powder particles that were not melted during the build process, leaving behind a defect that causes an evidently brittle fracture. However where the structure does not present defects (Fig 4.14 a and b) it is possible to observe the evidence of a ductile inter-granular fracture. The high cooling rates of SLM process indeed cause silicon segregation at the grain boundaries, creating a weaker point in the structure which constitutes a preferential fracture path, as confirmed by the lower elongation with respect to XY-built specimens.

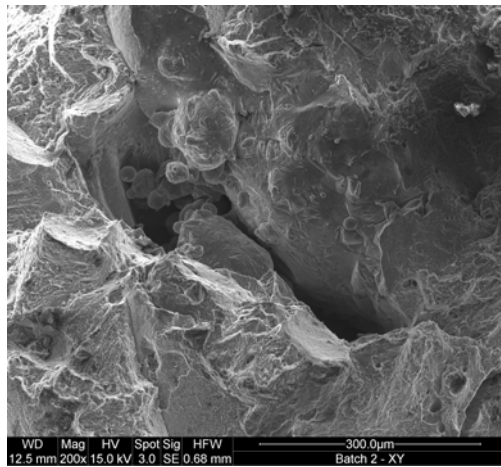
The as-built specimens grown in the 45° direction show a particular behavior, as



(a) Ductile fracture - 100x magnification



(b) Ductile fracture - 2000x magnification

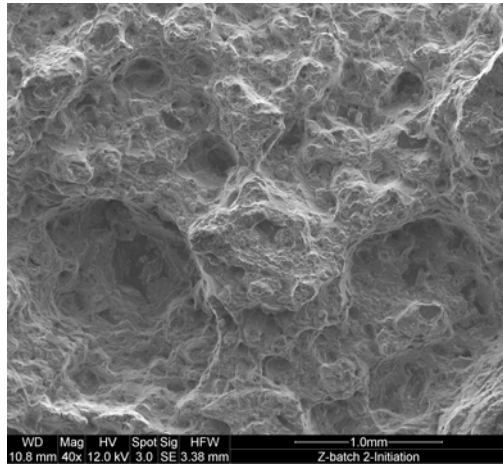


(c) Lack of fusion - 200x magnification

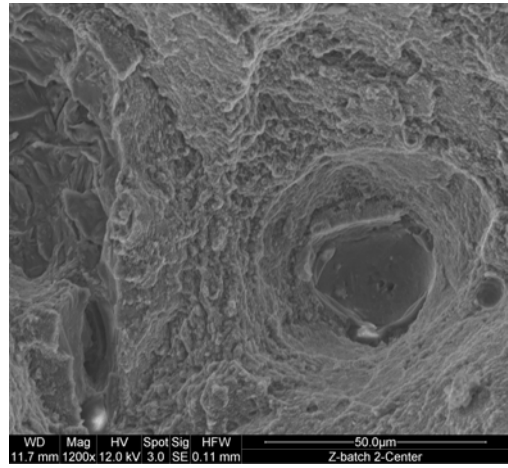


(d) Porosity-induced local brittle fracture - 500x magnification

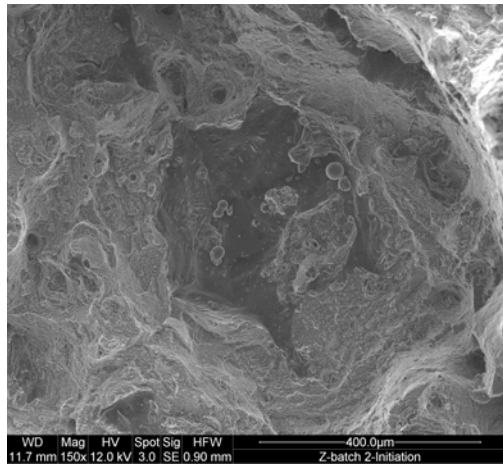
Figure 4.13: SEM image of the fracture surface of XY-plane as-built specimens



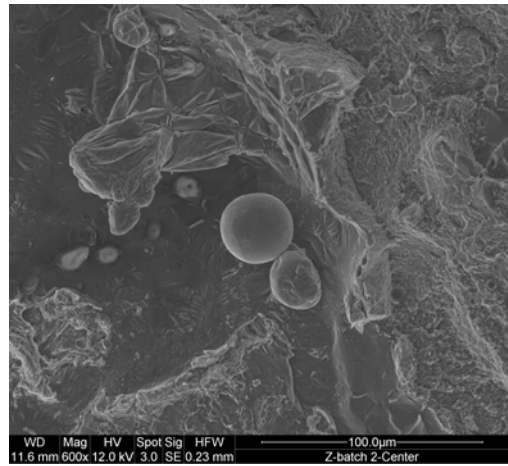
(a) Fracture surface roughness - 40x magnification



(b) Ductile fracture - 1200x magnification

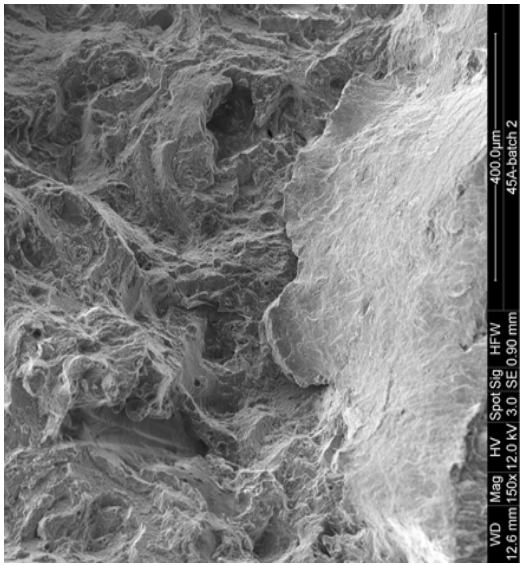


(c) Lack of fusion site with unmelted powder particles - 150x magnification

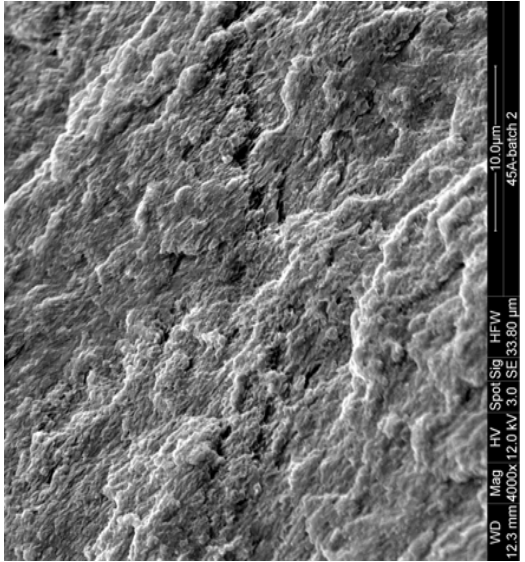


(d) Porosity-induced local brittle fracture - 600x magnification

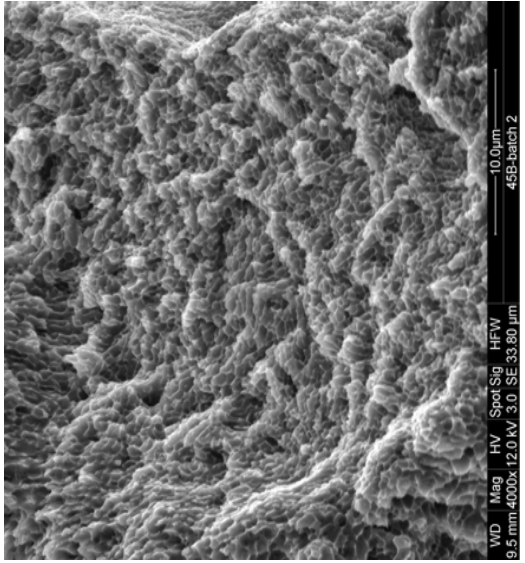
Figure 4.14: SEM image of the fracture surface of Z-axis as-built specimens



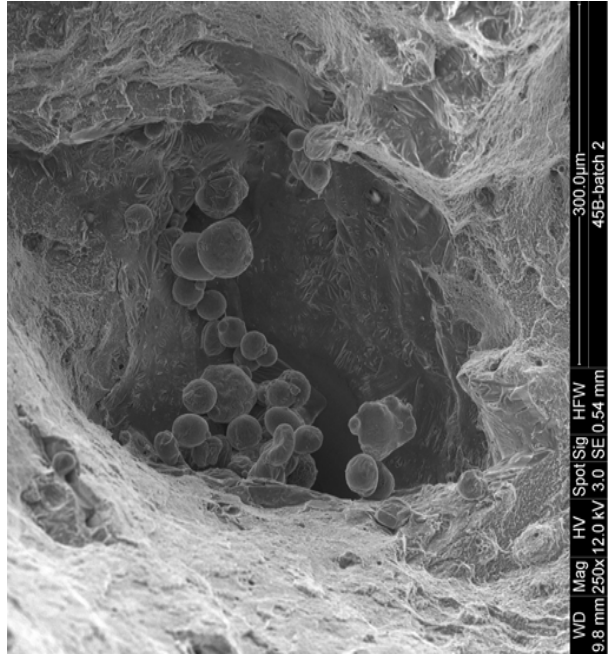
(a) Fracture surface presenting characteristics of both Z and XY-built specimens - 150x magnification



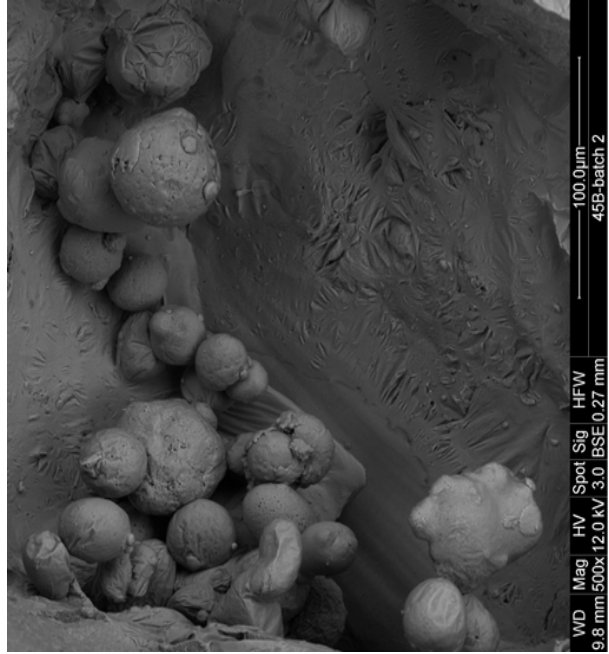
(b) Fracture surface typical of XY specimens - 4000x magnification



(c) Fracture surface typical of Z specimens - 4000x magnification



(d) Porosity cavity with agglomerate of unmelted powder - 250x magnification



(e) Unmelted powder particles - 500x magnification

Figure 4.15: SEM image of the fracture surface of 45°-axis as-built specimens

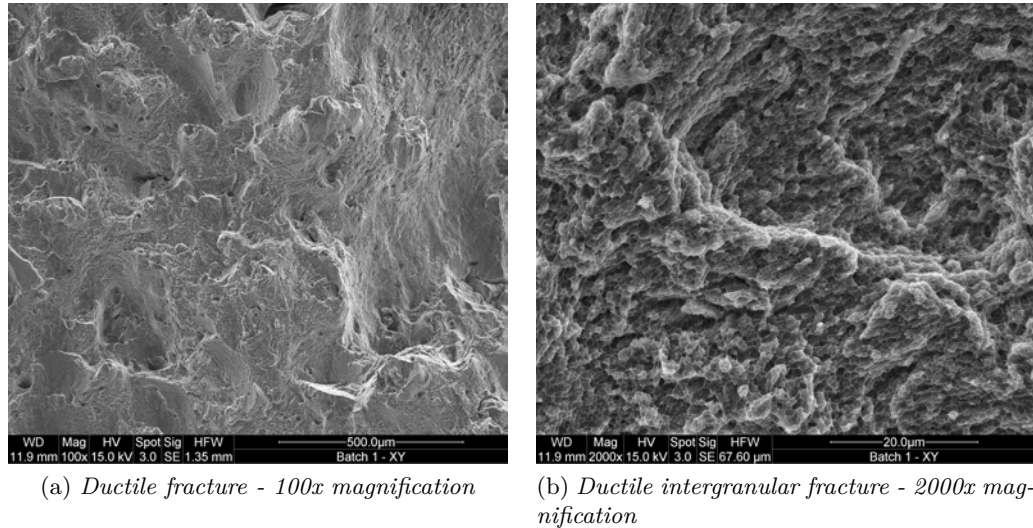


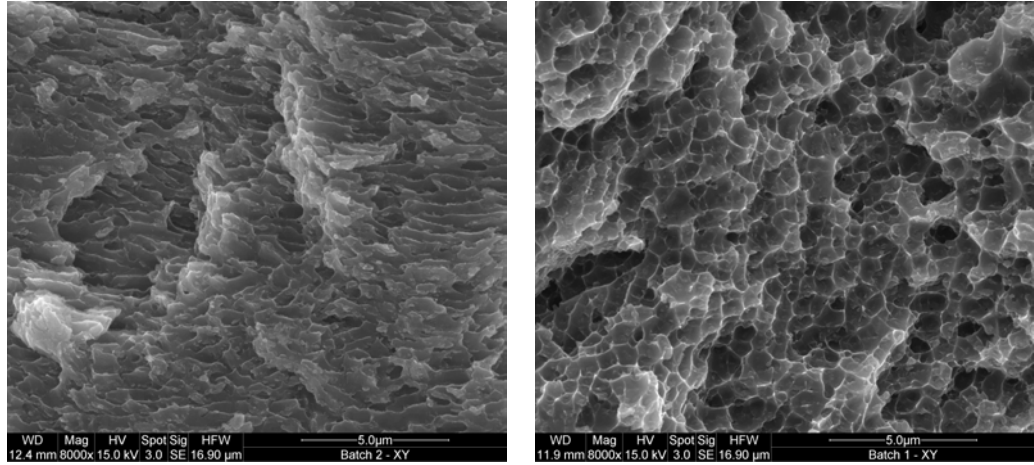
Figure 4.16: SEM image of the fracture surface of XY-plane stress-relieved specimens

it is possible to observe the fracture mechanisms observed on both Z and XY-built specimens, depending on the particular layer (and laser track) orientation. In Fig. 4.15 a, it is possible to observe both the smooth fracture surface typical of XY specimens and the rough intergranular fracture of Z-built specimens. The two fracture mechanisms are evenly distributed across the specimen surface, indeed the specimens have an elongation which is roughly between that of XY and Z specimens, confirming that the two fracture mechanisms interact with each other. It is however also possible to notice, as per the other two directions, the presence of widespread lack-of-fusion sites (Fig 4.15 e-f), with consequent porosity and embrittlement of the microstructure.

The heat treatment process has visible effects on the microstructure, yielding a noticeable reduction in lack-of-fusion sites and a homogenization of the grain structure. Observing stress-relieved specimens in the XY plane (Fig. 4.16) it is possible to notice that the general appearance of the fracture surface is still the same, with a fairly smooth fracture surface in which it is possible to observe intergranular fracture at higher magnifications. It is important to notice that the heat treatment homogenizes the structure, reducing the anisotropy in grain orientation that was initially due to the directional cooling during layer-wise manufacturing, as visible in Fig. 4.17.

Specimens built in the Z-axis show a greatly different fracture surface, which exhibits intergranular fracture even more clearly due to the segregation of silicon particles at the grain boundaries. The silicon segregated at the grain boundaries creates a harder interface which causes the characteristic dimpled surface after intergranular fracture. It is also possible to observe that fracture progresses along the borders of pre-existing laser tracks, which become the preferential path for crack propagation. It is however possible to notice that, differently from the XY-built specimens, the initial porosity could not be entirely eliminated and it is still possible to highlight local brittle fracture areas.

Specimens built in the 45° direction after stress-relieving show a ductile fracture surface, without evident defects and with the fracture propagating both through and

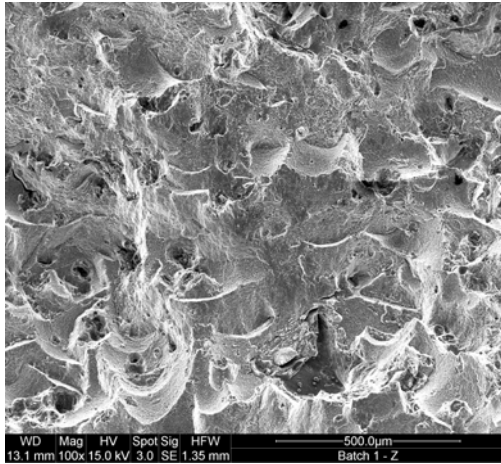


(a) *As-built specimens showing directional grain growth - 8000x magnification*

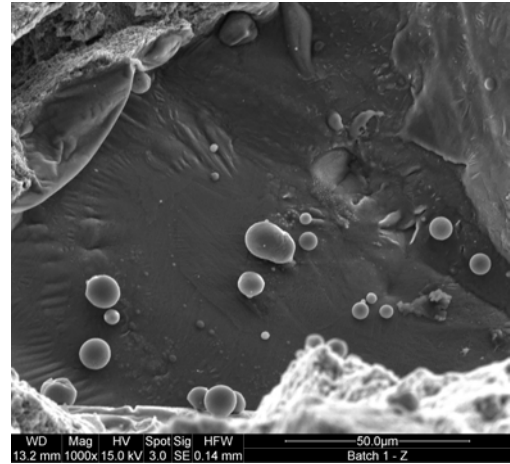
(b) *Stress-relieved specimens - 8000x magnification*

*Figure 4.17: Comparison of as-built and heat treated grain structures for XY specimens*

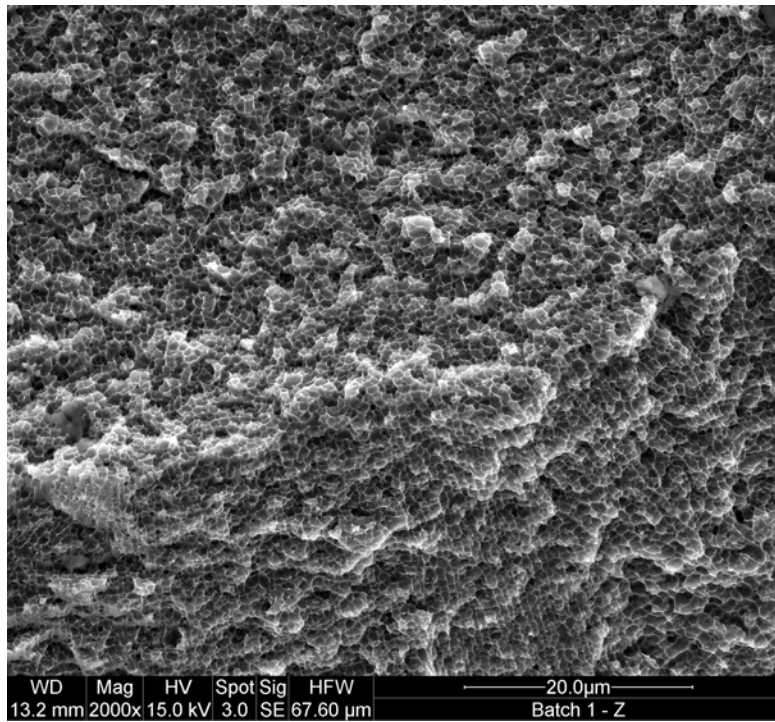
between layers, as seen in Fig 4.19. Differently from the as-built structure though, in the stress-relieved specimens the intergranular fracture is more evident due to the increased silicon segregation at the grain boundaries. It was also possible to observe evidence of silicon particles precipitated in the structure, evidenced by the higher brightness in the back-scatter electron SEM image (Fig 4.19 c)



(a) Fracture surface showing evidence of pre-existing laser tracks - 100x magnification

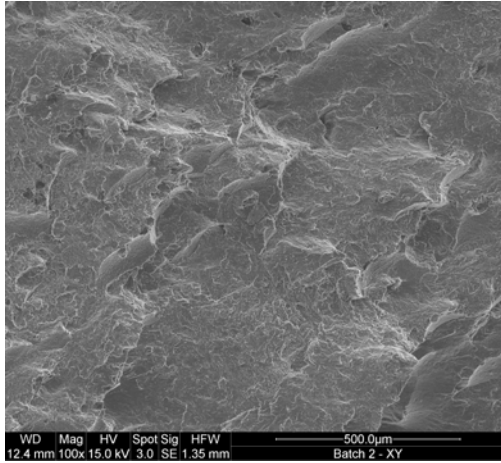


(b) Brittle local fracture induced by unmelted powder particles - 1000x magnification

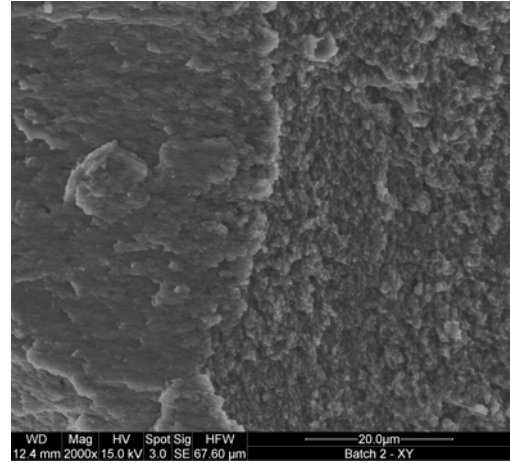


(c) General ductile intergranular fracture - 2000x magnification

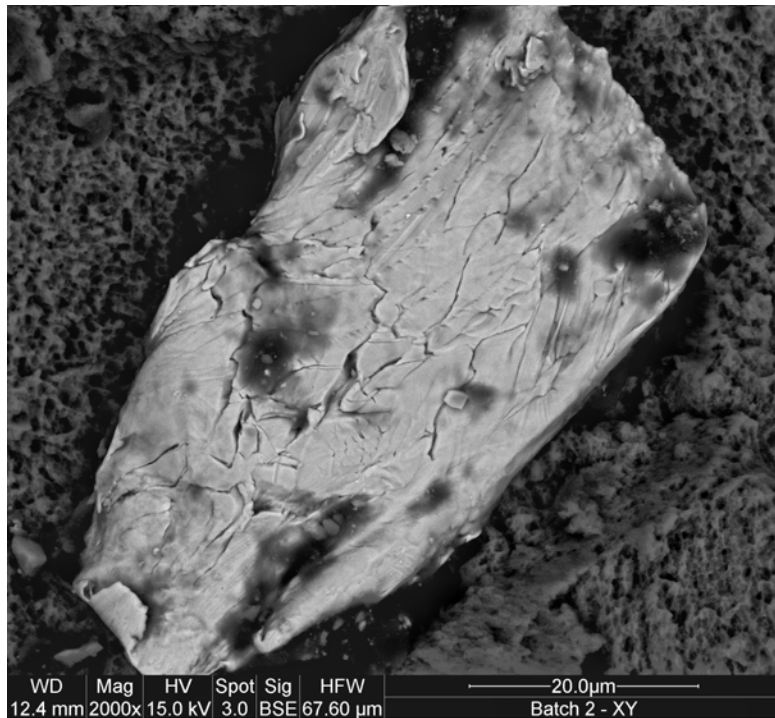
Figure 4.18: SEM images of the fracture surface of Z-axis stress-relieved specimens



(a) Ductile fracture surface - 100x magnification



(b) Inter and intra-layer fracture propagation, with intergranular fracture - 2000x magnification



(c) Silicon precipitate - 2000x magnification

Figure 4.19: SEM images of the fracture surface of 45°-axis stress-relieved specimens

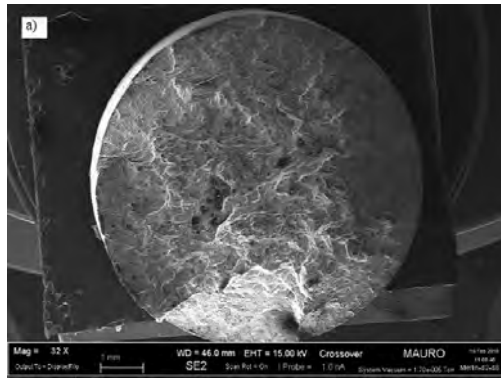
### 4.7.2 Italian Experimental Results

SEM fractography was carried out on both as-built and stress-relieved specimens, observing specimens built in the Z direction as well as in the XY plane, to gain a more complete understanding of the material fracture behavior. The SEM images show a general behavior of ductile fracture to be predominant in all the specimens, although fracture develops with different mechanisms depending on the specimen build direction. Specimens built along the XY-plane show fracture propagation through the layers, with a progression mechanisms in which the single laser tracks fracture, once the fracture load is reached, and give a preferential pathway for crack growth. This can be observed in the SEM image in Fig 4.21b, which shows that the fracture surface is characterized by small holes of different depths, referred to as *tunnels*. These tunnels are the evidence of where the laser beam went during the build: their fracture leaves a gap in the structure as the crack propagates along other track segments with preferential orientation.

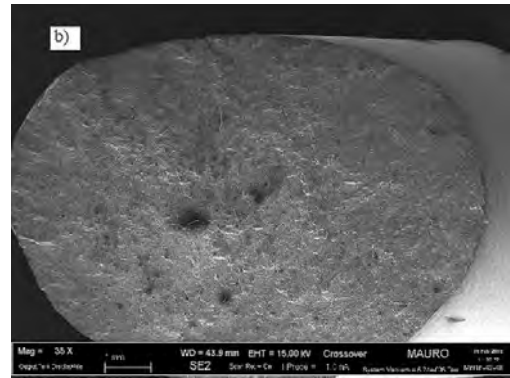
Specimens built in the Z direction on the other hand show failure propagation between the layers, with fracture proceeding through weak parts of the structure where complete adhesion of the layers could not be achieved, and roughness can be noticed on the fracture surface, following the contours of the detached layers as in Fig 4.21a, signaling a ductile fracture mode. It is possible to recognize this as an *inter-domain* fracture, occurring in the separation zone between the various meltpools. The borders of the meltpools have been found [77] to have much coarser grains than the centers, and moreover it was observed in section 4.3 that segregation of silicon particles happens at the grain boundaries and is especially evident at meltpool borders, due to the high cooling rates proper of SLM. It is possible to confirm this phenomenon by observing Fig 4.22a: the bright lines at the grain border are segregated silicon particles. The combination of these two aspects causes the fracture to remain ductile in nature and to propagate along the meltpools and grain boundaries. The cavities observed in Fig 4.21a and Fig 4.22a are therefore not porosities or tunnels but dimples caused by inter-granular fracture.

SEM images of heat-treated specimens show the influence that stress-relieving has on the microstructure and on the fracture mechanism. The heat treatment causes an even more evident silicon segregation at the grain borders and especially at the melt pool boundaries. In case of specimens grown along the Z-axis, as it is possible to observe this in Fig 4.24a, this translates into an even more evident ductile inter-domain fracture, with dimples typical of ductile fracture visible on the whole surface. It is also possible to notice limited grain growth when compared with as-built specimens (see Fig 4.25), as the silicon segregation at the grain boundaries prevents excessive grain growth.

Specimens grown in the XY-plane on the other hand do not show significant microstructural changes between the as-built and stress-relieved conditions. The parts always show gaps corresponding to pre-existent laser tracks and the fracture occurs along preferentially-oriented tracks.

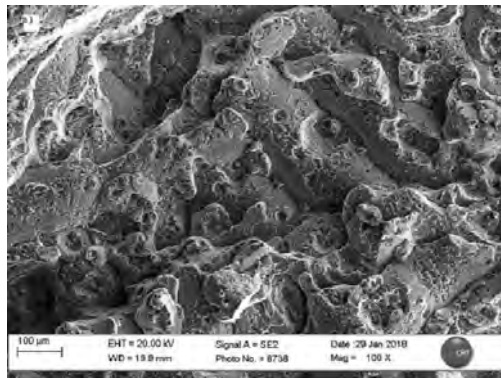


(a) Z-axis specimen



(b) XY-plane specimen

Figure 4.20: Low-magnification image of the fracture surface of as-built specimens

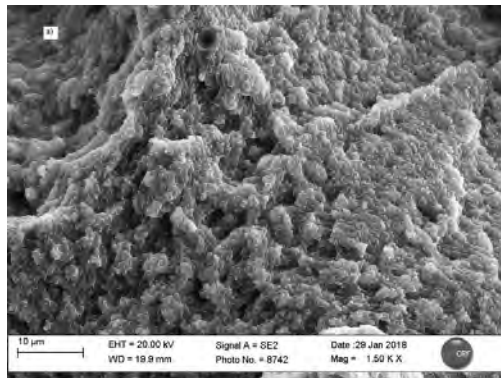


(a) Z-axis specimen

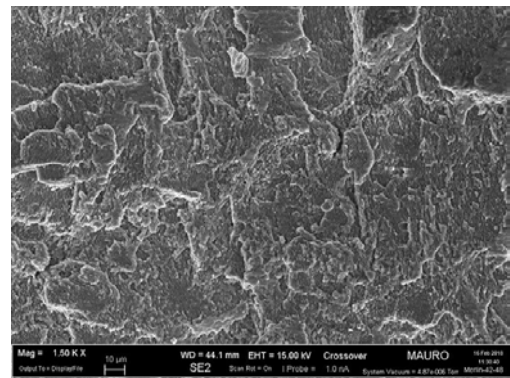


(b) XY-plane specimen

Figure 4.21: 100x image of the fracture surface of as-built specimens

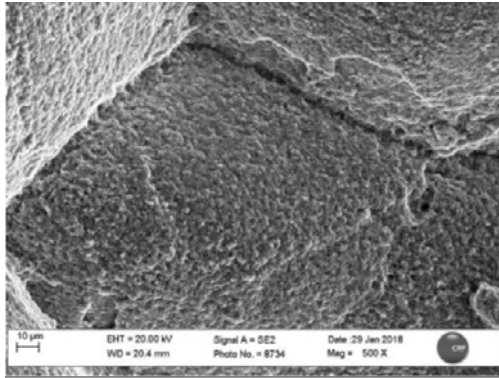


(a) Z-axis specimen



(b) XY-plane specimen

Figure 4.22: 1500x image of the fracture surface of as-built specimens

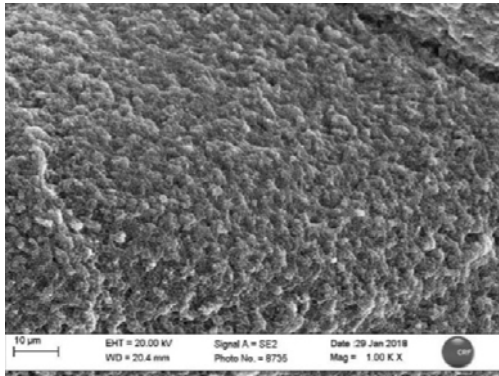


(a) Z-axis specimen (500x)

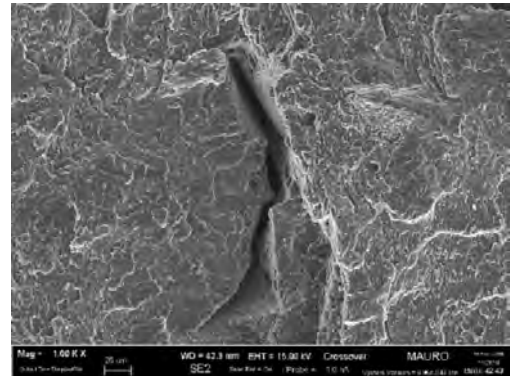


(b) XY-plane specimen (100x)

Figure 4.23: Image of the fracture surface of stress-relieved specimens

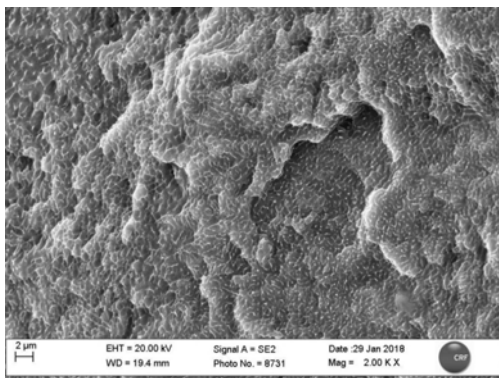


(a) Z-axis specimen

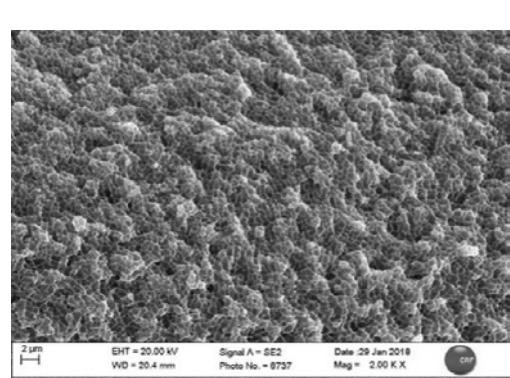


(b) XY-plane specimen

Figure 4.24: 1000x image of the fracture surface of stress-relieved specimens



(a) As-built specimen



(b) Stress-relieved specimen

Figure 4.25: 2000x image - Comparison of the fracture surface of as-built and stress-relieved Z-axis specimens

## Chapter 5

# Discussion of Results

This study was focused on determining the mechanical properties of AlSi10Mg processed via *Selective Laser Melting* and understanding how process parameters affect the mechanical behavior of parts. This manufacturing process is still novel and therefore many of its aspects are still not fully understood.

The main results achieved with the two experimental campaigns in Italy and North America were a complete mechanical characterization of the material (excluding fatigue behavior), analysis of the influence of different process parameters, and of the influence of a post-process heat treatment on the tensile behavior.

The starting material, i.e. a pulverized AlSi10Mg alloy, was analyzed in both experimental campaigns, to verify that test results were not skewed by a defective powder batch. Both suppliers were able to deliver a good quality starting material, with a correct chemical composition and a proper particle size distribution which guarantees the flowability properties required during the SLM processing.

The chemical analysis carried out in North America on both as-built and stress-relieved parts confirms that the parts are representative of an AlSi10Mg alloy, confirming that no contamination of the material occurred during the build process and that the machine used in the study can handle the production of reactive materials with ease. Moreover the chemical analysis can give a first glimpse of what will be confirmed later on: the heat treatment effectively changes the material microstructure, and that is already visible by the change in chemical composition between the as-built and heat treated material.

*Table 5.1: Comparison of chemical composition between as-built and stress-relieved specimens*

	Si	Mg	Fe	Cu	Mn	Zn	Ti	Al
As-built	10.144	0.376	0.130	0.009	0.003	0.008	0.007	Bal.
Stress-relieved	9.557	0.447	0.187	0.025	0.003	0.010	0.018	Bal.
Variation (%)	-6.1	15.9	30.5	64.0	0.0	20.0	61.1	n/d

As visible in Table 5.1 after the heat treatment the parts are subject to a great loss in Silicon content, due to the fact (confirmed by SEM image) that part of the silicon forms precipitates throughout the structure and thus generates a second phase which reduces the weight percentage of silicon dissolved in the aluminum structure.

The analysis of the material microstructure revealed interesting and important information. In both North American and Italian specimens it was found that the material, in the as-built condition, has a very fine microstructure, with evident laser tracks and an evident segregation of silicon particles at the meltpool boundaries. In fact the cooling rates experienced by the material are highest at the borders of the meltpools, as the molten metal is in contact with the rest of the structure silicon particles do not have time to precipitate on their own to create a second phase or to form precipitates with magnesium, and they create a locally homogeneous Al-Si structure, with silicon atoms concentrated at the grain borders.

After heat treatment however the observed structure change. No modifications can be observed in the Italian specimens, with the stress-relieved specimens showing very similar features to the as-built ones (same laser tracks were observed, as well as the same silicon segregation at grain boundaries as in the as-built specimens). On the other hand, the specimens tested by the North American supplier displayed important changes: the microstructure became highly homogeneous, without evident laser tracks in any direction and with silicon evenly distributed at the grain boundaries, although it retains the fine-grained structure typical of SLM parts. The heat treatment can therefore be useful to reduce the anisotropy induced by the layer-wise manufacturing, without causing excessive grain coarsening which would lead to a corresponding reduction of strength.

It is however necessary to report the important amount of porosity found in both as-built and stress-relieved specimens, in both North American and Italian specimens, although differences can be noticed between the two experimental campaigns. The specimens observed in Italy display a predominantly spherical porosity, closely resembling powder-induced porosity, although it is chiefly located at the meltpool borders, possibly indicating problems with lack of fusion of powder particles during the melting process. The porosity does not seem to be heavily affected by the thermal treatment, which only reduces the average dimension of the pores, without eliminating them. On the other hand specimens tested in North America show porosity throughout the entire structure, not only spherical-shaped but also with sharp contours, typical of process-induced defects. It is also important to point out the difference between the porosity of specimens taken from the top and the bottom of bars built along the Z-axis built bars: specimens at the bottom show an evidently lower amount of porosity, because the higher temperature to which they are exposed favors atomic mobility, effectively achieving the closure of the biggest pores. The heat treatment seems to have the opposite effect to the one experienced in Italy, as micrographs of stress-relieved specimens show a much higher level of porosity. This porosity is also highly aligned, possibly pointing to some process-induced defects that were not healed by the heat treatment.

On the Italian side it was possible to verify the density of the material for all three production runs. It can be observed that builds with equal production parameters (Build A and B) share the same levels of porosity, highlighting a good process repeatability, while an increase in layer thickness causes an increase in porosity, as the lower volumetric energy density determines an increase of the number of incompletely melted sites. It is however important to highlight that in any case the measured porosity is greater than claimed by EOS, possibly due to non-optimal process parameters causing an incomplete melting of the powder. It was moreover possible to study the porosity before and after stress-relieving. It was found that the heat treatment does not significantly change the porosity percentage in the material.

The analysis of the material hardness yielded some important results, as it was possible to observe, both in Italy and in North America, an increase of hardness after heat-treatment. The treatment at high temperature allows precipitation of silicon particles within the structure and creates the precipitation hardening effect typical of the AlSi10Mg alloy.

It was also possible to observe how different process parameters can yield different hardness values: Italian specimens built with a 60  $\mu\text{m}$  layer thickness showed higher levels of hardness compared to those with a 30  $\mu\text{m}$  thickness: the higher layer thickness causes a lower cooling rate of the melt pool, as the thermal inertia of the molten material is higher, and thus allows for the formation of a small number of precipitates throughout the structure which are instrumental in increasing the hardness. On the other hand specimens manufactured in North America with a lower base plate heating temperature (165  $^{\circ}\text{C}$  vs. 200  $^{\circ}\text{C}$ ) showed consistently lower hardness values: the lower average temperature in the build chamber results in faster cooling rates, which do not allow significant precipitation, effectively reducing the hardness of the material. It is indeed possible to observe that North American specimens showed a greater response to the heat treatment process with a hardness increase of around 13%, compared to the 1–6% increases found in Italian specimens.

The tensile test results provide the most important data regarding the mechanical characteristics of the material and the influence of the heat treatment. All the specimens show excellent tensile performance already in the as-built state, due to the fine-grained structure evidenced by the microstructural analysis, even surpassing the specifications required for cast materials. It was however possible to detect in all the as-built specimens a certain degree of anisotropy, particularly evident in the elongation of the material as, the fracture mechanism changes depending on the orientation of the specimen: specimens grown along the Z-axis show an evident inter-layer fracture, enhanced by the internal defects of the material, while specimens grown in the XY-plane display higher elongation thanks to the intra-layer fracture, propagating through pre-existent laser tracks, which have increased ductility.

A closer analysis of the results, starting from the North American specimens, reveals that, while exceeding requirements for cast materials, they do not meet the EOS targets for SLM parts. Observing SEM fractographs of as-built specimens it is possible to

notice evident porosity, caused by unmelted powder particles, throughout the structure. The accumulation of defects inside the material limits the mechanical performances and contributes to the embrittlement of the structure. Specimens built along the Z-axis mostly suffer from the effects of internal porosity, showing an elongation which is nearly half of that predicted by EOS and a higher standard deviation for strength measurements, as the failure is initiated by internal defects which are highly inconsistent from part to part. On the other hand specimens built along the XY and 45° direction show a more limited variability of results, as printing defects such as lack-of-fusion sites are parallel to the load and lead to less decrease in cross-sectional area.

The stress-relieving heat treatment has evident effects, causing an improvement of the ductility of the material, together with a reduction of strength. It is however to be noticed that the percentage improvement in ductility surpasses the decrease in strength, and the resulting specimens also show an evident reduction of anisotropy, with Z-axis specimens being subject to the greatest increase in elongation. This can be traced back to the stress-relieving effect (which is most effective in Z-axis specimens which are most affected by the layer-wise manufacturing), to the microstructural homogenization effect of the heat treatment, and to the evident reduction in lack-of-fusion sites throughout the structure. SEM images after stress-relieving reveal fracture surfaces which are mostly ductile, with limited local brittle fracture due to porosity. It was moreover possible to observe a reduction of the effects of directional heat conduction, with a loss of directional grain growth, as in Fig 4.17, confirming the reduction in anisotropy. After stress relieving it is also possible to observe silicon precipitation throughout the structure, confirming the reason behind the hardness increase observed on the stress-relieved specimens.

The tests carried out in Italy highlight a possible problem with SLM manufacturing, that is, batch to batch variability: batch A and B present evidently different results for specimens built along both the XY plane and the Z axis, although the same machine settings were used for manufacturing, with the difference growing larger after stress-relieving. There is no clear evidence for a definite explanation for this behavior, therefore it is possible to hypothesize that process-induced defects such as unmelted powder particles and inter-layer cracking could be the cause of the variability of the results. Since these defects are difficult to predict and control throughout the structure, they do not affect all the builds in the same way.

It is however possible to observe also in the Italian specimens an anisotropy similar to that found in North American specimens, with Z-axis specimens showing higher strength and much lower elongation. The process differences within batches A/B and C raise the need for a separate analysis. Specimens from Batch A and B in the as-built state display slightly lower strength values but much higher elongations than North American-built specimens, while in the stress-relieved state they have comparable, if not higher, elongation and strength values (particularly XY-built specimens from Batch B). Also specimens from batch C show slightly higher elongation and lower strength in the as-built state, while showing much greater strength and lower elongation in the stress-relieved state compared to the North American one.

It is thus possible to infer that generally the higher base plate heating temperature adopted in Italy (effect visible when comparing Batch C with the North American specimens) causes an increased ductility in the as-built state due to the lower residual stresses in the structure, while it also causes a lower response to the stress-relieving heat treatment. On the other hand the lower layer thickness generates again higher residual stresses due to the intense thermal cycling undergone by the structure and causes a more evident response to the heat treatment, while the strength in the as-built state is mostly retained thanks to the more finely-grained microstructure.

## Chapter 6

# Conclusions

This research was aimed at obtaining a characterization of the static mechanical properties of the AlSi10Mg alloy manufactured via *Selective Laser Melting*, analyzing at the same time the influence of heat treatment on the alloy. After two experimental campaigns carried out in North America and in Italy it is possible to draw a series of important conclusions regarding the behavior of the alloy and the future steps required prior to its introduction in the automotive field.

The initial analysis on the microstructure confirmed that the material, when processed with SLM, possesses the peculiar microstructure observed in the literature review, with extremely fine grains, visible laser tracks and non-negligible porosity. The silicon segregation at the melt pool and at the grain boundaries emphasizes the effect of the high cooling rates experienced during the build. These microstructural features highlight the anisotropy of the structure and the influence of defects on the tensile properties. The heat treatment, however, causes a general homogenization of the structure which will be beneficial for the ductility of the material.

The initial non-destructive hardness testing of the specimens provided a first understanding of the anisotropy of the as-built material depending on part orientation and position within the build structure: due to the different thermal histories, parts located at different spots of the build chamber will display different properties. The longer the material remains at the high temperatures generated in the build chamber during the melting process, the more grain coarsening occurs, therefore specimens from volumes of material first melted in the process show a performance decrease of around 6.5 % compared to the last-melting layer. Hardness testing also allowed a comparison between the mechanical properties of as-built and stress-relieved specimens: while it was found that all specimens show lower hardness with respect to the ones advertised by EOS, it was also possible to underline a clear effect of the heat treatment. The stress relieving is instrumental in increasing the hardness of the material via precipitation of silicon particles in the aluminum structure, which are responsible for the precipitation hardening of the AlSi10Mg alloy.

After the density and porosity measurements it was shown that all specimens show higher levels of porosity compared to the EOS target values due to improper fusion of the powder, a result of clearly non-optimal printing parameters. It was also possible

to observe a slight increase in porosity after heat treatment, suggesting that the higher temperatures may cause the entrapped gases to expand and increase the void content of the material. This observation was consistent for all the batches even at different layer thicknesses.

Tensile testing and surface fracture analysis gave the most valuable data regarding the understanding of the material behavior and of the influence of the heat treatment. Mechanical characteristics of the material are clearly not isotropic and not constant, being dependent on the build direction, on the layer thickness and on the applied heat treatment. Specimens grown on the XY plane generally show higher degrees of ductility but lower strength than those built in the Z-axis, with specimens built along the 45° direction showing a mixed behavior since the two different fracture mechanisms coexist. Specimens grown in the XY plane are indeed subject to a fracture that proceeds through different material layers, with the laser tracks acting like fibers that increase the ductility of the material; while Z-axis specimens experience a mostly inter-layer fracture that more easily propagates through internal defects at lack-of-fusion sites, as seen in the SEM fractography. On the microscopic level all specimens undergo a ductile intergranular fracture, with the fracture surface evidencing small grains surrounded by segregated silicon particles, the difference being that Z-axis specimens are more subject to embrittlement due to internal defects.

The stress-relieving heat treatment causes further silicon segregation at the grain boundaries, homogenization of the structure and an important increase in ductility accompanied by a generally less marked decrease in tensile strength. The heat treatment can be said to be instrumental in reducing the anisotropy caused by the layer-wise manufacturing and its influence has been verified for different layer thicknesses and different build plate temperatures, observing a common behavior of highest impact on the *UTS* and on the elongation of the material, with the effects mostly visible for Z-axis specimens.

It can thus be concluded that SLM is a process that has the potential of yielding parts which satisfy the traditional requirements of cast parts (as those reported in Table 4.13). However it was seen that a variety of defects impact the mechanical properties of the material, leaving room for significant improvements. The primary target must be the reduction in anisotropy, in order to produce parts whose mechanical properties can be confidently estimated and used in simulation before the actual build of the component. To this end the use of post-build heat treatment processes is to be considered unavoidable: it has been seen that stress-relieving achieves good improvements in ductility of the material, but the next step would be the application of heat treatments such as Hot Isostatic Pressing, which not only would achieve a reduction of the anisotropy, but would also remove the internal defects of the material by closing internal pores, yielding a material whose properties can be much more repeatable and independent of eventual process variations. A further next step would be to study the behavior of the material under cyclic loading: the fatigue behavior of SLM parts has been the subject of limited studies also in the literature, and has however been found to be highly critical, as the

internal defects induced by the process cause important issues of stress concentration and premature crack initiation, leading to sub-standard fatigue life and to a limitation in the range of use for SLM parts with the current material properties. The application of heat treatments aimed at increasing the material ductility and reducing the impact of internal defects would open the way to the implementation of SLM parts also in applications where fatigue loading has to be accounted for.

Overall, the main conclusions of the project are:

- As-built parts present a fine-grained microstructure with non-negligible porosity and silicon segregation at grain boundaries, as expected from SLM processing.
- Porosity is mainly process-induced with evident lack-of-fusion areas causing local brittle fracture.
- Anisotropy in as-built condition due to layer-wise manufacturing and different sensitivity to defects: parts built along the Z-axis show more fragile behavior than those grown in the XY plane.
- Fracture surface inspection reveals ductile intergranular fracture for all the specimens, with brittle behavior caused by internal defects.
- Stress relieving is effective in homogenizing the structure and reducing residual stresses, effectively increasing elongation and reducing anisotropy.
- SLM process is able to parts that satisfy the highest performance standards for traditional AlSi10Mg manufacturing, and should be seriously considered for further studies aimed at implementing this technology into niche industrial applications.
- Further studies should focus on validation of the material and the process for cyclic loading applications, where sensitivity to defects is even greater.
- Further advancements can be made by reducing internal defects with more optimized process parameters and/or applying more advanced heat treatments.

# Bibliography

- [1] Hideo Kodama. “Automatic method for fabricating a three-dimensional plastic model with photo-hardening polymer”. In: *Review of scientific instruments* 52.11 (1981), pp. 1770–1773.
- [2] Carl Deckard. “Part Generation by Layer-Wise Selective Laser Sintering”. PhD thesis. University of Texas, 1986.
- [3] Dirk Herzog, Vanessa Seyda, Eric Wycisk, and Claus Emmelmann. “Additive manufacturing of metals”. In: *Acta Materialia* 117 (2016), pp. 371–392.
- [4] Todd M Mower and Michael J Long. “Mechanical behavior of additive manufactured, powder-bed laser-fused materials”. In: *Materials Science and Engineering: A* 651 (2016), pp. 198–213.
- [5] S. Leuders, M. Thone, A. Riemer, T. Niendorf, T. Troster, HA. Richard, and HJ. Maier. “On the mechanical behaviour of titanium alloy TiAl6V4 manufactured by selective laser melting: Fatigue resistance and crack growth performance”. In: *International Journal of Fatigue* 48 (2013), pp. 300–307.
- [6] Victor Chastand, Astrid Tezenas, Yannick Cadoret, Philippe Quaegebeur, Wilson Maia, and Eric Charkaluk. “Fatigue characterization of Titanium Ti-6Al-4V samples produced by Additive Manufacturing”. In: *Procedia Structural Integrity* 2 (2016), pp. 3168–3176.
- [7] S Beretta and S Romano. “A comparison of fatigue strength sensitivity to defects for materials manufactured by AM or traditional processes”. In: *International Journal of Fatigue* 94 (2017), pp. 178–191.
- [8] Amanda Sterling, Nima Shamsaei, Brian Torries, and Scott M Thompson. “Fatigue Behaviour of Additively Manufactured Ti-6Al-4V”. In: *Procedia Engineering* 133 (2015), pp. 576–589.
- [9] Eric Wycisk, Andreas Solbach, Shafaqat Siddique, Dirk Herzog, Frank Walther, and Claus Emmelmann. “Effects of defects in laser additive manufactured Ti-6Al-4V on fatigue properties”. In: *Physics Procedia* 56 (2014), pp. 371–378.
- [10] Shafaqat Siddique, Muhammad Imran, Miriam Rauer, Michael Kaloudis, Eric Wycisk, Claus Emmelmann, and Frank Walther. “Computed tomography for characterization of fatigue performance of selective laser melted parts”. In: *Materials & Design* 83 (2015), pp. 661–669.

- [11] Shafaqat Siddique, Muhammad Imran, and Frank Walther. “Very high cycle fatigue and fatigue crack propagation behavior of selective laser melted AlSi12 alloy”. In: *International Journal of Fatigue* 94 (2017), pp. 246–254.
- [12] HV. Atkinson and S. Davies. “Fundamental aspects of hot isostatic pressing: an overview”. In: *Metallurgical and Materials Transactions A* 31.12 (2000), pp. 2981–3000.
- [13] ASTM International. *ASTM F2792-12a, Standard Terminology for Additive Manufacturing Technologies, (Withdrawn 2015)*. West Conshohocken, PA, 2012.
- [14] Mary Kathryn Thompson, Giovanni Moroni, Tom Vaneker, Georges Fadel, R Ian Campbell, Ian Gibson, Alain Bernard, Joachim Schulz, Patricia Graf, Bhrihu Ahuja, et al. “Design for Additive Manufacturing: Trends, opportunities, considerations, and constraints”. In: *CIRP annals* 65.2 (2016), pp. 737–760.
- [15] Ian Gibson, David Rosen, and Brent Stucker. Engineering. Boston, MA: Springer US, 2010. ISBN: 978-1-4419-1119-3. URL: <https://doi.org/10.1007/978-1-4419-1120-9>.
- [16] Julien Gardan. “Additive manufacturing technologies: state of the art and trends”. In: *International Journal of Production Research* 54.10 (2016), pp. 3118–3132.
- [17] Ian Gibson, David Rosen, and Brent Stucker. Engineering. New York, NY: Springer, 2015. ISBN: 978-1-4939-2112-6. URL: <https://doi.org/10.1007/978-1-4939-2113-3>.
- [18] Flaviana Calignano, Diego Manfredi, Elisa Paola Ambrosio, Sara Biamino, Mariangela Lombardi, Eleonora Atzeni, Alessandro Salmi, Paolo Minetola, Luca Iuliano, and Paolo Fino. “Overview on additive manufacturing technologies”. In: *Proceedings of the IEEE* 105.4 (2017), pp. 593–612.
- [19] Concept Laser. *X-LINE 2000R Metal Laser Melting System Brochure*. 2017. URL: [https://www.concept-laser.de/fileadmin/Blaue\\_Broschueren/1708\\_X\\_LINE\\_2000R\\_EN\\_update\\_2\\_\\_lowres\\_einzel.pdf](https://www.concept-laser.de/fileadmin/Blaue_Broschueren/1708_X_LINE_2000R_EN_update_2__lowres_einzel.pdf).
- [20] E Herderick. “Additive manufacturing of metals: A review”. In: *Materials Science and Technology* MS (2011), p. 1413.
- [21] William J. Sames, FA. List, Sreekanth Pannala, Ryan R. Dehoff, and Sudarsanam Suresh Babu. “The metallurgy and processing science of metal additive manufacturing”. In: *International Materials Reviews* 61.5 (2016), pp. 315–360.
- [22] William E. Frazier. “Metal additive manufacturing: a review”. In: *Journal of Materials Engineering and Performance* 23.6 (2014), pp. 1917–1928.
- [23] EOS. *EOS M400-4 Brochure*. 2017. URL: [https://cdn0.scrvt.com/eos/bd4b8d14bf1e79f1/6928a708eeae/EOS\\_System\\_Data\\_Sheet\\_EOS\\_M\\_400-4\\_EN\\_V13\\_web.pdf](https://cdn0.scrvt.com/eos/bd4b8d14bf1e79f1/6928a708eeae/EOS_System_Data_Sheet_EOS_M_400-4_EN_V13_web.pdf).
- [24] Concept Laser. *M-LINE Factory Metal Laser Melting System Brochure*. 2017. URL: [https://www.concept-laser.de/fileadmin/Blaue\\_Broschueren/1708\\_M\\_LINE\\_FACTORY\\_EN\\_update\\_3\\_\\_lowres\\_einzel.pdf](https://www.concept-laser.de/fileadmin/Blaue_Broschueren/1708_M_LINE_FACTORY_EN_update_3__lowres_einzel.pdf).

- [25] Ralf Larson. “Method and device for producing three-dimensional bodies”. US Patent US5786562 A. 1993.
- [26] Arcam AB. *Arcam History*. 2017. URL: <http://www.arcam.com/company/about-arcam/history/>.
- [27] Arcam AB. *Arcam EBM Brochure*. 2017. URL: <http://www.arcamebm.com/>.
- [28] Markforged. *Markforged Metal X Brochure*. 2017. URL: <http://www.markforged.com/>.
- [29] Esmat Sheydaeian, Zachary Fishman, Mihaela Vlasea, and Ehsan Toyserkani. “On the effect of throughout layer thickness variation on properties of additively manufactured cellular titanium structures”. In: *Additive Manufacturing* 18 (2017), pp. 40–47.
- [30] Farzad Liravi and Mihaela Vlasea. “Powder bed binder jetting additive manufacturing of silicone structures”. In: *Additive Manufacturing* 21 (2018), pp. 112–124.
- [31] Roland Berger Strategy Consultants GmbH. “Additive manufacturing: a game changer for the manufacturing industry”. In: (2013).
- [32] Adam Hehr and Marcelo J Dapino. “Dynamics of ultrasonic additive manufacturing”. In: *Ultrasonics* 73 (2017), pp. 49–66.
- [33] Ross J. Friel and Russell A. Harris. “Ultrasonic additive manufacturing—a hybrid production process for novel functional products”. In: *Procedia CIRP* 6 (2013), pp. 35–40.
- [34] Anatoliy Popovich and Vadim Sufiiarov. “Metal Powder Additive Manufacturing”. In: *New Trends in 3D Printing*. InTech, 2016.
- [35] WJ. Sames, F. Medina, WH. Peter, SS. Babu, and RR. Dehoff. “Effect of process control and powder quality on Inconel 718 produced using electron beam melting”. In: *8th International Symposium on Superalloy 718 and Derivatives*. John Wiley & Sons, Inc. 2014, pp. 409–423.
- [36] EOS GmbH. *Materials for Additive Manufacturing*. 2017. URL: <https://www.eos.info/material-m>.
- [37] Concept Laser. *AM Materials*. 2017. URL: <https://www.concept-laser.de/en/products/materials.html>.
- [38] SLM Solutions. *SLM Metal Powder*. 2017. URL: <https://slm-solutions.com/products/accessories-and-consumables/slm-metal-powder>.
- [39] Malgorzata Warmuzek. *Aluminum-silicon casting alloys: an atlas of microfractographs*. ASM international, 2004.
- [40] Cassiopée Galy, Emilie Le Guen, Eric Lacoste, and Corinne Arvieu. “Main defects observed in aluminum alloy parts produced by SLM: from causes to consequences”. In: *Additive Manufacturing* (2018).

- [41] Noriko Read, Wei Wang, Khamis Essa, and Moataz M. Attallah. “Selective laser melting of AlSi10Mg alloy: Process optimisation and mechanical properties development”. In: *Materials & Design (1980-2015)* 65 (2015), pp. 417–424.
- [42] Karolien Kempen, Lore Thijs, Evren Yasa, Mohsen Badrossamay, Wesley Verheercke, and Jean-Pierre Kruth. “Microstructural analysis and process optimization for selective laser melting of AlSi10Mg”. In: *Solid Freeform Fabrication Symposium Proceedings*. 2011.
- [43] Francesco Trevisan, Flaviana Calignano, Massimo Lorusso, Jukka Pakkanen, Alberta Aversa, Elisa Paola Ambrosio, Mariangela Lombardi, Paolo Fino, and Diego Manfredi. “On the selective laser melting (SLM) of the AlSi10Mg alloy: process, microstructure, and mechanical properties”. In: *Materials* 10.1 (2017), p. 76.
- [44] John A Slotwinski, Edward J Garboczi, and Keith M Hebenstreit. “Porosity measurements and analysis for metal additive manufacturing process control”. In: *Journal of research of the National Institute of Standards and Technology* 119 (2014), p. 494.
- [45] Usman Ali, Yahya Mahmoodkhani, Shahriar Imani Shahabad, Reza Esmaeilizadeh, Farzad Liravi, Esmat Sheydaeian, Ke Yin Huang, Ehsan Marzbanrad, Mihaela Vlasea, and Ehsan Toyserkani. “On the measurement of relative powder-bed compaction density in powder-bed additive manufacturing processes”. In: *Materials & Design* (2018).
- [46] Nesma T. Aboulkhair, Nicola M. Everitt, Ian Ashcroft, and Chris Tuck. “Reducing porosity in AlSi10Mg parts processed by selective laser melting”. In: *Additive Manufacturing* 1 (2014), pp. 77–86.
- [47] Karolien Kempen, Lore Thijs, Jan Van Humbeeck, and J-P Kruth. “Mechanical properties of AlSi10Mg produced by selective laser melting”. In: *Physics Procedia* 39 (2012), pp. 439–446.
- [48] Jean-Pierre Kruth, Jan Deckers, Evren Yasa, and Ruben Wauthlé. “Assessing and comparing influencing factors of residual stresses in selective laser melting using a novel analysis method”. In: *Proceedings of the institution of mechanical engineers, Part B: Journal of Engineering Manufacture* 226.6 (2012), pp. 980–991.
- [49] DD Gu, Wilhelm Meiners, Konrad Wissenbach, and Reinhart Poprawe. “Laser additive manufacturing of metallic components: materials, processes and mechanisms”. In: *International materials reviews* 57.3 (2012), pp. 133–164.
- [50] Tatiana Mishurova, Sandra Cabeza, Tobias Thiede, Naresh Nadammal, Arne Kromm, Manuela Klaus, Christoph Genzel, Christoph Haberland, and Giovanni Bruno. “The influence of the support structure on residual stress and distortion in SLM Inconel 718 parts”. In: *Metallurgical and Materials Transactions A* 49.7 (2018), pp. 3038–3046.

- [51] Ahmed H. Maamoun, Mohamed Elbestawi, Goulmara K. Dosbaeva, and Stephen C. Veldhuis. “Thermal post-processing of AlSi10Mg parts produced by Selective Laser Melting using recycled powder”. In: *Additive Manufacturing* 21 (2018), pp. 234–247.
- [52] Alessandro Salmi, Eleonora Atzeni, Luca Iuliano, and Manuela Galati. “Experimental analysis of residual stresses on AlSi10Mg parts produced by means of selective laser melting (SLM)”. In: *Procedia CIRP* 62 (2017), pp. 458–463.
- [53] Erhard Brandl, Ulrike Heckenberger, Vitus Holzinger, and Damien Buchbinder. “Additive manufactured AlSi10Mg samples using Selective Laser Melting (SLM): Microstructure, high cycle fatigue, and fracture behavior”. In: *Materials & Design* 34 (2012), pp. 159–169.
- [54] U. Tradowsky, J. White, R.M. Ward, N. Read, W. Reimers, and M.M. Attallah. “Selective laser melting of AlSi10Mg: influence of post-processing on the microstructural and tensile properties development”. In: *Materials & Design* 105 (2016), pp. 212–222.
- [55] Lore Thijs, Karolien Kempen, Jean-Pierre Kruth, and Jan Van Humbeeck. “Fine-structured aluminium products with controllable texture by selective laser melting of pre-alloyed AlSi10Mg powder”. In: *Acta Materialia* 61.5 (2013), pp. 1809–1819.
- [56] Naor Elad Uzan, Shlomo Ramati, Roni Shneck, Nachum Frage, and Ori Yeheskel. “On the effect of shot-peening on fatigue resistance of AlSi10Mg specimens fabricated by additive manufacturing using selective laser melting (AM-SLM)”. In: *Additive Manufacturing* 21 (2018), pp. 458–464.
- [57] Ahmed H. Maamoun, Mohamed A. Elbestawi, and Stephen C. Veldhuis. “Influence of Shot Peening on AlSi10Mg Parts Fabricated by Additive Manufacturing”. In: *Journal of Manufacturing and Materials Processing* 2.3 (2018). ISSN: 2504-4494. DOI: 10.3390/jmmp2030040. URL: <http://www.mdpi.com/2504-4494/2/3/40>.
- [58] Roland Berger Strategy Consultants GmbH. “Additive Manufacturing in Aerospace and Defense”. In: (2017).
- [59] Mark Cotteleer and Jim Joyce. “3D opportunity: Additive manufacturing paths to performance, innovation, and growth”. In: *Deloitte Review* 14 (2014), pp. 5–19.
- [60] ASTM International. *ASTM E466-15 Standard Practice for Conducting Force Controlled Constant Amplitude Axial Fatigue Tests of Metallic Materials*. West Conshohocken, PA, 2015.
- [61] ASTM International. *ASTM E647-15e1 Standard Test Method for Measurement of Fatigue Crack Growth Rates*. West Conshohocken, PA, 2015.
- [62] Eric Wycisk, Shafaqat Siddique, Dirk Herzog, Frank Walther, and Claus Emmelmann. “Fatigue performance of laser additive manufactured Ti-6Al-4V in very high cycle fatigue regime up to 10<sup>9</sup> cycles”. In: *Frontiers in Materials* 2 (2015), p. 72.

- [63] S. Siddique, M. Imran, E. Wycisk, C. Emmelmann, and F. Walther. “Fatigue assessment of laser additive manufactured AlSi12 eutectic alloy in the very high cycle fatigue (VHCF) range up to 1E9 cycles”. In: *Materials Today: Proceedings* 3.9 (2016), pp. 2853–2860.
- [64] ASTM International. *ASTM E8/E8M-16a Standard Test Method for Tension Testing of Metallic Materials*. West Conshohocken, PA, 2016.
- [65] EN ISO. *6892-1 - Metallic materials - Tensile testing - Part 1: Method of test at room temperature*. 2009.
- [66] ASTM International. *E1251-11 - Standard Test Methods for Analysis of Aluminum and Aluminum Alloys by Spark Atomic Emission Spectrometry*. West Conshohocken, PA, 2011.
- [67] ASTM International. *E158-86 - Standard Practice for Fundamental Calculations to Convert Intensities into Concentrations in Optical Emission Spectrochemical Analysis*. West Conshohocken, PA, 1986.
- [68] ASTM International. *E18-17e1 - Standard Test Methods for Rockwell Hardness of Metallic Materials*. West Conshohocken, PA, 2017.
- [69] EN ISO. *6506-1 - Metallic materials - Brinell hardness test - Part 1: Test method*. 2005.
- [70] Perrin Walker and William H. Tarn. *CRC handbook of metal etchants*. CRC press, 1990.
- [71] BJ Inkson. “Scanning electron microscopy (SEM) and transmission electron microscopy (TEM) for materials characterization”. In: *Materials characterization using nondestructive evaluation (NDE) methods*. Elsevier, 2016, pp. 17–43.
- [72] Weilie Zhou, Robert Apkarian, Zhong Lin Wang, and David Joy. “Fundamentals of scanning electron microscopy (SEM)”. In: *Scanning microscopy for nanotechnology*. Springer, 2006, pp. 1–40.
- [73] ASTM International. *E140-12b - Standard Hardness Conversion Tables for Metals Relationship Among Brinell Hardness, Vickers Hardness, Rockwell Hardness, Superficial Hardness, Knoop Hardness, Scleroscope Hardness, and Leeb Hardness*. West Conshohocken, PA, 2013.
- [74] Buehler Wilson Hardness. *Hardness Conversion Chart*. 2018. URL: <http://www.ampht.com/pdfs/WilsonConversionChart.pdf>.
- [75] Joseph R. Davis et al. *Aluminum and aluminum alloys*. ASM international, 1993.
- [76] Stena Aluminum. *Cast Aluminum Alloys Specifications*. 2018. URL: <https://www.stenaaluminium.com/aluminium-alloys-and-services/alloy-specifications>.
- [77] J-P. Kruth, G. Levy, F. Klocke, and THC. Childs. “Consolidation phenomena in laser and powder-bed based layered manufacturing”. In: *CIRP annals* 56.2 (2007), pp. 730–759.

# Vita Auctoris

NAME: Carlo Marinelli

PLACE OF BIRTH: Saluzzo, Piedmont, Italy

YEAR OF BIRTH: 1994

EDUCATION: Liceo Classico Carlo Botta, Ivrea, Italy, 2013

Politecnico di Torino, Torino, Italy, 2016

University of Windsor, Windsor, Canada, 2018